

Die approbierte Originalversion dieser Dissertation ist an der Hauptbibliothek der Technischen Universität Wien aufgestellt (<http://www.ub.tuwien.ac.at>).

The approved original version of this thesis is available at the main library of the Vienna University of Technology (<http://www.ub.tuwien.ac.at/englweb/>).



TECHNISCHE
UNIVERSITÄT
WIEN
VIENNA
UNIVERSITY OF
TECHNOLOGY

Dissertation

Design and Computational Analysis of Compound Castings and other Multi-Material Structures

ausgeführt zum Zwecke der Erlangung des akademischen Grades eines
Doktors der technischen Wissenschaften unter der Leitung von

O.Univ.Prof. Dipl.-Ing. Dr. Franz G. Rammerstorfer
Institut für Leichtbau und Struktur-Biomechanik

eingereicht an der Technischen Universität Wien
Fakultät für Maschinenwesen und Betriebswissenschaften

von

Dipl.-Ing. Robert D. Bitsche
Matrikelnummer: 9825484
Refsnægade 30, 3.th
2200 Copenhagen N
Denmark

Wien, im April 2009

Robert D. Bitsche

Abstract

The multi-material lightweight design concept strives to use the “best” material and manufacturing process for each part of a structure in order to combine the advantages of different materials. Obviously, joining techniques play a major role in the manufacturing of these structures. The *compound casting process* allows for the joining of a casting to other parts during the casting process. That is, the casting process serves both as a production and a joining process.

The aim of this thesis is to develop computational methods for the analysis and design of compound castings and other multi-material structures. Both finite element methods and asymptotic analysis techniques are used.

During the quenching (or cooling) of a compound casting residual stresses develop due to the inhomogeneous transient temperature field and the dissimilar coefficients of thermal expansion of the materials involved. As these stresses determine the frictional connection and other important characteristics (e.g. the fatigue life) of the structure, the simulation of the quenching process is of central importance.

In the case of purely contacting interfaces, i.e., if no metallurgical bonding exists, the heat transfer at the interface is either by contact or through the gap, and the thermal contact conductance at the bimaterial interface of the compound casting depends on contact pressure and gap opening. A major finding of this thesis is that, in general, the consideration of this dependence is crucial to the simulation of the quenching process of compound castings.

During the quenching process gaps can open up at the bimaterial interface even if the structure is geometrically simple. The opening of the gap severely reduces the thermal contact conductance and forces heat to flow mainly parallel to the open gap.

Practical examples of steel-aluminum compound castings with form-locking and/or frictional connection are presented. In general, the strength of these connections could be well predicted by the finite element simulations.

Local stress concentrations can occur due to the abrupt change in material properties at the interface of a multi-material structure. Under the assumptions of linear elasticity theory, these stress concentrations can manifest themselves as stress singularities. The dependence of the order of these singularities on geometrical and material parameters is examined in a systematic way and “design charts” are developed by which the order of the stress singularity can be directly registered. Using these charts, geometry modifications can be determined that either minimize the order of the stress singularity or lead to a regular stress field. Often, great improvements can be achieved through comparatively small and local modifications of the geometry.

Keywords: compound casting, multi-material structures, quenching simulation, thermal contact conductance, finite element analysis, stress singularities.

Kurzfassung

Das Multi-Material Leichtbau-Konzept strebt danach, den “besten” Werkstoff und den besten Herstellungsprozess für jeden Bereich einer Struktur einzusetzen. Damit können die Vorteile unterschiedlicher Werkstoffe miteinander kombiniert werden. Fügetechnik spielt in diesem Zusammenhang eine wichtige Rolle. Der *Verbundguss* ermöglicht es, Gussbauteile während des Gießprozesses mit anderen Bauteilen zu verbinden. Das heißt, der Gießprozess dient gleichzeitig als Herstellungs- und Fügeprozess.

Ziel der vorliegenden Arbeit ist die Entwicklung von Berechnungsmethoden zur Untersuchung und Gestaltung von Verbundguss-Strukturen und anderen Verbundbauteilen. Dabei kommen sowohl Finite Elemente Methoden als auch asymptotische Methoden zum Einsatz.

Während des Abschreckens (oder Abkühlens) eines Verbundgussbauteils entwickelt sich auf Grund des inhomogenen transienten Temperaturfeldes sowie auf Grund der unterschiedlichen Wärmeausdehnungskoeffizienten der beteiligten Werkstoffe ein Eigenspannungszustand. Da diese Eigenspannungen die kraftschlüssige Verbindung und andere wichtige Eigenschaften (z.B. die Betriebsfestigkeit) des Bauteils bestimmen, ist die Simulation des Abschreckvorgangs von zentraler Bedeutung.

Wenn am Interface des Verbundgussbauteils keine stoffschlüssige Verbindung vorliegt, dann ist mit Wärmeübertragung durch Kontakt zu rechnen, und die thermische Kontaktleitfähigkeit am Interface hängt vom Kontaktdruck bzw. von der Spaltbreite ab. Die vorliegende Arbeit zeigt, dass die Berücksichtigung dieser Abhängigkeit bei der Simulation des Abschreckvorgangs von Verbundgussbauteilen äußerst wichtig ist.

Während des Abschreckvorgangs können sich Spalte am Interface des Verbundgussbauteils bilden. Dies ist selbst dann möglich, wenn es sich um ein geometrisch einfaches Bauteil handelt. Durch das Öffnen des Spaltes wird die thermische Kontaktleitfähigkeit deutlich reduziert, und der Wärmestrom ist gezwungen, hauptsächlich parallel zum Interface zu verlaufen.

Es werden praktische Beispiele für Stahl-Aluminium Verbundgussbauteile mit form- und/oder kraftschlüssiger Verbindung vorgestellt. Im allgemeinen konnte die Festigkeit der Verbindung dieser Bauteile von den Finite Elemente Simulationen gut vorhergesagt werden.

Die sprunghafte Änderung der Materialeigenschaften am Interface von Verbundbauteilen kann zum Auftreten lokaler Spannungskonzentrationen führen. Unter den Annahmen der linearen Elastizitätstheorie können sich diese Spannungskonzentrationen in Form von Spannungssingularitäten äußern. Die Abhängigkeit der Ordnung dieser Singularitäten von geometrischen Größen und Materialparametern wird systematisch untersucht, und “Design Diagramme” werden erstellt, von denen die Ordnung der Singularität direkt abgelesen werden kann. Mit Hilfe dieser Diagramme können geometrische Änderungen bestimmt werden, welche entweder die Ordnung der Singularität

vermindern oder zu einem regulären Spannungsfeld führen. Oft können große Verbesserungen durch vergleichsweise kleine und lokale Änderungen der Geometrie erreicht werden.

Schlüsselbegriffe: Verbundguss, Verbundbauteile, Abschrecken, thermische Kontaktleitfähigkeit, Finite Elemente Methode, Spannungssingularitäten.

Acknowledgment

My deepest gratitude is to my advisor, Prof. Dr. Franz G. Rammerstorfer. He is at the same time a great scientist, a great teacher and an honest, generous and kind-hearted person. I am much indebted to him for his valuable feedback and challenges which taught me to think critically and express my ideas. It has been my great pleasure and privilege to have him as my advisor.

I would also like to thank Prof. Dr. Franz Dieter Fischer from Montanuniversität Leoben for acting as my co-advisor.

This thesis was prepared in the course of my employment at the Institute of Lightweight Design and Structural Biomechanics (ILSB) at the Vienna University of Technology. The ILSB is known for its scientific excellence but also for its warm and welcoming environment. I would like to express my appreciation to all people who contribute to making the ILSB such a special place. Being a part of the ILSB has been a great experience that I will cherish forever.

Many people at the ILSB contributed to the following thesis through discussion, commentary and constructive criticism. Particularly, I would like to thank Prof. Dr. Helmut J. Böhm (head of the ILSB), Dr. Thomas Daxner, Dr. Dieter Pahr, Dr. Sergio Nogales, Dr. Bernhard Höfl, Dr. Christopher Huber, Dipl.-Ing. Christian Bilik, Dipl.-Ing. Andreas Reisinger, Dr. Gerald Wimmer, Dipl.-Ing. Thomas Flatscher, Dr. Christian Grohs, Dr. Mathias Luxner and Dr. Clara Schuecker.

Further thanks go to Prof. Hans-Peter Degischer, Dr. Anette Danninger and Dipl.-Ing. Karolina Zimnik from the Institute of Materials Science and Technology for their various contributions.

During my time at the ILSB, I became a fan of the Linux operating system and other free software projects. Therefore, I would like to thank all the people who contribute to these projects. In this context, I would also like to thank Gerhard Schneider, the ILSB's system administrator, for providing a unique working environment and acting as my informal Linux instructor.

I am also indebted to the people at Leichtmetallkompetenzzentrum Ranshofen (LKR) who helped me to put theoretical ideas into practice. Particularly, I would like to acknowledge Dipl.-Ing. Ziad Khalil, Dipl.-Ing. (FH) Christian Peterlechner, Dipl.-Ing. Werner Fragner and Dr. Ulf Noster.

I would like to thank the Austrian Research Centers and the Austrian National Foundation for funding this research work in the framework of the project *Austrian Light Weight Structures*.

I am grateful to Dipl.-Ing. Verena Batlogg who went through the tedious task of proof-reading this thesis and provided valuable feedback.

None of this would have been possible without the love and support of my parents, Ingrid and Ernst. I owe them everything.

Finally, I would like to thank Sarah for being the wonderful person she is.

For my grandmother,

Erna Kessler

Contents

1	Introduction	10
1.1	Joining Fundamentals	11
1.2	Aim and Outline of the Thesis	12
2	Finite Element Analysis of Quenching and other Heat Treatment Processes	14
2.1	Introduction	14
2.2	Heat Transfer during Quenching	16
2.3	Materials Used in the Present Work	18
2.4	Some Aspects of the Physical Metallurgy of Aluminum Alloys	19
2.5	Thermo-Mechanical Constitutive Laws	22
2.6	Stress-Strain Curves for Aluminum Alloy A356.0	23
2.7	Stress-Strain Curves for Steels S355 and C45E	26
2.8	Temperature Dependence of Thermophysical and Mechanical Properties	27
2.8.1	Introduction	27
2.8.2	Young's Modulus and Poisson's Ratio	28
2.8.3	Coefficient of Thermal Expansion	29
2.8.4	Mass Density	33
2.8.5	Thermal Conductivity	33
2.8.6	Specific Heat	34
2.9	Consistent System of Units	35
3	Thermal Contact Conductance	38
3.1	Introduction	38
3.2	Conduction through the Actual Contact Spots	40
3.3	Heat Transfer through the Interstitial Gas	41
3.3.1	Relevance of Heat Transfer through Natural Convection	43
3.3.2	Heat Transfer through Conduction through the Interstitial Gas	44
3.4	Radiation	46
3.5	Total Thermal Contact Conductance at a Steel-Aluminum Interface . .	47
3.6	Sequentially Coupled and Fully Coupled Problems	48
3.7	Example	49
3.8	Summary and Concluding Remarks	52
4	A Ductile Failure Damage Indicator	54
4.1	Introduction	54
4.2	Damage Indicator Used in this Study	55
4.3	Discussion	56
5	Stress Singularities in Multi-Material Structures	57
5.1	Introduction	57
5.2	Mathematical Description	58
5.3	Dundurs Parameters	60

Contents

5.4	Design Charts	61
5.5	End Point of a Perfectly Bonded Interface	63
5.5.1	Introduction	63
5.5.2	Design Chart	64
5.5.3	Examples	69
5.5.4	Some Remarks on Interface Cracks	75
5.6	Corner in a Perfectly Bonded Interface	79
5.6.1	Introduction	79
5.6.2	Design Chart	80
5.6.3	Example	81
5.7	Wedge Frictionally Sliding on a Body with Smooth Surface	82
5.7.1	Introduction	82
5.7.2	Design Charts	84
5.7.3	Examples	88
5.7.4	Some Remarks on Fretting Fatigue	89
5.8	Closing Remarks	91
5.8.1	Upper Limit for the Singularity Exponent	91
5.8.2	Wedge Solver	92
5.9	Summary	93
6	Step-Bars with Axisymmetric Inserts	95
6.1	Introduction	95
6.2	Finite Element Simulation of Quenching and Mechanical Testing	96
6.3	Simulation Results and Comparison to Experimental Data	99
6.4	Discussion	103
7	Demo Prototype of a Compound Casting	104
7.1	Introduction	104
7.2	Geometry and Manufacturing Process	104
7.3	Simulation of Quenching, Machining and Mechanical Testing	109
7.4	Simulation Results and Comparison to Experimental Data	111
7.5	Discussion	114
8	Conclusion and Outlook	117
	Appendices	121
A	Cubic Splines Approximating Stress-Strain Curves	122
B	Polynomials Approximating Thermophysical and Mechanical Properties	127
C	Additional Design Charts	132
D	Boundary Conditions for Torsional Loading	135

Chapter 1

Introduction

This thesis was prepared in conjunction with the author's participation in the research project *Austrian Light Weight Structures*, funded by the Austrian Research Centers and the Austrian National Foundation. This collaborative research & development project addressed the development of various lightweight multi-material structures. The sub-project that the author participated in focused on steel-aluminum structures manufactured by *compound casting*. It was carried out at the Institute of Lightweight Design and Structural Biomechanics in close collaboration with Leichtmetallkompetenzzentrum Ranshofen (LKR)⁽¹⁾ and the Institute of Materials Science and Technology at the Vienna University of Technology⁽²⁾.

Lightweight design has become very important for a great variety of industrial applications. In recent years interest in lightweight multi-material concepts has grown remarkably. For instance, the SuperLIGHT-CAR project⁽³⁾ has a multi-material philosophy [Goede et al., 2008].

The multi-material concept strives to use the “best” material and manufacturing process for each part of a structure in order to combine the advantages of different materials. Obviously, joining techniques play a major role in the manufacturing of these structures.

The compound casting process allows for the joining of a casting to other parts during the casting process. That is, the casting process serves at the same time as a production and a joining process.

A spectacular example of a compound casting is the magnesium-aluminum crankcase of BMW's inline six-cylinder engine. An aluminum casting containing the cylinders serves as a core around which the crankcase is cast in a magnesium alloy. [Klütting and Landerl, 2004]

⁽¹⁾ <http://www.lkr.at>

⁽²⁾ <http://info.tuwien.ac.at/E308>

⁽³⁾ SuperLIGHT-CAR is a collaborative research & development project co-funded by the European Union. It aims for the realization of multi-material lightweight vehicle structures. <http://www.superlightcar.com>

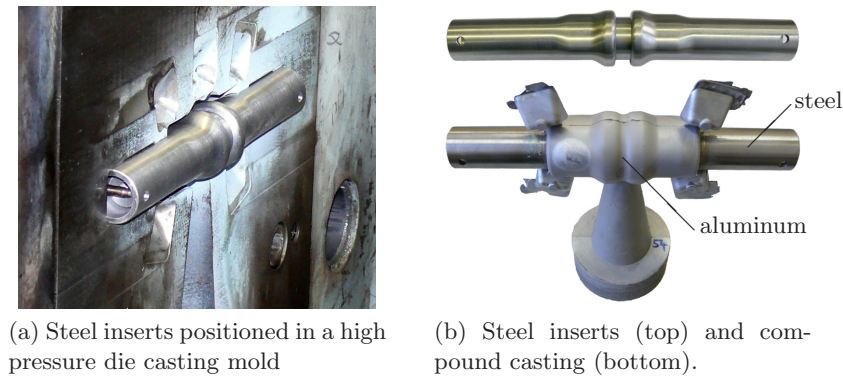


Figure 1.1: A steel-aluminum compound casting. Pictures courtesy of Leichtmetallkompetenzzentrum Ranshofen.

Figure 1.1 shows a steel-aluminum compound casting. Two steel inserts are positioned in a high pressure die casting mold. During the casting process the liquid aluminum fills the space between the mold and the inserts and a mechanical connection is formed.

1.1 Joining Fundamentals

Three main principles permit the joining of different materials: form-locking connection, frictional connection and material-locking connection.

A *form-locking connection* is achieved through the geometrical shape of the connected parts. A dovetail joint is a typical example. With respect to compound castings, a form-locking connection is a natural choice as complex shapes and undercuts can be easily achieved.

A *frictional connection* is achieved through static friction between the connected parts. If two materials with a very different coefficient of thermal expansion (e.g. steel and aluminum) are connected using a compound casting process, large residual stresses can develop during the cooling of the casting, resulting in a strong frictional connection.

A *material-locking connection* is achieved through atomic or molecular forces. With respect to compound casting of metals, a diffusion and/or reaction zone may form at the interface when the liquid material comes into contact with the solid material. Ideally, a continuous metallurgical bond between the two materials is achieved.

In the solid state, iron as well as aluminum are covered by a natural oxide layer. If a part made from one of these materials comes into contact with liquid aluminum or magnesium during a compound casting process, the oxide layer prevents the formation of a continuous metallurgical bond. Consequently, no material-locking connection is obtained [Fragner et al., 2008]. In order to achieve a material-locking connection, the oxide layer needs to be removed prior to the casting process and reoxidation must be

prevented. Advice on how to remove the oxide layer and achieve a material-locking connection for the material combinations steel-aluminum, aluminum-magnesium (with magnesium as liquid material) and aluminum-aluminum can be found in [Fragner et al., 2008] and [Papis et al., 2008].

If metallurgical bonding is achieved during a steel-aluminum compound casting process, a thin layer of intermetallic phases⁽⁴⁾ is formed at the interface [Fragner et al., 2006]. These intermetallic phases are known to be brittle at room temperature⁽⁵⁾. That is, a crack in the layer of intermetallic phases can easily propagate along the interface. It is generally accepted that the intermetallic layer thickness should be kept below a critical thickness of about $10\ \mu\text{m}$ in order to limit the detrimental effects of the brittle intermetallics [Potesser et al., 2006], [Borrisutthekul et al., 2007].

It is difficult to achieve a perfect, continuous metallurgical bond during a real, industrial compound casting process. Therefore, it is sometimes suggested that the material-locking connection should merely be used in addition to a form-locking and/or frictional connection. It should, however, be kept in mind that a crack in the brittle layer of intermetallic phases may not only propagate along the interface but also deflect into one of the two adjacent materials [Gross and Seelig, 2007]. Therefore, it is very well possible that an additional (imperfect) metallurgical bond results in a reduction of the structure's load carrying capacity as compared to a purely form-locking and/or frictional connection.

1.2 Aim and Outline of the Thesis

The aim of this thesis is to develop computational methods for the analysis and design of compound castings and other multi-material structures. Both finite element methods and asymptotic analysis techniques are used.

The thesis is organized as follows.

Chapter 2 deals with the finite element analysis of quenching and other heat treatment processes of compound castings. During the quenching (or cooling) of a compound casting residual stresses develop. As these stresses determine the frictional connection and other important characteristics (e.g. the fatigue life) of the structure, the reliable calculation of the residual stresses is of great importance.

A major finding of this thesis is that the consideration of a variable thermal contact conductance is crucial to the simulation of the quenching process of a steel-aluminum compound casting without material-locking connection. Therefore, *Chapter 3* gives a

⁽⁴⁾Intermetallic phases are compounds of two or more metals that have a certain composition and a crystal structure that is different from that of the constituent metals [Schulze, 1967]

⁽⁵⁾For instance, Sritharan et al. [2000] report a value of $2.0\ \text{MPa m}^{1/2}$ for the mode-I fracture toughness of the four intermetallic compounds Fe_2SiAl_8 , FeSiAl_5 , FeSiAl_3 and FeSi_2Al_4 .

Chapter 1 Introduction

detailed discussion of the dependence of the thermal contact conductance on contact pressure and gap opening.

A ductile failure damage indicator is used to predict the onset of fracture during the mechanical testing of steel-aluminum compound castings in this dissertation. Therefore, a short description of the concept of damage indicators is provided in *Chapter 4*.

Local stress concentrations can occur due to the abrupt change in material properties at the interface of a multi-material structure. Under the assumptions of linear elasticity theory, these stress concentrations can manifest themselves as stress singularities. *Chapter 5* discusses these stress singularities and develops “design charts” for practical use in the design of multi-material structures.

Chapters 6 and 7 present practical examples of steel-aluminum compound castings together with finite element models for the simulation of the quenching process, machining operations and mechanical tests. The results of mechanical tests are compared to simulation results.

In *Chapters 6*, simple low-pressure die-cast aluminum step-bars with various axisymmetric steel inserts are investigated. In *Chapters 7*, a geometrically more complex high-pressure die-cast steel-aluminum structure is presented. This “demo prototype of a compound casting” is meant to demonstrate the possibilities of the compound casting technology.

Chapter 8 presents a summary and propositions for future research.

Even though extensive use of non-linear finite element analysis is made in this dissertation, no introductory chapter on finite element analysis is included. For an extensive introduction to finite element methods the reader is referred to the book by Bathe [2002].

Chapter 2

Finite Element Analysis of Quenching and other Heat Treatment Processes

2.1 Introduction

When a common casting is quenched, the inhomogeneous transient temperature field induces thermal stresses. These stresses are often large enough to cause local plastic deformation. Due to the plastic strains, a residual stress field remains after complete cooling of the casting. During operation of the casting, the load induced stresses are superimposed onto the residual stress field. Thus, the presence of the residual stress field can either be beneficial or detrimental.

Industrial interest in the simulation of quenching and other heat treatment processes has increased during the last decade. There are several reasons for this. The ever increasing speed of computers now allows for the simulation of geometrically complex parts (e.g. cast aluminum alloy wheels, cylinder blocks, cylinder heads). Furthermore, it was realized that accounting for residual stress fields caused by heat treatment processes can dramatically enhance the accuracy of fatigue analyses. Moreover, the prediction of distortions caused by heat treatment processes is of great interest for certain applications (e.g. cast aluminum wheels).

Figure 2.1 shows a typical sequence of simulation steps when simulating the production and operation of an aluminum casting. First, the casting process is simulated (A). This is usually done using specialized CFD programs (casting simulation software) capable of simulating mold filling and solidification. Often, a general purpose finite element program is used for the remaining steps. Thus, at a short time after complete solidification (when the casting can still be assumed to be stress-free) the temperature field is transferred from the casting simulation program to the general purpose finite element program.

Next, the quenching or cooling process is simulated (B). In the case of quenching, thermal stresses build up so fast that creep and relaxation effects are often neglected and a thermo-elastic-plastic constitutive law is used. In the case of a comparatively slow cooling process, creep and relaxation effects are more important and an appropriate constitutive model is advisable.

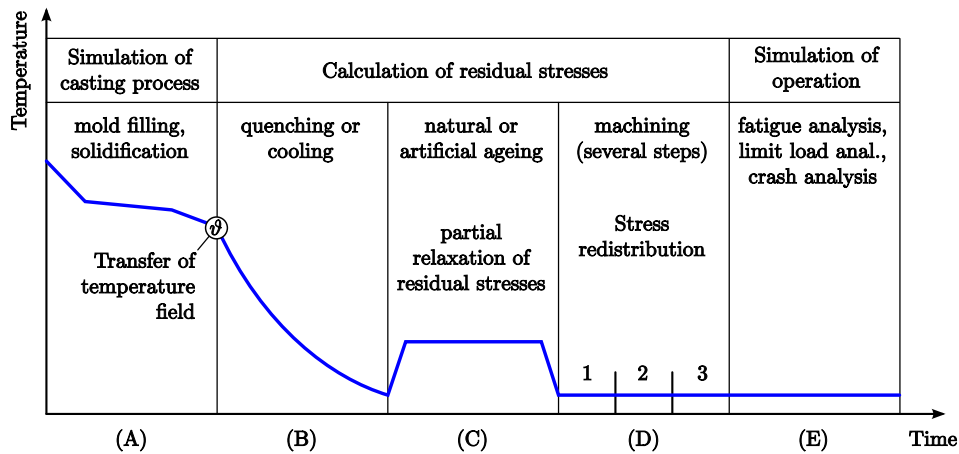


Figure 2.1: Typical sequence of simulation steps when simulating the production and operation of an aluminum casting.

If the cast alloy employed responds to precipitation hardening, natural or artificial ageing is simulated next (C). While stress relaxation does not occur during natural ageing (at room temperature), a certain degree of relaxation of the residual stresses occurs during artificial ageing (at intermediate temperatures).

As last step in the calculation of the residual stress field, potential machining steps have to be simulated. The machining can lead to considerable stress redistributions (D).

Finally, the now known residual stress field is included in the subsequent simulation of operation of the casting, such as fatigue analysis, limit load analysis or crash analysis (E).

Solution treatment can be an additional step in the above described sequence of steps. Also step C (natural or artificial ageing) and step D (machining) can be performed in reversed order.

In the case of a compound casting, knowledge of the residual stress field is especially important, as the residual stresses determine the frictional connection of the structure. When a compound casting is quenched (or cooled down), a residual stress field can develop not only due to the inhomogeneous transient temperature field but also due to the dissimilar coefficients of thermal expansion of the materials involved.

The simulation of heat treatment processes of steel-aluminum compound castings is somewhat simplified by the fact that aluminum alloys do not undergo solid-solid phase transitions and many steels do not undergo solid-solid phase transitions in the relevant temperature range (below the solidus temperature of the aluminum alloy).

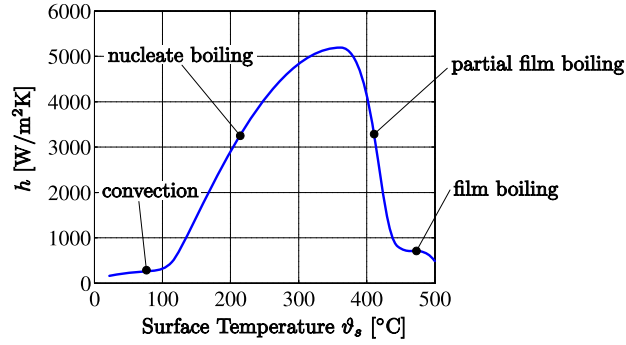


Figure 2.2: Schematic dependence of the heat transfer coefficient h on surface temperature ϑ during quenching; initial temperature: 500°C ; $T_\infty = 20^\circ\text{C}$.

In this chapter some key points regarding the simulation of quenching and other heat treatment processes of steel-aluminum compound castings are highlighted. The last section in this chapter is devoted to the use of a consistent system of units.

The *thermal contact conductance* at the interface of the two materials involved turns out to be an important issue with respect to the simulation of quenching processes of compound castings. As the matter is described in some detail, a whole chapter has been devoted to it, see Chapter 3.

2.2 Heat Transfer during Quenching

Heat transfer during quenching of a hot metallic component in a liquid is a very complex process. A detailed description is beyond the scope of this thesis. More information can be found in [ASM, 1991] and [Maniruzzaman and Sisson, 2004].

Heat transfer between a liquid and a solid is usually characterized in terms of the heat transfer coefficient h :

$$h = \frac{\dot{q}}{T_s - T_\infty}, \quad (2.1)$$

where \dot{q} is the heat flux, T_s is the surface temperature and T_∞ is the temperature of the liquid away from the surface of the solid.

At least four different heat transfer mechanisms are usually distinguished when a metallic component is quenched in a liquid. The four transfer mechanisms correspond to four different temperature ranges as shown schematically in Figure 2.2.

The first stage of cooling, directly after the component has been immersed into the liquid, is characterized by an unbroken vapor film that surrounds the component. This stage is referred to as *film boiling*. As the unbroken vapor film acts as an insulator,

the heat transfer coefficient is low during this stage. The phenomenon is also referred to as Leidenfrost effect⁽¹⁾.

As the surface temperature decreases, the vapor film becomes increasingly unstable and the heat transfer coefficient increases significantly. This stage is referred to as *partial film boiling*. The surface is alternatively covered with a vapor film or liquid. Especially in this stage the heat transfer coefficient in Figure 2.2 can only be seen as an effective value.

As the surface temperature decreases further the partial films are replaced by bubbles and the surface of the component is in permanent contact with the liquid. This stage is referred to as *nucleate boiling*. High values of the heat transfer coefficient are associated with this stage.

Finally, when the surface temperature decreases below the boiling point of the liquid, the *convection stage* starts. Heat transfer coefficients are low as heat is only transferred by (natural or forced) convection.

Besides surface temperature, the heat transfer coefficient depends on a number of factors. Among those are: the properties of the quenching fluid (e.g. boiling point), the temperature of the quenching fluid, the geometry of the quenched component, the orientation of the component during quenching, the fluid agitation level and the surface roughness.

For instance, the film boiling stage is known to be short in cold water (as shown in Figure 2.2) but can be extended considerably when the water temperature approaches the boiling temperature (100 °C).

In practice, establishing values for the heat transfer coefficients is a difficult task. If the component under consideration is physically available, thermocouples can be inserted into the component in order to record temperature curves during a quenching process. The heat transfer coefficients assumed in the simulation can then be adjusted by trial and error until the calculated curves resemble the measured ones. Alternatively, an inverse heat conduction problem can be solved in order to determine the unknown heat transfer coefficients systematically.

For the numerical simulation of a quenching process it is common practice to prescribe the heat transfer coefficient as a function of surface temperature⁽²⁾. Usually, different curves are prescribed on different parts of the component's surface. It should, however, be noticed that this approach can result in inconsistencies. For instance, a film boiling stage (associated with low values of the heat transfer coefficient) is known to occur for a range of different initial surface temperatures (the temperature of the surface when

⁽¹⁾The Leidenfrost effect can be observed in everyday life. A droplet of water that comes into contact with a hot frying pan skitters around and does not evaporate quickly because it is protected by an insulating vapor film.

⁽²⁾Note that radiative heat transfer can also be described using a temperature dependent heat transfer coefficient as shown in Section 3.4.

the component is immersed into the liquid). This effect can not be captured if the heat transfer coefficient is taken to be only a function of surface temperature.

For the curve in Figure 2.2 it was assumed that the temperature of the surface is 500 °C when the component is immersed into the liquid. Let us assume that this curve is used as input for the numerical simulation of a quenching process. The curve might appropriately describe the heat transfer for those parts of the model surface that have a temperature of about 500 °C when the component is immersed into the liquid. However, other parts of the model surface might already have reached a lower temperature (e.g. 400 °C) when the quenching process starts. In the simulation those areas immediately experience high heat transfer coefficients (corresponding to partial film or nucleate boiling) when they should experience an initial film boiling stage.

A solution to the above described problem would consist in a model capable of predicting the heat transfer coefficient during the different stages of a quenching process. Such a model is – to the author’s best knowledge – not yet available. Therefore, the heat transfer coefficients assumed for the simulation of a quenching process remain a source of uncertainty.

2.3 Materials Used in the Present Work

Only one cast aluminum alloy and two different steels have been used in the present work:

- Cast aluminum alloy A356.0 (Aluminum Association⁽³⁾ alloy designation system)
- Steel C45E (European Standard [DIN EN 10083-2], material number: 1.1191)
- Steel S355 (European Standard [DIN EN 10025-2])

The process of finding material properties and other information about an aluminum alloy is complicated by the fact that material designation systems are not internationally standardized. Often, it is worthwhile to look for data about an alloy of equal or approximately equal composition under different designations. Table 2.1 shows a comparison of alloy designations for alloys of approximately equal composition for the alloys 356.0 and A356.0. An extensive comparison of this kind, comprising many standards and alloys, can be found in [Kammer, 2002, Table A.15].

The Aluminum Association (AA) designation system uses a preceding letter (A, B, C, etc.) to indicate small variations in the composition limits. For example alloy 356.0 has variations A356.0, B356.0, and C356.0. Each of these alloys has identical major alloy contents, but has decreasing limits applicable to impurities. The fourth digit in the AA designation system denotes casting (0) or ingot (1, 2). A former AA designation system did not use a period and a fourth digit. An alloy designated A356 may safely be

⁽³⁾The Aluminum Association is a trade association for aluminum manufacturers based in Washington, DC; <http://www.aluminum.org>

AA	DIN EN 1706	BS ¹	SIS ²	CSA ³	JIS ⁴
356.0	EN AC-42000 or EN AC-ALSi7Mg	LM29	4244	SG70N	AC4C
A356.0	EN AC-42100 or EN AC-ALSi7Mg0,3	LM25	-	SG70P	-

¹ British Standard

² Swedish Standard

³ Canadian Standard

⁴ Japanese Standard

Table 2.1: Comparison of alloy designations for alloys of approximately equal composition [Kammer, 2002].

Alloy	356.0		A356.0	
	Nominal	Limits	Nominal	Limits
Si	7.0	6.5-7.5	7.0	6.5-7.5
Mg	0.32	0.20-0.45	0.35	0.25-0.45
Fe	-	≤ 0.6	-	≤ 0.2
Cu	-	≤ 0.25	-	≤ 0.2
Mn	-	≤ 0.35	-	≤ 0.1
Zn	-	≤ 0.35	-	≤ 0.1
Ti	-	≤ 0.25	-	≤ 0.2

Table 2.2: Nominal composition and composition limits of alloys 356.0 and A356.0 in weight percent [Kaufman and Rooy, 2005].

assumed to be A356.0 by the current standard [Kaufman and Rooy, 2005]. Table 2.2 shows the nominal composition and composition limits of alloys 356.0 and A356.0.

2.4 Some Aspects of the Physical Metallurgy of Aluminum Alloys

In this section some aspects of the physical metallurgy of aluminum alloys relevant for the present work are highlighted. The reader already familiar with the subject can skip this section. For an extensive treatment of the physical metallurgy of aluminum alloys and other light metals the reader is referred to the book by Polmear [2006].

The aluminum alloy used in the present work, A356.0, belongs to the group of cast

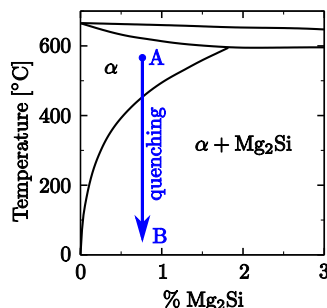


Figure 2.3: Pseudo-binary phase diagram for Al – Mg₂Si [Polmear, 2006].

alloys which respond to *precipitation hardening*. In these alloys a large number of extremely small particles (nanometer range) can precipitate under certain conditions. As these particles can act as obstacles to the motion of dislocations, the strength of the material can be considerably increased.

A precondition for an alloy to respond to precipitation hardening is a decrease in solid solubility of one or more alloying elements. In the case of the Al-Si-Mg-based alloy A356.0, the solid solubility of Mg₂Si decreases with decreasing temperature as shown in Figure 2.3.

The desired fine dispersion of small precipitates is normally achieved through a heat treatment comprising the following three steps:

- Solution treatment at high temperatures (e.g. point A in Figure 2.3); the alloying elements are dissolved and a high concentration of vacancies is generated.
- Fast cooling (quenching) to room temperature (point B in Figure 2.3) produces a super-saturated solid solution of the alloying elements in aluminum. Also, the high concentration of vacancies generated in the previous step is preserved.
- Precipitation of fine particles from the super saturated solid solution at room or elevated temperatures assisted by the high concentration of vacancies.

If the precipitation process takes place at room temperature, the process is referred to as *natural ageing*. If it takes place at elevated temperatures, the process is referred to as *artificial ageing*.

The increase of yield strength associated with natural ageing usually starts immediately after quenching and may, for some alloys, continue for month or even years. In contrast, in the case of artificial ageing yield strength usually increases to a peak value within hours and then decreases. Normally, higher strength can be achieved through artificial ageing than through natural ageing.

The ageing process of Al-Si-Mg-based alloys like A356.0 is particularly complex and not yet fully understood. For an extensive review the reader is referred to the book by Polmear [2006].

With respect to the above described three-step heat treatment process it must be noted that castings produced by high pressure die casting (the economically most important casting process) can normally not be solution treated. This is because gas is entrapped under high pressure in the pores of such a casting. When the casting is heated to high temperatures, the entrapped gases expand, which leads to plastic deformations of the skin (blistering) [Lumley et al., 2007].

The compound castings investigated in the experimental part of this work (manufactured by low pressure die casting, see Chapter 6, and high pressure die casting, see Chapter 7) have not been solution treated. After the casting process they were removed from the mold as early as possible and then immediately quenched. In the subsequent days and weeks the yield stress of the material increases due to natural ageing.

Casting and subsequent quenching leads to a lower degree of supersaturation than solution treatment and subsequent quenching. As a consequence the alloy's ability to be strengthened by natural or artificial ageing is reduced.

Moreover, when the cooling rate after casting is low (cooling in air, delayed quenching, . . .), coarse precipitates may form that do not cause any significant strengthening. Due to the formation of these coarse precipitates the supersaturation in the quenched condition is reduced and, as a consequence, the alloys ability to be strengthened by natural or artificial ageing is diminished.

Figure 2.4 shows the isothermal time-temperature-precipitation diagram for two aluminum alloys containing 7% Si and 0.3% Mg (A356.0) and 7% Si and 0.5% Mg (A356.0 with slightly increased Mg-content), respectively. The lines in Figure 2.4 indicate the limits of precipitate solubility. It can be seen that for an intermediate temperature range of about 200 °C - 400 °C the time for the formation of precipitates is short. This is the critical temperature range for the formation of coarse precipitates and the associated loss of supersaturation during cooling. Thus, especially this temperature range must be passed through quickly in order to retain a high degree of supersaturation and eventually a good response to natural or artificial ageing.

Figure 2.4 also indicates that the cooling rate required to obtain a high degree of supersaturation is higher for an alloy containing 7% Si and 0.5% Mg than for an alloy containing 7% Si and 0.3% Mg. The composition limits of alloy A356.0 are 0.25%-0.45% Mg (see Table 2.2). Thus, two alloys, both within the composition range of A356.0, may respond quite differently to the same thermal history.

In this context it should be mentioned that the strength values that can be attained by natural or artificial ageing, can be estimated based on a known thermal history and a isothermal time-temperature-precipitation diagram (like the one in Figure 2.4) using a method called "Quench Factor Analysis" [Rometsch et al., 2003].

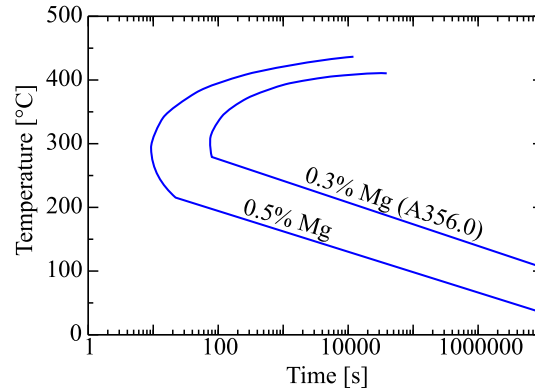


Figure 2.4: Isothermal time-temperature-precipitation diagram for aluminum alloys containing 7% Si and varying amounts of Mg [Kaufman and Rooy, 2005].

2.5 Thermo-Mechanical Constitutive Laws

For the simulation of quenching and other heat treatment processes of an aluminum casting a mechanical constitutive model is required. In many cases an elastic-viscoplastic model (comprising rate-dependent plasticity and creep) would be most appropriate. However, the experimental determination of material parameters associated with such a model is difficult and appropriate material parameters are hardly available in the open literature.

If the process simulated is sufficiently fast, viscous effects can be neglected and a rate-independent elastic-plastic model can be used. This is usually true for the simulation of quenching processes of rather small parts, where the quenched components often reach low temperatures only seconds after immersion into the quenching fluid.

Neglecting viscous effects results in a tendency to overestimate the residual stresses generated by a quenching process. This tendency can be counterbalanced to a certain degree by starting the quenching simulation at a temperature level that is high but markedly below the solidus temperature and assuming that the component is still stress free at that time.

Aluminum castings are either quenched after solution treatment or directly after casting. In the former case, the component usually needs to be transported from the furnace to the quench tank. During that transport the component slowly cools in air, so that the temperature upon immersion into the quench tank will be somewhat below the solution treatment temperature. In the latter case the component first cools in the mold and additionally during the transport from the mold to the quench tank, so that the temperature upon immersion into the quench tank will be markedly below the solidus temperature.

In both cases it is reasonable to start the simulation at the time of immersion of the component into the quenching fluid and to assume that the component is still stress-free at that time. Before immersion, the temperature is high and changes comparatively slowly, so that the build-up of considerable stresses is prevented by relaxation effects. From the time of immersion into the quenching fluid temperature changes rapidly. As a consequence, viscous effects can be neglected and an elastic-plastic constitutive model is applicable.

For the quenching simulations presented in Chapters 3, 6 and 7 von Mises rate-independent plasticity with isotropic hardening and associated flow rule has been assumed. The yield surface is defined by specifying the value of the uniaxial yield stress as a function of accumulated equivalent plastic strain and temperature. Thus, stress-strain curves at a number of different temperatures have to be determined experimentally. Some remarks about the determination of these stress-strain curves and some experimental results for A356.0 are given in the next section.

2.6 Stress-Strain Curves for Aluminum Alloy A356.0

Determining stress-strain curves that appropriately describe the material behavior of A356.0 during the quenching operation by means of a mechanical test (tensile or compressive test) is not trivial as the results can be distorted by unintended precipitation processes.

For instance, if a sample is quenched to room temperature after casting (or after solution treatment) and later heated up to test temperature, precipitation effects can severely affect the results. Unintended precipitation processes can take place at room temperature (before the mechanical test), during the heating of the sample to the test temperature or even during the mechanical test itself. The latter can especially be a problem when mechanical tests are conducted at low strain rates (and thus take a long time) and intermediate temperatures (see Figure 2.4).

Estey et al. [2004] addressed the problem described above and presented a method for determining stress-strain curves more or less unaffected by precipitation processes. In the paper stress-strain curves for A356.0 appropriate for the simulation of a quenching process are given for the temperature range from 200 °C to 500 °C. Together with an appropriate room temperature curve determined in collaboration with Leichtmetallkompetenzzentrum Ranshofen these stress-strain curves served as basis for the thermo-elastic-plastic material model used in this work (see Figure 2.7).

As mentioned before, the compound castings presented in the experimental part of this work (see Chapters 6 and 7) were removed from the mold as early as possible and then immediately quenched. No further heat treatment was performed. In order to estimate the amount of natural (and artificial) ageing to be expected from these



Figure 2.5: Die casting mold (left), quenching of step-bar sample (middle), step-bar sample (right); pictures courtesy of Leichtmetallkompetenzzentrum Ranshofen.

compound castings, a series of experiments has been performed in cooperation with Leichtmetallkompetenzzentrum Ranshofen.

Step-bar samples have been produced from A356.0 by high pressure die casting (see Figure 2.5). One part of the samples was removed from the mold as soon as possible and quenched in water. Another part of the samples was removed from the mold as soon as possible and cooled down in air. Subsequently, tensile test specimens were machined from a part of the samples and room temperature tensile tests were performed. The time between cooldown and the mechanical testing was kept as short as possible (few hours) in order to keep the effects of natural ageing to a minimum and to obtain a room temperature stress-strain curve suitable as input for the simulation of the quenching process. The remaining samples were either naturally aged for three weeks or artificially aged for 7 hours at 180 °C and subsequently mechanically tested. According to ageing curves (Brinell hardness over time) reported by Kliauga et al. [2008], three weeks of natural ageing is sufficient to reach maximum strength. Moreover, the ageing curves given by Kliauga et al. [2008] indicate that the increase in hardness is very small during the first hours of natural ageing, so that the stress-strain curve obtained within few hours after the cool down of the samples closely correspond to the condition directly after casting and quenching.

The tensile test specimens were machined from the 5 mm thick steps of the step-bar samples. This ensures that the thermal history of the sample and the “demo prototype” presented in Chapter 7 is similar, as the wall thickness of the demo prototype is also about 5 mm.

Figure 2.6 shows the 0.2% proof stress determined for the different tempers. The bars labeled “tested immediately” represent mean values from 6 measurements, the other bars represent mean values from 3 measurements. It can be seen that the values of the proof stress determined immediately after quenching and after air-cooling are almost

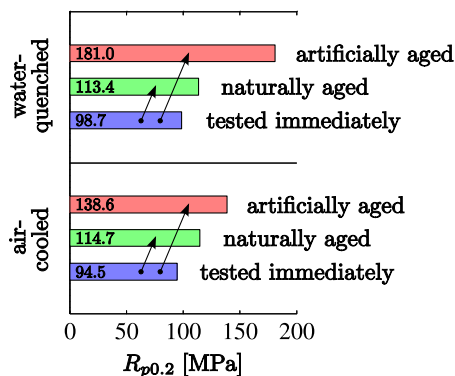


Figure 2.6: 0.2% proof stress of A356.0 in different temps. Bars labeled “tested immediately” represent mean values from 6 measurements, other bars represent mean values from 3 measurements.

identical (98.7 MPa and 94.5 MPa, respectively). Also, the values of the proof stress in the naturally aged condition is almost identical for the quenched and the air-cooled sample (113.4 MPa and 114.7 MPa, respectively). The values of the proof stress in the artificially aged condition, however, is much higher for the quenched than for the air-cooled sample (181.0 MPa and 138.6 MPa, respectively).

It can be concluded that for the casting process and wall thickness considered, the increase of the 0.2% proof stress through natural ageing is in the range of 15-20% (from about 96 MPa to about 114 MPa). Furthermore, this increase does not strongly depend on the cooling rate after casting. Also, the relative increase of the proof stress through natural ageing is in good agreement with the relative increase of the Brinell Hardness reported by Kliauga et al. [2008].

The value of the proof stress after quenching and artificial ageing (181 MPa) is quite close to the value reported for A356.0 after solution treatment, quenching and artificial ageing (T6 condition) by Kaufman and Rooy [2005] (205 MPa).

To obtain a suitable input for the finite element simulations all measured stress-strain curves (the ones taken from [Estey et al., 2004] and the ones determined in collaboration with LKR) have been approximated by cubic splines as shown in Figure 2.7. Curves (1) to (5) have been used for the quenching simulations.

For the sake of reproducibility, the numerical values of the breaks and coefficients defining the splines are listed in Appendix A (page 122). The numbers in brackets in Figure 2.7 refer to rows in Tables A.1 and A.2 in the appendix. The Appendix also contains some basic definitions and considerations about splines.

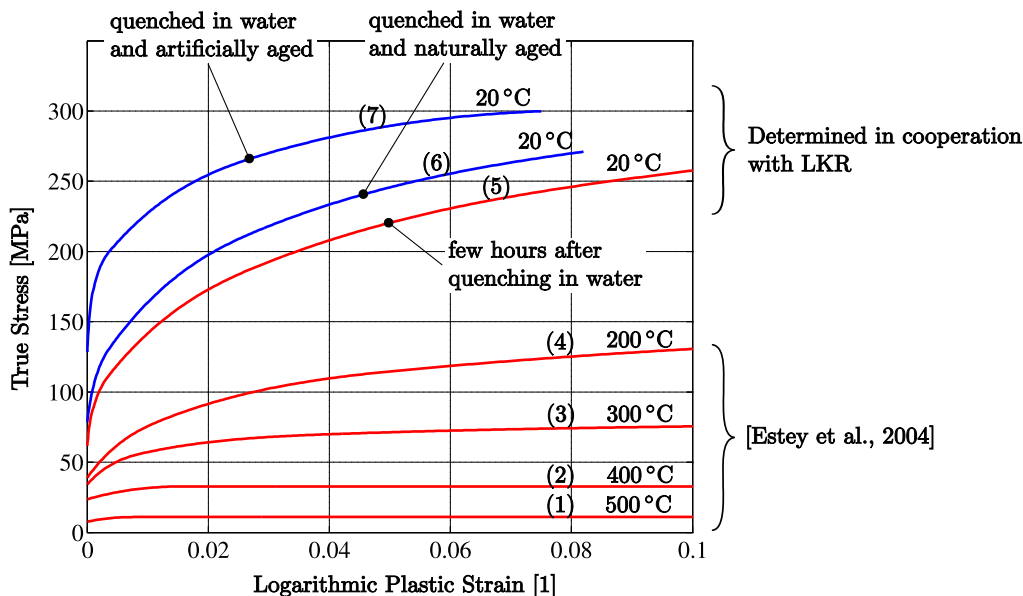


Figure 2.7: Splines approximating stress-strain curves for A356.0; numbers in brackets refer to rows in Tables A.1 and A.2 on pages 124 and 125.

2.7 Stress-Strain Curves for Steels S355 and C45E

For the finite element simulations of quenching processes of compound castings presented in this work, the steel inserts (made from steel S355 and C45E) were assumed to be linear elastic. Inspection of the simulation results confirmed that the von Mises equivalent stress in the steel inserts was always clearly below the yield stress at the respective temperature.

For the simulation of subsequent mechanical tests von Mises plasticity with isotropic hardening and associated flow rule has been assumed, and the stress-strain curves shown in Figure 2.8 have been used for S355 and C45E. The curves have been approximated by splines. The numerical values of the corresponding breaks and coefficients are listed in Table A.3 in Appendix A. The yield stress of C45E is very high as the material was cold drawn.

It should be mentioned that it is by no means clear that plastic deformation of steel inserts does not occur during the quenching or cooling of a steel-aluminum compound casting. For instance, the stresses generated during the cooling of a thick-walled casting surrounding a comparatively thin walled insert (e.g. a thin-walled steel-pipe) can easily plastically deform the insert.

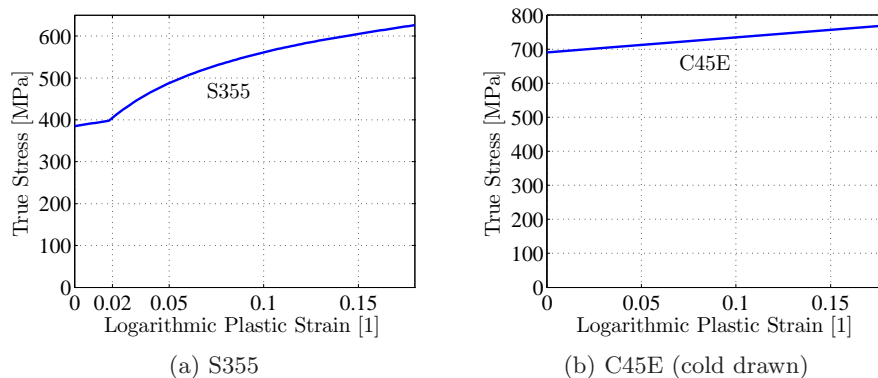


Figure 2.8: Room temperature stress-strain curves for steels S355 and C45E.

2.8 Temperature Dependence of Thermophysical and Mechanical Properties

2.8.1 Introduction

In addition to the mechanical constitutive model discussed in the previous sections, a number of mechanical and thermophysical material properties is required for the simulation of the quenching (or other heat treatment processes) of a compound casting. These are Young's modulus, Poisson's ratio, coefficient of thermal expansion, thermal conductivity, mass density and specific heat of the materials involved.

In this section these material properties are given for aluminum alloy A356.0, steel S355 and steel C45E (see Section 2.3). Low order polynomials are used to approximate the temperature dependence of the properties in the temperature range relevant for quenching simulations⁽⁴⁾. For instance, the temperature dependence of a material property p is described by:

$$p(\vartheta) = a_0 + a_1\vartheta + \dots + a_n\vartheta^n, \quad (2.2)$$

where ϑ is the Celsius temperature.

In some cases coefficients for these polynomials could be taken directly from the literature. In the remaining cases, suitable polynomials were fitted to the literature data by least square approximation. While diagrams showing the temperature dependence of the material properties are included in this section, the numerical values of the polynomial coefficients are listed in Appendix B (page 127).

⁽⁴⁾Solidus temperature of A356.0 is 560 °C Quenching simulations usually start somewhat below that temperature.

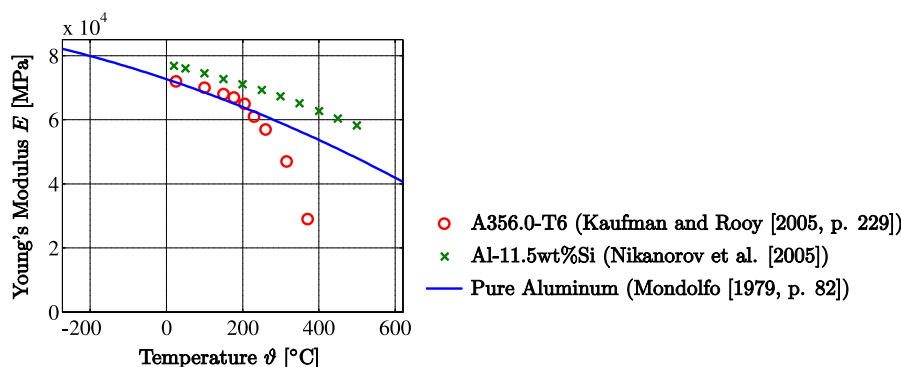


Figure 2.9: Temperature dependence of Young's modulus for A356.0, Al-11.5wt%Si and pure aluminum as reported by different authors.

Finding all required material parameters for a given material in the open literature can be a tedious process. Two sources of information turned out to be especially valuable. First, [SEW 310, 1992] contains thermophysical properties (Young's modulus, coefficient of thermal expansion, specific heat and thermal conductivity) of 72 steels for a large range of temperatures. Also, a comprehensive list of steels not covered by the SEW 310 is given, indicating steels with similar thermophysical properties. The information in SEW 310 is strongly based on the work of Richter [1973, 1991]. Second, [THERPRO], a thermophysical properties database provided by the IAEA⁽⁵⁾, contains thermophysical properties of a large number of materials.

Values for steel S355 were taken from [SEW 310, 1992, Table 13] and for steel C45E from [SEW 310, 1992, Table 15]. The values reported for Young's modulus, coefficient of thermal expansion and specific heat of S355 are identical to those reported for C45E. The values given for thermal conductivities of the two steels differ only slightly.

2.8.2 Young's Modulus and Poisson's Ratio

Values reported in the literature for Young's modulus of aluminum alloys at high temperatures are surprisingly contradictory. Figure 2.9 shows the temperature dependence of Young's modulus for A356.0 (Al-7wt%Si-0.35wt%Mg) as reported by Kaufman and Rooy [2005, p. 229], Al-11.5wt%Si (hypoeutectic binary alloy) as reported by Nikanorov et al. [2005] and pure aluminum as reported by Mondolfo [1979, p. 82].

While the values for Al-11.5wt%Si as reported by Nikanorov et al. are in good agreement with the values for pure aluminum as reported by Mondolfo (the overall slightly higher values are due to the increased silicon content), the values for A356.0 as reported

⁽⁵⁾International Atomic Energy Agency

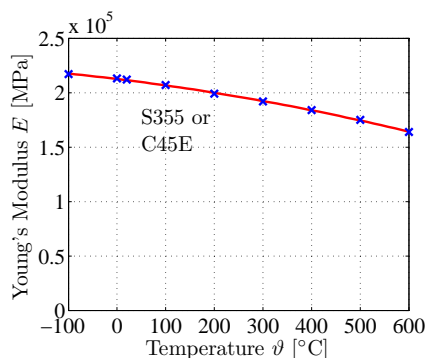


Figure 2.10: Temperature dependence of Young's modulus for S355 or C45E [SEW 310, 1992].

by Kaufman and Rooy are significantly lower at high temperatures⁽⁶⁾. The enhanced drop of the Young's modulus at these high temperatures is in discrepancy with the rule of thumb according to which the Young's modulus of a metal at one-half the melting temperature⁽⁷⁾ in Kelvin becomes 0.8 and at near the melting temperature reaches 0.4 of the value near absolute zero [Sinha, 2003].

For the simulations presented in this work, the well-established data for pure aluminum (as given by Mondolfo [1979]) has been used to describe the temperature dependence of Young's modulus for A356.0. The temperature dependence is described by a second order polynomial (see Figure 2.9) obtained by least square approximation. The polynomial coefficients are given in Table B.1 (page 128) in Appendix B.

Temperature dependence of Young's modulus for steels S355 and C45E was taken from [SEW 310, 1992]. Identical values are reported for both steels. A second order polynomial was fitted to the data - see Figure 2.10 and Table B.3 (page 130) in Appendix B.

Temperature dependence of Poisson's ratio has been neglected for all three materials. Poisson's ratio was assumed to be $\nu_a = 0.33$ for A356.0, and $\nu_s = 0.3$ for steels S355 and C45E.

2.8.3 Coefficient of Thermal Expansion

The coefficient of thermal expansion is an important parameter as thermal expansion is the driving force for thermal stresses. This is especially true for compound castings, where the different thermal expansion of the materials involved is a key issue.

⁽⁶⁾For a temperature of 370 °C the value given by Kaufman and Rooy for A356.0 (29 GPa) is less than half the value given by Nikanorov et al. for Al-11.5wt%Si (64 GPa).

⁽⁷⁾The melting point of high purity aluminum is 660 °C; the melting range of A356.0 is approximately 560 – 615 °C.

Basic Definitions

The linear coefficient of thermal expansion (CTE) relates the change in a material's linear dimensions to a change in temperature. The *instantaneous (or tangent) linear coefficient of thermal expansion* α_i^{th} is defined as:

$$\alpha_i^{\text{th}}(\vartheta) = \frac{d}{d\vartheta} \varepsilon_{\text{th}}(\vartheta), \quad (2.3)$$

where ϑ is the temperature and ε_{th} is the thermal strain. In the following ε_{th} is regarded as an engineering strain and not a true strain. As the thermal strains considered in the present work are small, the two measures do not differ significantly.

From (2.3) it follows that the thermal strain ε_{th} corresponding to a change in temperature from an initial temperature ϑ_i to a temperature ϑ is:

$$\varepsilon_{\text{th}}(\vartheta) = \int_{\vartheta_i}^{\vartheta} \alpha_i^{\text{th}}(\tau) d\tau. \quad (2.4)$$

A different definition – the *total (or secant) linear coefficient of thermal expansion* α_t^{th} – is also commonly used. It is defined as:

$$\alpha_t^{\text{th}}(\vartheta) = \frac{\varepsilon_{\text{th}}^0(\vartheta)}{\vartheta - \vartheta_0}, \quad (2.5)$$

where $\varepsilon_{\text{th}}^0$ is the thermal strain in a sample heated from the reference temperature ϑ_0 to a temperature ϑ . The reference temperature ϑ_0 is often chosen as 20 °C.

Hence, the thermal strain ε_{th} corresponding to a change in temperature from an initial temperature ϑ_i to a temperature ϑ is:

$$\varepsilon_{\text{th}}(\vartheta) = \underbrace{\alpha_t^{\text{th}}(\vartheta)(\vartheta - \vartheta_0)}_{\varepsilon_{\text{th}} \text{ for } \vartheta_0 \rightarrow \vartheta} - \underbrace{\alpha_t^{\text{th}}(\vartheta_i)(\vartheta_i - \vartheta_0)}_{\varepsilon_{\text{th}} \text{ for } \vartheta_0 \rightarrow \vartheta_i} \quad (2.6)$$

Some finite element codes require the instantaneous coefficient of thermal expansion α_i^{th} and others the total coefficient of thermal expansion α_t^{th} . Only if the coefficient of thermal expansion is independent of temperature, the two are identical.

The following relations between α_i^{th} and α_t^{th} can easily be derived:

$$\alpha_t^{\text{th}}(\vartheta) = \frac{1}{\vartheta - \vartheta_0} \int_{\vartheta_0}^{\vartheta} \alpha_i^{\text{th}}(\tau) d\tau, \quad (2.7)$$

$$\alpha_i^{\text{th}}(\vartheta) = \alpha_t^{\text{th}}(\vartheta) + (\vartheta - \vartheta_0) \frac{d}{d\vartheta} \alpha_t^{\text{th}}(\vartheta). \quad (2.8)$$

The temperature dependence of the coefficient of thermal expansion is often approximated by a second order polynomial:

$$\alpha_i^{\text{th}}(\vartheta) = a_0 + a_1\vartheta + a_2\vartheta^2, \quad (2.9)$$

$$\alpha_t^{\text{th}}(\vartheta) = b_0 + b_1\vartheta + b_2\vartheta^2, \quad (2.10)$$

The relations between the polynomial coefficients in (2.9) and (2.10) can be computed using equation (2.8):

$$\begin{aligned} a_0 &= b_0 - b_1 \vartheta_0 , & b_0 &= a_0 + \frac{1}{2}a_1 \vartheta_0 + \frac{1}{3}a_2 \vartheta_0^2 , \\ a_1 &= 2b_1 - 2b_2 \vartheta_0 , & b_1 &= \frac{1}{2}a_1 + \frac{1}{3}a_2 \vartheta_0 , \\ a_2 &= 3b_2 , & b_2 &= \frac{1}{3}a_2 . \end{aligned} \quad (2.11)$$

A356.0 and Pure Aluminum

Kaufman and Rooy [2005, p. 80] give an expression for the linear thermal expansion of A356.0:

$$L_{t(0 \text{ to } 1000^\circ\text{F})} = L_0 [1 + 0.91 (12.19 t + 0.003115 t^2) 10^{-6}] , \quad (2.12)$$

where t is the temperature in Fahrenheit, L_0 is the length at 0°F and L_t is the length at temperature t .

Differentiating (2.12) with respect to t and conversion to $^\circ\text{C}$ yields the instantaneous coefficient of thermal expansion α_1^{th} in $1/^\circ\text{C}$:

$$\alpha_1^{\text{th}}(\vartheta) = \underbrace{20.2938 10^{-6}}_{a_0} + \underbrace{18.3685 10^{-9}}_{a_1} \vartheta , \quad (2.13)$$

where ϑ is the temperature in $^\circ\text{C}$. Using (2.11) the total coefficient of thermal expansion can easily be computed. Choosing a reference temperature of $\vartheta_0 = 20^\circ\text{C}$ we get:

$$\alpha_t^{\text{th}}(\vartheta) = \underbrace{20.4775 10^{-6}}_{b_0} + \underbrace{9.18427 10^{-9}}_{b_1} \vartheta . \quad (2.14)$$

Figure 2.11 shows a plot of Equations (2.13) and (2.14). The two curves intersect at the reference temperature $\vartheta_0 = 20^\circ\text{C}$. Above that temperature the instantaneous coefficient of thermal expansion α_1^{th} is larger than the total coefficient of thermal expansion α_t^{th} .

The measurements corresponding to Equation (2.12) were done in the annealed condition. In the heat treated condition values might be slightly higher. Though it is indicated in [Kaufman and Rooy, 2005] that the applicability of (2.12) is limited to temperatures below 315°C the relation is also used for somewhat higher temperatures in this work.

Blanke [1989, p. 162] gives a polynomial expression for the instantaneous coefficient of thermal expansion of pure aluminum (see Table B.1 in Appendix B). For comparison, Figure 2.12(a) shows the instantaneous coefficient of thermal expansion of pure aluminum and A356.0. Due to the high silicon content of A356.0 its CTE is smaller than the CTE of pure aluminum.

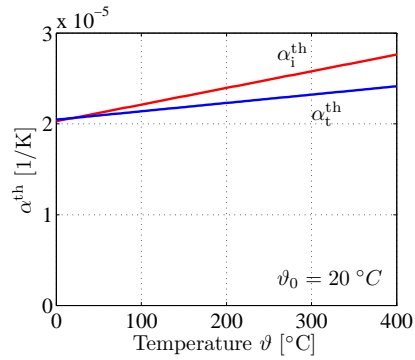
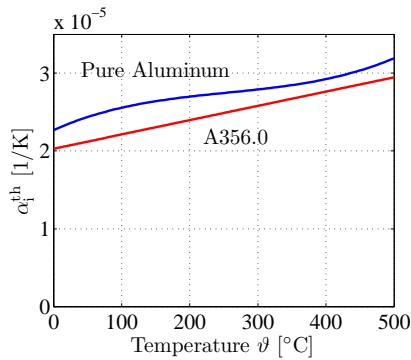
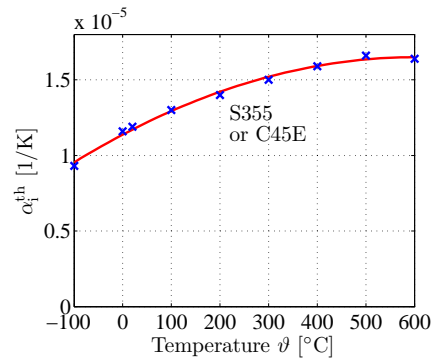


Figure 2.11: Instantaneous coefficient of thermal expansion α_i^{th} and total coefficient of thermal expansion α_t^{th} (reference temperature $\vartheta_0 = 20^\circ\text{C}$) of A356.0 [Kaufman and Rooy, 2005, p. 80].



(a) Pure aluminum [Blanke, 1989] and A356.0 [Kaufman and Rooy, 2005].

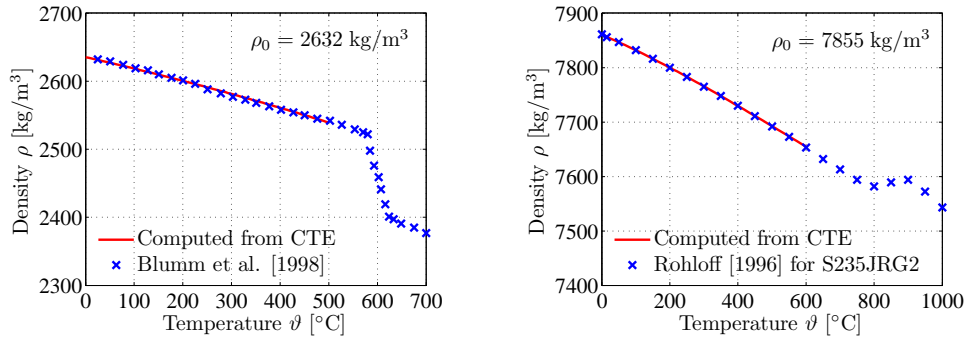


(b) Steel S355 or C45E [SEW 310, 1992].

Figure 2.12: Temperature dependence of the instantaneous coefficient of thermal expansion α_i^{th} .

S355 and C45E

Temperature dependence of the coefficient of thermal expansion for steels S355 and C45E was taken from [SEW 310, 1992]. Identical values are reported for both steels. A second order polynomial was fitted to the data - see Figure 2.12(b) and Table B.3 (page 130) in Appendix B.



(a) A356.0 computed from CTE (see Figure 2.11); data from Blumm et al. [1998] ([THERPRO]) are shown for comparison.

(b) S355 or C45 computed from CTE (Figure 2.12(b)); data for S235JRG2 from Rohloff and Zastera [1996] are shown for comparison.

Figure 2.13: Temperature dependence of mass density ρ .

2.8.4 Mass Density

The dependence of mass density ρ on temperature can be computed from the coefficient of thermal expansion:

$$\rho(\vartheta) = \rho_0 \frac{1}{(1 + \varepsilon_{\text{th}}(\vartheta))^3}, \quad (2.15)$$

where ρ_0 is the density at the initial temperature ϑ_i and the thermal strain $\varepsilon_{\text{th}}(\vartheta)$ is given by Equation (2.4) or (2.6). For small strains (2.15) can be linearized:

$$\rho(\vartheta) = \rho_0 (1 - 3\varepsilon_{\text{th}}(\vartheta)) \quad (2.16)$$

Figure 2.13(a) shows the temperature dependence of mass density ρ of A356.0 as computed from the coefficient of thermal expansion (see Figure 2.11) using Equation (2.15) and assuming a room temperature (20 °C) value of $\rho_0 = 2632 \text{ kg/m}^3$. Data for A356.0 from Blumm et al. [1998] ([THERPRO]) are shown for comparison.

Figure 2.13(b) shows the temperature dependence of mass density ρ of S355 or C45E as computed from the coefficient of thermal expansion (see Figure 2.12(b)) using Equation (2.15) and assuming a room temperature (20 °C) value of $\rho_0 = 7855 \text{ kg/m}^3$. Data for S235JRG2 from Rohloff and Zastera [1996] are shown for comparison.

2.8.5 Thermal Conductivity

The thermal conductivity of aluminum alloys is generally much higher than that of steels.

Figure 2.14 shows the temperature dependence of the thermal conductivity of A356.0 as reported by Blumm et al. [1998] and pure aluminum as reported by Blanke [1989].

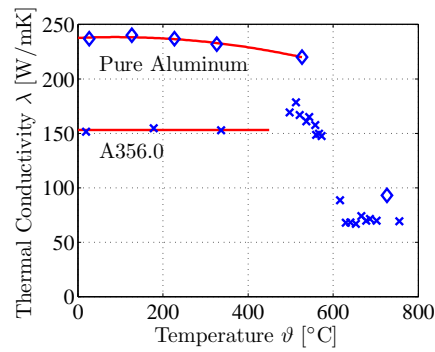


Figure 2.14: Temperature dependence of thermal conductivity λ of pure aluminum [Blanke, 1989] and A356.0 [Blumm et al., 1998], [THERPRO].

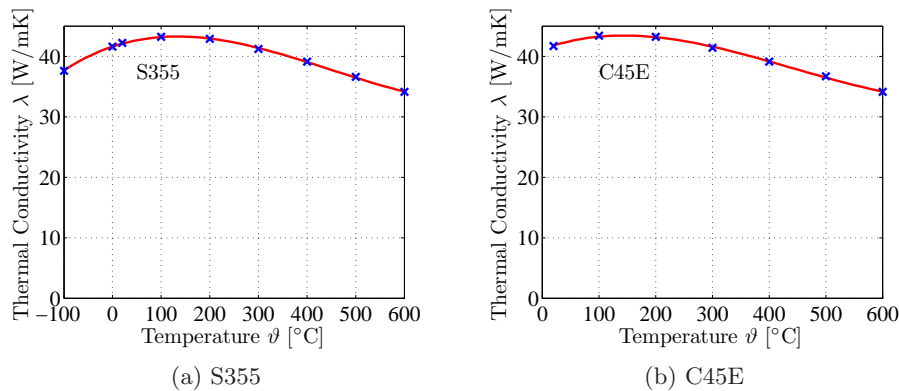


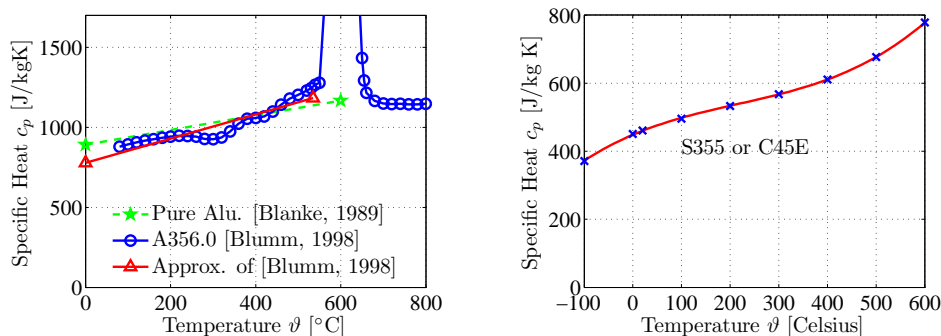
Figure 2.15: Temperature dependence of thermal conductivity λ of S355 and C45E [SEW 310, 1992].

Corresponding polynomial expressions are given in Table B.1 and B.2 in Appendix B (page 128). It can be observed that the thermal conductivity of A356.0 is markedly lower than that of pure aluminum.

Figure 2.15 shows the temperature dependence of the thermal conductivity of S355 and C45E as given in [SEW 310, 1992]. Corresponding polynomial expressions are given in Table B.3 and B.4 in Appendix B (page 130). The thermal conductivities of S355 (Figure 2.15a) and C45E (Figure 2.15b) are almost equal.

2.8.6 Specific Heat

The specific heat capacity is a measure of the amount of energy required to raise the temperature of a unit mass of a material by 1 K. The specific heat of aluminum alloys is considerably higher than the specific heat of steels. However, the *volumetric*



(a) Pure aluminum [Blanke, 1989] and A356.0 [Blumm et al., 1998], [THERPRO]; the peak in the curve for A356.0 corresponds to the heat of fusion.

(b) S355 or C45E [SEW 310, 1992].

Figure 2.16: Temperature dependence of specific heat c_p .

heat capacity (the specific heat multiplied by the mass density) of aluminum alloys is typically lower than or in the same order as the volumetric heat capacity of steels.

Figure 2.16(a) shows the temperature dependence of the specific heat of A356.0 as reported by Blumm et al. [1998], and pure aluminum as reported by Blanke [1989]. Corresponding polynomial expressions are given in Table B.1 and B.2 in Appendix B (page 128).

Temperature dependence of the specific heat for steels S355 and C45E was taken from [SEW 310, 1992]. Identical values are reported for both steels - see Figure 2.16(b). The corresponding polynomial expression is given in Table B.3 in Appendix B (page 130).

2.9 Consistent System of Units

Usually, finite element programs do not handle units of measurement. Instead, a consistent system of units must be used for data input and interpretation of results. The derived units of a consistent system of units can be expressed in terms of the fundamental units of that system without conversions factors. The International System of Units (SI) is an example of such a system.

There are two reasons for not using the SI system for the finite element analyses presented in this work. First, many engineers simply prefer to work with certain non-SI units. For instance, many engineers prefer Megapascal over Pascal as unit of stress. Second, in fully coupled thermal-mechanical problems⁽⁸⁾ the use of certain systems of units can lead to numerically ill-conditioned matrices. Therefore, the manual of

⁽⁸⁾A problem where the mechanical solution depends on the temperature field and vice versa.

the finite element program used for this work, ABAQUS⁽⁹⁾, suggests using Megapascal instead of Pascal as unit of stress for fully coupled problems [Dassault Systèmes, 2008a].

The system of units used in this work is based on the fundamental units millimeter (mm), metric ton (t), second (s) and kelvin (K), and is here denoted as mm-t-s-K system. The unit of stress derived from these fundamental units is Megapascal. Care has to be taken when working with such a system of units – mistakes are easily made. Table 2.3 lists a number of important physical quantities and their respective units in the SI system and the mm-t-s-K system. Each row lists a physical quantity, the exponents of mass, length, time and temperature for that quantity, and the respective units of the quantity.

⁽⁹⁾<http://www.simulia.com>

	Mass	Length	Time	Temp.	SI System (m-kg-s-K)	mm-t-s-K system
Mass	1	0	0	0	kg	t (10^3 kg)
Length	0	1	0	0	m	mm
Time	0	0	1	0	s	s
Temperature	0	0	0	1	K	K
Force	1	1	-2	0	N	N
Stress, Young's modulus	1	-1	-2	0	Pa	10^6 Pa = MPa
Energy	1	2	-2	0	J	10^{-3} J = N mm
Mass density	1	-3	0	0	kg m^{-3}	10^{12} kg m^{-3}
Specific heat capacity	0	2	-2	-1	$\text{J kg}^{-1} \text{K}^{-1}$	10^{-6} $\text{J kg}^{-1} \text{K}^{-1}$
Thermal conductivity	1	1	-3	-1	$\text{W m}^{-1} \text{K}^{-1}$	$\text{W m}^{-1} \text{K}^{-1}$
Heat flux	1	0	-3	0	W m^{-2}	$10^3 \text{W m}^{-2} = \text{kW m}^{-2}$
Heat transfer coefficient, Therm. contact conduct.	1	0	-3	-1	$\text{W m}^{-2} \text{K}^{-1}$	$10^3 \text{W m}^{-2} \text{K}^{-1} = \text{kW m}^{-2} \text{K}^{-1}$
Coeff. of thermal exp.	0	0	0	-1	K^{-1}	K^{-1}

Table 2.3: Unit of some important physical quantities in the mm-t-s-K-system.

Chapter 3

Thermal Contact Conductance

3.1 Introduction

If heat flows from one body into a contacting body, a sudden temperature drop at the interface can frequently be observed, see Figure 3.1. The interface causes a resistance to the heat flow.

The *thermal contact conductance* h is defined as:

$$h = \frac{\dot{q}}{\Delta T} , \quad (3.1)$$

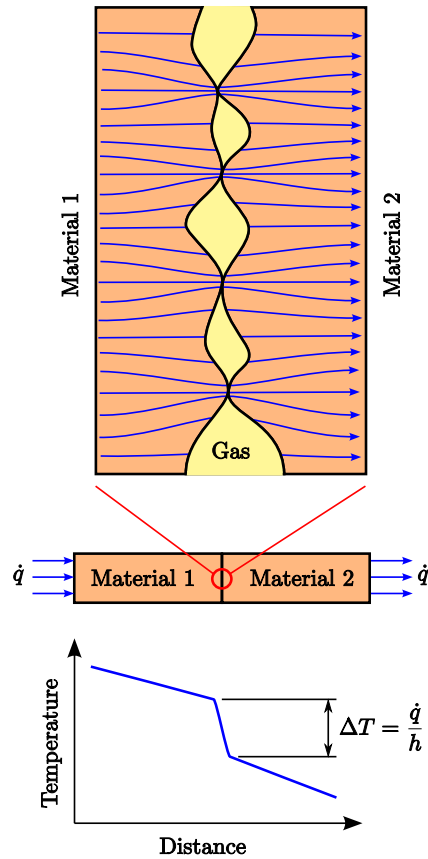
where \dot{q} is the average heat flux flowing through the interface and ΔT is the temperature drop at the interface as shown in Figure 3.1. The reciprocal of the thermal contact conductance is designated as *thermal contact resistance*.

During the cooling or quenching of a compound casting, residual stresses develop. As these stresses determine the frictional connection and other important characteristics (e.g. the fatigue life) of the structure, the reliable calculation of the residual stresses is of great importance. For this purpose, the transient inhomogeneous temperature field that develops during the cooling or quenching has to be determined. As will be shown by means of an example at the end of this chapter, this temperature field may strongly depend on the thermal contact conductance at the interface between the two materials connected.

If metallurgical bonding is achieved at the interface of a steel-aluminum compound casting, a thin layer (in the order of microns) of different intermetallic phases exists between the two materials. The thermal conductivity of this layer is presumably lower, but still of the same order of magnitude as the thermal conductivity of the adjacent metals⁽¹⁾. Consequently, the temperature drop at the interface will be very small, and it will be justified to assume the thermal contact resistance to be zero.

If the interface is not metallurgically bonded, the situation is entirely different. The surface of a casting formed when the liquid metal comes into contact with the surface of

⁽¹⁾For instance, Reddy and Deevi [2000] reported values in the order of 10 W/mK for the thermal conductivity of FeAl.

Figure 3.1: Definition of the thermal contact conductance h .

the mold (or an insert) does *not* simply replicate the microscopic irregularities of these surfaces [Alonso Rasgado and Davey, 2002]. The surface of the casting can actually be rougher or smoother than the surface of the mold (or insert) [Loulou et al., 1999a,b].

Thus, if no metallurgical bonding takes place during the manufacturing of a compound casting, the contact at the interface between the two materials is similar to the common contact of two engineering surfaces. Due to the roughness of these surfaces they will touch each other only in a few points, as shown in Figure 3.1. As heat flow through the contact interface is constrained to these contact spots, the contact interface causes a resistance to the heat flow.

In principle, three mechanisms contribute to the heat transfer through a contact interface: conduction through the actual contact spots, heat transfer through the interstitial gas (e.g. air) and radiation. We assume that it is admissible to split up the total heat flux \dot{q} into the respective parts,

$$\dot{q} = \dot{q}_s + \dot{q}_g + \dot{q}_r, \quad (3.2)$$

where \dot{q}_s is the heat flux due to conduction through the actual contact spots, \dot{q}_g is the heat flux due to conduction through the interstitial gas and \dot{q}_r is the net heat flux due to radiation. Then from Equation (3.1) follows that the total contact conductance h is the sum of the contact conductance due to conduction through the actual contact spots h_s , the contact conductance due to conduction through the interstitial gas h_g and the contact conductance due to radiation h_r :

$$h = h_s + h_g + h_r, \quad (3.3)$$

$$h_s = \dot{q}_s/\Delta T, \quad h_g = \dot{q}_g/\Delta T, \quad h_r = \dot{q}_r/\Delta T. \quad (3.4)$$

These three contributions to the total thermal contact conductance are discussed in the following sections.

Vast literature on thermal contact conductance exists. In this chapter only a few key points are highlighted. For a deeper insight the reader is referred to the book by Madhusudana [1996].

3.2 Conduction through the Actual Contact Spots

The contact conductance due to conduction through the actual contact spots h_s can be seen as the sum of the conductances of the individual spots. Hence, h_s strongly depends on the number and size of these spots, which in turn depend on the contact pressure at the interface as shown schematically in Figure 3.4.

If the number and size of the contact spots is estimated based on theoretical considerations, the contact conductance can be described as a function of the surface parameters, material properties and the contact pressure.

In this work the following expression from [Madhusudana, 1996] (originally introduced by Mikic [1974]) for the case of plastically deformed asperities is used:

$$h_s = 1.13 \lambda \frac{\tan(\theta)}{R_q} \left(\frac{p}{H} \right)^{0.94}. \quad (3.5)$$

In (3.5) p is the contact pressure, H is the microhardness⁽²⁾ (in the unit of stress) of the softer of the two materials, λ is the harmonic mean of the thermal conductivities of the two materials,

$$\lambda = \frac{2 \lambda_1 \lambda_2}{\lambda_1 + \lambda_2}, \quad (3.6)$$

$\tan(\theta)$ is the effective slope of the surface roughness profiles,

$$\tan(\theta) = \sqrt{\tan(\theta_1)^2 + \tan(\theta_2)^2}, \quad (3.7)$$

⁽²⁾As the microhardness H does not refer to a fundamental material property, the magnitude of H is open to some uncertainty.

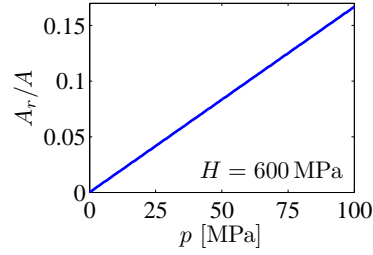


Figure 3.2: Ratio of the real to the apparent area of contact as a function of contact pressure for $H = 600$ MPa.

and R_q is the effective root-mean-square roughness of the surfaces,

$$R_q = \sqrt{R_{q1}^2 + R_{q2}^2}. \quad (3.8)$$

It should be noted that the term p/H in Equation (3.5) is an estimation for the ratio of the real area of contact A_r to the apparent area of contact A at the interface:

$$\frac{A_r}{A} = \frac{p}{H}. \quad (3.9)$$

Assuming $H = 600$ MPa for A356.0 in the as-cast condition Figure 3.2 shows A_r/A as a function of the contact pressure p as described by Equation (3.9). It can be seen that even for relatively high contact pressures the real area of contact is only a small fraction of the apparent area of contact.

The thermal conductivities, λ_1 and λ_2 , and the microhardness H in Equation (3.5) depend on temperature. As a simplification, they are assumed as constant in this work. Table 3.1 lists the material properties and surface parameters used for the evaluation of Equation (3.5). Material 1 is aluminum alloy A356.0 in the as-cast condition, material 2 is steel S355 or C45E. Figure 3.3 shows the resulting contact conductance h_s as a function of the contact pressure p . A strong increase of the contact conductance due to conduction through the actual contact spots with contact pressure can be observed.

3.3 Heat Transfer through the Interstitial Gas

Heat can also be transferred across the interface through the interstitial fluid filling the voids between the actual contact spots. The situation can be represented by an effective gas-filled gap between two parallel surfaces. The width of this microscopic gap is here denoted as d_{mic} – see Figure 3.4, middle and right.

Material 1: Aluminum alloy A356.0 in as-cast condition

Material 2: Steel S355 or C45E

$\lambda_1 = 153 \text{ W/mK}$ [Blumm et al., 1998]

$\lambda_2 = 43 \text{ W/mK}$ [SEW 310, 1992]

$\tan(\theta_1) = \tan(\theta_2) = 0.18$

$R_{q1} = R_{q2} = 4 \mu\text{m}$

$H = 600 \text{ MPa}^{(1)}$ [Zhang et al., 2007b], [El Sebaie et al., 2008]

⁽¹⁾ Microhardness of A356.0 in the as-cast condition

Table 3.1: Material properties and surface parameters for the evaluation of Equation (3.5).

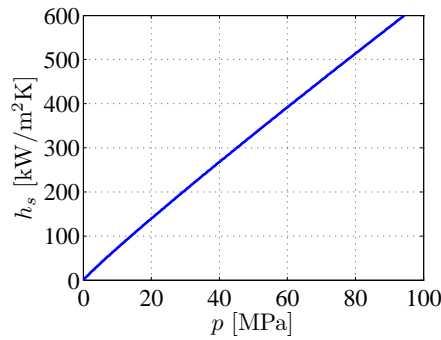


Figure 3.3: Contact conductance due to conduction through the actual contact spots h_s as described by Equation (3.5) and the material properties and surface parameters in Table 3.1.

A macroscopic gap can exist or open up at an interface due to various reasons. (For instance, a macroscopic gap can open up due to the inhomogeneous transient temperature field that develops during the quenching of a compound casting – see Chapter 6) The width of this macroscopic gap is here denoted as d_{mac} – see Figure 3.4, left. The total gap d is then:

$$d = d_{\text{mic}} + d_{\text{mac}} . \quad (3.10)$$

The clearance between two contact surfaces available as output variable in finite element programs corresponds to the macroscopic gap width d_{mac} .

Both conduction and natural convection are possible modes of heat transfer through the interstitial gas. In the next section it is shown that in the majority of cases natural convection heat transfer is negligible so that the heat transfer through the interstitial gas is limited to conduction.

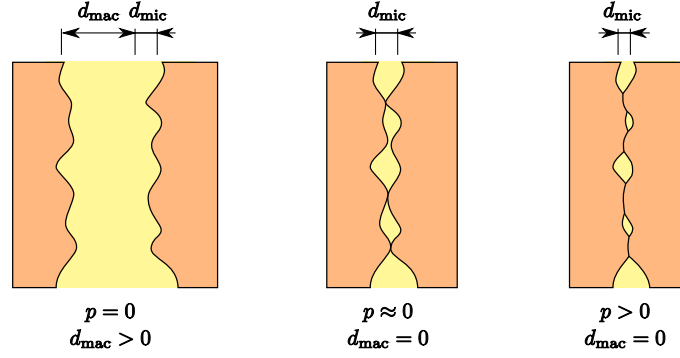


Figure 3.4: Left: open interface ($d_{\text{mac}} > 0$); middle: closed interface ($p \approx 0$); right: closed interface ($p > 0$).

3.3.1 Relevance of Heat Transfer through Natural Convection

Natural convection heat transfer in a narrow gap is negligible if the Rayleigh number,

$$Ra = \frac{g \gamma \Delta T d^3}{\nu a}, \quad (3.11)$$

does not exceed the critical value $Ra_{\text{crit}} = 1700$ [Dittmann, 1995]. The heat transfer through the interstitial gas is then limited to conduction. In (3.11) g is the gravitational acceleration, γ is the volumetric thermal expansion coefficient, ΔT is the difference between the surface temperatures, d is the gap width, ν is the kinematic viscosity and a is the thermal diffusivity. The thermophysical properties of the interstitial gas (γ , ν and a) are evaluated at the average value of the two surface temperatures.

From (3.11) a critical gap width,

$$d_{\text{crit}} = \sqrt[3]{\frac{Ra_{\text{crit}} \nu a}{g \gamma \Delta T}}, \quad (3.12)$$

can be calculated. Natural convection heat transfer is negligible if the gap width is smaller than d_{crit} . Figure 3.5 shows how the critical gap width d_{crit} depends on the difference between the surface temperatures ΔT for air at atmospheric pressure as interstitial gas. Three curves for three different average values ϑ_m of the surface temperatures (20 °C, 300 °C, 500 °C) are shown. The corresponding thermophysical properties of air at atmospheric pressure are given in Table 3.2.

Figure 3.5 clearly shows that even for high values of the temperature difference ΔT and low values of the average temperature ϑ_m the critical gap width d_{crit} is in the range of several millimeters. As gaps of this width do not usually form during a heating or cooling process (see Chapter 6) of a compound casting, the heat transfer through the interstitial gas will normally be limited to conduction.

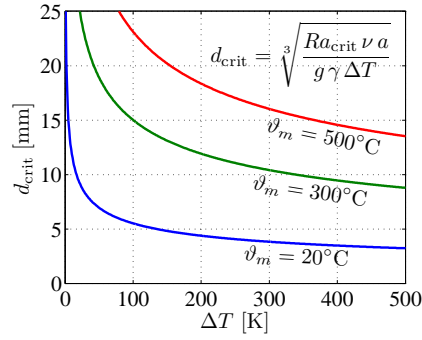


Figure 3.5: Critical gap width d_{crit} for air at atmospheric pressure as interstitial gas. Three curves for three different average values ϑ_m of the surface temperatures are shown.

Temperature		20 °C	100 °C	300 °C	500 °C
Thermal conductivity	λ [W/mK]	$2.57 \cdot 10^{-2}$	$3.14 \cdot 10^{-2}$	$4.41 \cdot 10^{-2}$	$5.56 \cdot 10^{-2}$
Thermal diffusivity	a [m ² /s]	$2.15 \cdot 10^{-5}$	$3.33 \cdot 10^{-5}$	$6.94 \cdot 10^{-5}$	$1.13 \cdot 10^{-4}$
Kinematic viscosity	ν [m ² /s]	$1.54 \cdot 10^{-5}$	$2.35 \cdot 10^{-5}$	$4.92 \cdot 10^{-5}$	$8.14 \cdot 10^{-5}$
Volumetric thermal expansion coefficient	γ [1/K]	$3.42 \cdot 10^{-3}$	$2.68 \cdot 10^{-3}$	$1.75 \cdot 10^{-3}$	$1.29 \cdot 10^{-3}$

Table 3.2: Thermophysical properties of air at $p = 10^5$ Pa [VDI, 2002]

From the thermophysical properties of the interstitial gas appearing in Equation (3.12) the kinematic viscosity ν and the thermal diffusivity a clearly depend on pressure. Both, ν and a decrease with increasing pressure, so that d_{crit} becomes smaller when pressure increases.

3.3.2 Heat Transfer through Conduction through the Interstitial Gas

The situation of heat being conducted through the interstitial gas can be represented by an effective gas-filled gap of width d between to parallel surfaces as explained in Section 3.3. Figure 3.6 shows the temperature distribution within the gas.

If the gap width is very small, namely of the same order of magnitude as the mean free path of the gas molecules⁽³⁾, the effect of *temperature jump* becomes important. The temperature jump is caused by the incomplete energy transfer between the gas molecules and the molecules of the adjacent solid material. The *temperature jump*

⁽³⁾The mean free path of air molecules is of the order of $0.07 \mu\text{m}$ at atmospheric pressure.

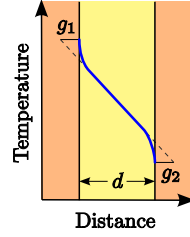


Figure 3.6: Temperature distribution within the gas if the gap width is of the same order of magnitude as the mean free path of the gas molecules.

distance is then the distance by which the gap width d is apparently increased. In Figure 3.6 the temperature jump distances are denoted as g_1 and g_2 .

Thus, for the contact conductance due to conduction through the interstitial gas Fourier's Law of heat conduction yields:

$$h_g = \frac{\lambda_g}{d + g_1 + g_2}, \quad (3.13)$$

where λ_g is the thermal conductivity of the gas, d is the mean (or effective) gap width and g_1 and g_2 are the temperature jump distances. The temperature jump distances must be accounted for if either the surfaces of the solid material are very smooth or the gas pressure is low. If the surfaces of the solid materials are very smooth, the microscopic gap width d_{mic} becomes very small and could be of the same order of magnitude as the mean free path. On the other hand, if the gas pressure is low, the mean free path becomes large and could be of the same order of magnitude as the microscopic gap d_{mic} even for rough surfaces. In this work it is assumed that neither is the case and the temperature jump distances are neglected. Equation (3.13) then reads:

$$h_g = \frac{\lambda_g}{d}. \quad (3.14)$$

A comprehensive treatment of the subject of temperature jump and expressions for the calculation of the temperature jump distance can be found in [Madhusudana, 1996].

Similar to the real area of contact (see Section 3.2), the microscopic gap width d_{mic} depends on the contact pressure. However, the variation of d_{mic} with contact pressure is relatively small. Therefore, as a simplification, a constant d_{mic} is assumed in this work:

$$d_{\text{mic}} = 2.7 R_q, \quad (3.15)$$

where R_q is the effective root-mean-square roughness of the surfaces as defined by Equation (3.8). The relation in Equation (3.15) was established experimentally by Wahid and Madhusudana [2000] using a contact pressure of 0.433 MPa.

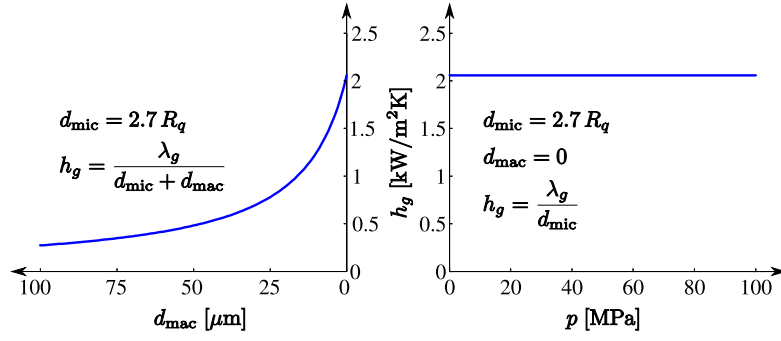


Figure 3.7: Contact conductance due to conduction through the interstitial gas as a function of the macroscopic gap width and the contact pressure. $R_q = 5.66 \mu\text{m}$, $\lambda_g = 3.14 \cdot 10^{-2} \text{ W/mK}$.

As a further simplification a constant thermal conductivity of the gas λ_g in Equation (3.14) is assumed in this work. The dependence of λ_g on temperature (on to a certain extend on gas pressure) is neglected.

Finally, using the surface roughness values given in Table 3.1 and the thermal conductivity of air at 100°C given in Table 3.2, Figure 3.7 shows the contact conductance due to conduction through the interstitial gas, h_g , as a function of the macroscopic gap width d_{mac} and the contact pressure p . For a closed interface ($d_{\text{mac}} = 0$) h_g does not depend on contact pressure, because d_{mic} is assumed constant.

3.4 Radiation

The net radiative heat flux across a narrow gap between two surfaces is given by:

$$\dot{q}_r = \sigma C (T_1^4 - T_2^4) \quad (3.16)$$

with

$$C = \left(\frac{1}{\varepsilon_1} + \frac{1}{\varepsilon_2} - 1 \right)^{-1}, \quad (3.17)$$

where $\sigma = 5.6704 \cdot 10^{-8} \text{ W/m}^2\text{K}^4$ is the Stefan-Boltzmann constant, ε_1 and ε_2 are the surface emissivities and T_1 and T_2 are the absolute surface temperatures.

This can be rewritten in the following form:

$$\dot{q}_r = \underbrace{4\sigma C T_m^3}_{h_r} (T_1 - T_2) \quad (3.18)$$

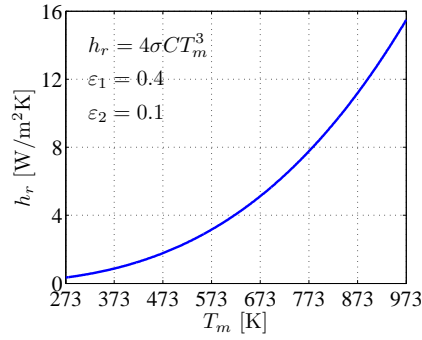


Figure 3.8: Contact conductance due to radiative heat transfer h_r as a function of the mean temperature T_m for $\epsilon_1 = 0.4$ and $\epsilon_2 = 0.1$.

with

$$T_m = \sqrt[3]{\frac{T_1 + T_2}{2} \frac{T_1^2 + T_2^2}{2}}, \quad (3.19)$$

where T_m is a mean temperature in the sense that T_m always lies between T_1 and T_2 . From (3.18) it can be seen that the net radiative heat flux \dot{q}_r increases with increasing mean temperature T_m and with increasing temperature difference $T_1 - T_2$. The term $h_r = 4\sigma CT_m^3$ in (3.18) can be interpreted as a temperature dependant contact conductance due to radiative heat transfer. Figure 3.8 shows h_r as a function of the mean temperature T_m assuming $\epsilon_1 = 0.4$ (steel) and $\epsilon_2 = 0.1$ (aluminum). Even for temperatures as high as the melting point of aluminum (933 K, 660°C), the values of h_r are much smaller than typical values of the thermal contact conductance associated with conduction through the actual contact spots or conduction through an interstitial gas (compare Figure 3.3 and 3.7). Thus, in many cases it will be well justified to completely neglect the contribution of radiative heat transfer to the thermal contact conductance.

3.5 Total Thermal Contact Conductance at a Steel-Aluminum Interface

In this section the total thermal contact conductance, h , at a steel-aluminum interface is established. The material properties used are that of steel S355 or C45E and aluminum alloy A356.0. Air at atmospheric pressure is assumed as the interstitial gas. The material properties and surface parameters of the solid materials are given in Table 3.1, the properties of air are given in Table 3.2.

As only the microhardness of the softer of the two materials (the aluminum alloy) enters Equation (3.5), and the thermal conductivity of S355 and C45E are almost identical

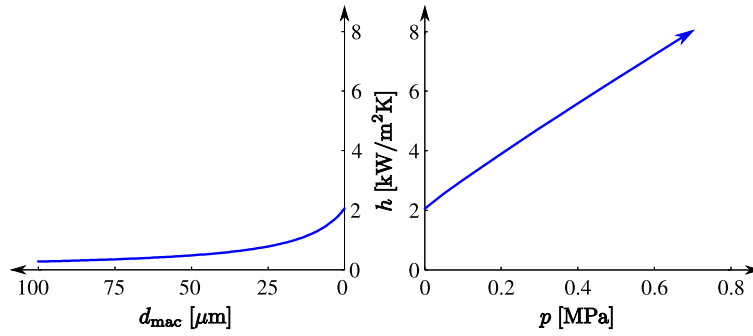


Figure 3.9: Total thermal contact conductance at a steel-aluminum interface.

(SEW 310 [1992]), the values of the contact conductance depicted in this section are applicable to both material combinations: S355-A356.0 and C45E-A356.0.

Besides the assumptions highlighted in the previous sections, the following assumptions were made:

- Natural convection heat transfer through the interstitial gas is neglected – see Section 3.3.1.
- Radiative heat transfer is neglected - see Section 3.4.

The total thermal contact conductance is then the sum of the contact conductance due to conduction through the actual contact spots as described by Equation (3.5) and the contact conductance due to conduction through the interstitial gas as described by Equation (3.14). Figure 3.9 shows the total thermal contact conductance as a function of the macroscopic gap width d_{mac} and the contact pressure p . Figure 3.9 is obtained by adding the curve in Figure 3.3 (on page 42) the corresponding curve in Figure 3.7 (on page 46).

3.6 Sequentially Coupled and Fully Coupled Problems

If a mechanical problem involving heat transfer is analyzed, the thermal problem and the mechanical problem can either be *sequentially coupled* or *fully coupled*. In the former case the mechanical solution (displacements, stresses) depends on the temperature field but there is no inverse dependency. Hence, the pure heat transfer problem can be solved first and the mechanical problem is then solved using the now known temperature field. In the latter case the mechanical solution depends on the temperature field and vice versa. Thus, the heat transfer problem and the mechanical problem have to be solved simultaneously.

If the dependence of the thermal contact conductance on the contact pressure and the macroscopic gap opening is accounted for, the thermal and the mechanical problem are obviously fully coupled.

In terms of finite element analysis such a fully coupled problem usually requires more computational time and more main memory than a sequentially coupled problem. While in general these additional costs can and should not be avoided (see the example in the following section), it might be very beneficial to avoid either the additional computational time or the additional memory requirements in certain situations. For these cases the following procedure is suggested:

- A plausible constant value h_0 of the thermal contact conductance is chosen and a sequentially coupled analysis is performed.
- Using the resulting values of the contact pressure and the macroscopic gap opening at the interface, the “correct values” of the thermal contact conductance h are computed (compare Figure 3.9).
- Finally, the “correct values of the temperature drop” $\Delta T = \dot{q}/h$ are computed.

If the difference between the correct value of the temperature drop and the temperature drop used in the analysis ($\Delta T_0 = \dot{q}/h_0$) remains small everywhere throughout the analysis, chances are that the results of the sequentially coupled analysis are acceptable. This might especially be the case when:

- Heat fluxes are generally low (e.g. a casting is cooled down in air). The temperature drop at the interface may then always be very low.
- The magnitude of the heat fluxes is not low, but heat fluxes are mainly parallel to the interface in question.
- The contact pressure at the interface is high throughout all the analysis, so that h is also high and the temperature drop is small (see the example in the following section).

3.7 Example

The example presented in this section emphasizes the importance of accounting for a variable thermal contact conductance when simulating the quenching process of a compound casting without metallurgical bonding. Fundamental considerations regarding the simulation of the quenching process of a compound casting have been given in Chapter 2 and 3. The general purpose finite element program ABAQUS Standard⁽⁴⁾ [Dassault Systèmes, 2008a] has been used to carry out the simulations.

⁽⁴⁾<http://www.simulia.com>

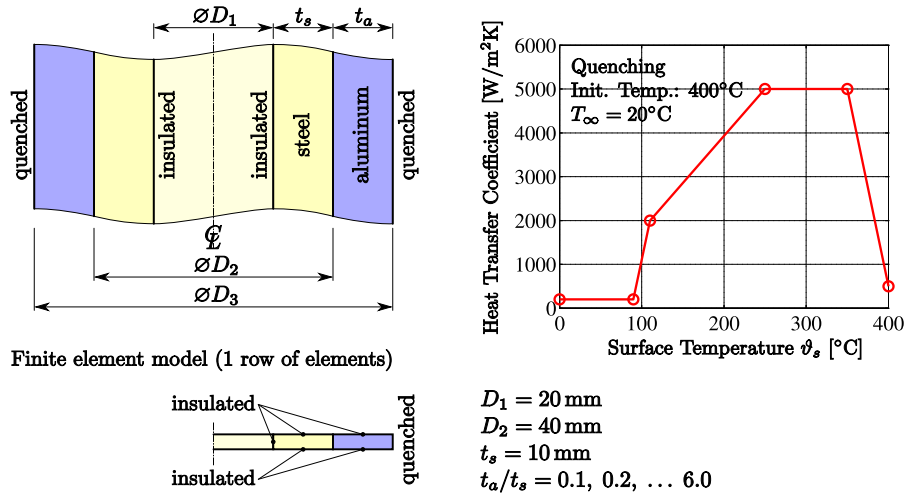


Figure 3.10: Simulation of the quenching process of an axisymmetric generic structure (tubular steel insert surrounded by an aluminum casting).

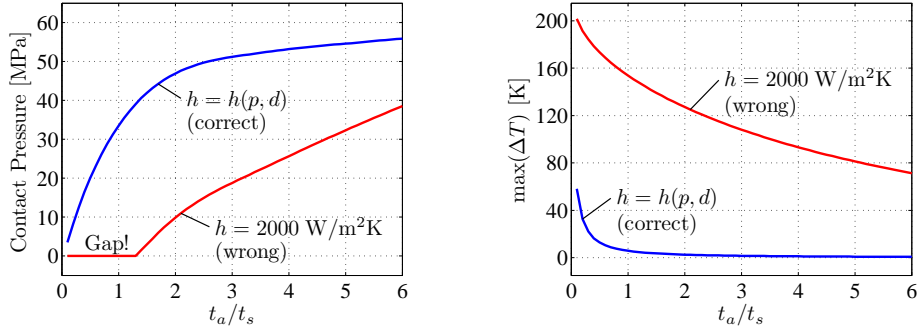
The axisymmetric generic structure shown in Figure 3.10 is considered. It consists of a tubular steel insert with outer diameter $D_2 = 40 \text{ mm}$, wall thickness $t_s = 10 \text{ mm}$, surrounded by an aluminum casting with wall thickness t_a . The ratio t_a/t_s is varied from 0.1 to 6.0. Frictionless contact is assumed at the steel-aluminum interface and plane stress is assumed in the axial direction. As the problem is one-dimensional, a finite element model consisting of a single row of axisymmetric elements⁽⁵⁾ is sufficient.

The insert and the casting are assumed to be made from steel S355 and aluminum alloy A356.0, respectively. Information on both materials can be found in Section 2.3. Von Mises rate-independent plasticity with isotropic hardening is assumed for both materials (see Section 2.5). Stress-strain curves for the relevant temperature range are given in Figure 2.7 on page 26 for A356.0 and in Figure 2.8(a) on page 27 for S355. Further required thermophysical and mechanical material properties are given in Section 2.8.

The simulation starts at the time of immersion of the structure into the quenching water. At that time, it is assumed that both components (insert and casting) exhibit a homogeneous temperature of 400 °C and that the structure is still stress-free.

Only the outer surface of the casting is assumed to be in contact with the quenching water. The heat transfer coefficient is taken as a function of the surface temperature as shown in Figure 3.10. The inner surface of the steel insert is assumed insulated. For this choice of thermal boundary conditions, the magnitude of the thermal contact conductance at the steel-aluminum interface is of particular importance as all thermal

⁽⁵⁾ABAQUS element type CAX4T: 4-node, linear, coupled temperature-displacement element



(a) Contact pressure at the steel-aluminum interface after complete cooling.

(b) Magnitude of the maximum temperature drop that occurred at the steel-aluminum interface during the quenching process.

Figure 3.11: Simulation results.

energy difference between hot and cooled-down situation initially stored in the steel insert must flow through that interface during the quenching process.

For the thermal contact conductance h at the steel-aluminum interface two different assumptions are considered:

- Thermal contact conductance is taken as a function of contact pressure and macroscopic gap width, $h = h(p, d)$, as described in Section 3.5 and shown in Figure 3.9.
- A constant value of $h = 2000 \text{ W/m}^2\text{K}$ is assumed.

A constant value of $h = 2000 \text{ W/m}^2\text{K}$ is (approximately) the value obtained for zero contact pressure in Section 3.5. It is also a typical value used at the metal-mold interface for the simulation of casting processes, see for instance [Zhang et al., 2007a].

Figure 3.11 shows simulation results. Figure 3.11(a) shows the contact pressure at the steel-aluminum interface after complete cooling. For variable thermal contact conductance, the contact pressure rises from 3.5 MPa to 56 MPa for t_a/t_s ranging from 0.1 to 6.0. Considerably lower values of the contact pressure are predicted for a constant value of $h = 2000 \text{ W/m}^2\text{K}$. In fact, for $t_a/t_s < 1.3$ zero contact pressure (a gap) at the steel-aluminum interface is predicted!

This can be understood by looking at Figure 3.11(b), where the magnitude of the maximum temperature drop that occurred at the steel-aluminum interface during the quenching process is shown.

In the case of variable thermal contact conductance, the maximum temperature drop remains comparatively small. That is because contact pressure at the steel-aluminum interface increases to several MPa during an early stage of the quenching simulation. As a consequence, the thermal contact conductance rises to high values (see Figure 3.9) and the temperature drop at the interface remains small.

By contrast, in the case of a constant value of $h = 2000 \text{ W/m}^2\text{K}$, temperature drops of up to 200°C are predicted. That is, the aluminum casting is plastically deformed while it “shrinks on” to the still comparatively hot steel insert. When the steel insert finally cools down, the contact pressure at the steel-aluminum interface is decreased. For $t_a/t_s < 1.3$ the contact pressure decreases to zero and a gap opens up!

It must be concluded that the use of constant value of the thermal contact conductance in the order of $h = 2000 \text{ W/m}^2\text{K}$ is *not suitable* for the simulation of the quenching process of a compound casting. Instead, thermal contact conductance must be taken as a function of contact pressure and gap width and a fully coupled analysis must be performed.

In the present example, results very similar to those for variable thermal contact conductance are obtained if the thermal contact conductance is assumed to be infinity (zero thermal contact resistance). This is, however, not a general rule. More realistic problems (more complex geometry and boundary conditions) often exhibit areas of low contact pressure (see Chapter 7). It is even possible that gaps open up during the quenching process (see Chapter 6).

3.8 Summary and Concluding Remarks

In this chapter the dependence of the thermal contact conductance on contact pressure and gap opening at the steel-aluminum interface of a compound casting has been discussed. Conduction through actual contact spots and heat transfer through the interstitial gas mainly contribute to the heat transfer through the interface. The contact conductance increases with increasing contact pressure and decreases with increasing gap opening.

In general, a variable thermal contact conductance must be accounted for when simulating the quenching process of a compound casting without metallurgical bonding. As a consequence, a fully coupled analysis is required.

Enhancements and Uncertainties

In order to simplify the model, the dependence of several parameters on temperature in the equations describing the thermal contact conductance has been ignored. It is straight forward to enhance the model by including these dependencies.

There is a certain degree of uncertainty regarding the pressure of the interstitial gas. If, for instance, a macroscopic gap opens up during the quenching of a compound casting, and this gap is connected to an ambient fluid (see for example Figure 6.6 on page 100), the gas pressure in the gap is known. If, on the other hand, such a macroscopic gap opens up without being connected to the surroundings, the magnitude of the gas pressure in the gap is not so obvious. Fortunately, the thermal conductivity of the interstitial gas appearing in Equations (3.13) and (3.14) is only weakly related to gas

pressure [VDI, 2002]. For very low gas pressures the temperature jump distances have to be accounted for - see Section 3.3.2.

Application to the Metal-Mold Interface

The approach presented in this chapter was prepared with the interface between the two materials of a compound casting in mind. Of course, it can basically also be applied to the metal-mold interface when simulating a casting process (solidification simulation). At these interfaces the thermal contact conductance usually decreases after the onset of solidification as a gap forms due to the thermal contraction of the casting and the thermal expansion of the mold [Santos et al., 2001].

However, fully coupled, three-dimensional numerical models of this kind comprising the casting, the mold and possibly even parts of the structure surrounding the mold are still computationally very expensive.

Chapter 4

A Ductile Failure Damage Indicator

4.1 Introduction

In chapters 6 and 7 of this dissertation a ductile failure damage indicator is used to predict the onset of fracture during the mechanical testing of steel-aluminum compound castings. Therefore, this chapter presents a very short introduction to ductile failure damage indicators. It is by no means meant as a full treatment of the comprehensive subject of damage mechanics. For an extensive introduction the reader is referred to the book by Lemaitre and Desmorat [2005].

Ductile failure in metals occurs through the generation, growth and coalescence of voids during plastic deformation. The generation of voids is often associated with the fracture or the debonding from small particles.⁽¹⁾ After a stage of growth, the coalescing voids form macrocracks, which eventually lead to final failure.

A number of methods have been developed to predict ductile failure. They can be grouped generally into coupled and uncoupled methods. The former take into account the change of the constitutive behavior of the material due to the progression of damage, whereas the latter ignore this change. Uncoupled methods are also referred to as *damage indicators*. A comparison of the coupled and the uncoupled approach can be found in the book by Lemaitre and Desmorat [2005].

In general, damage indicators can be implemented more easily into existing finite element programs than coupled methods. As damage indicators do not influence the finite element analysis itself, the calculation of a damage indicator can be implemented as a pure postprocessing procedure.

A number of different damage indicators have been suggested in the literature. Often, they are of the form:

$$D = \int_0^{\varepsilon_{\text{eqp},f}} f(\sigma_{ij}) d\varepsilon_{\text{eqp}} , \quad (4.1)$$

⁽¹⁾In the case of Al-Si-Mg casting alloys, void generation is often associated with the cracking of eutectic silicon particles [Polmear, 2006].

where σ_{ij} is the stress tensor, ε_{eqp} is the accumulated equivalent plastic strain and $\varepsilon_{\text{eqp},f}$ is the accumulated equivalent plastic strain at failure. When the damage indicator D reaches a critical value, the onset of fracture is predicted.

4.2 Damage Indicator Used in this Study

In the present work a damage indicator based on the work of Rice and Tracey [1969] and Hancock and Mackenzie [1976] is used. (Rice and Tracey investigated the enlargement of spherical voids in a triaxial stress field assuming a rigid-ideal plastic material.) Based on the findings of these authors, a reference failure strain for the triaxial case ε_f can be defined,

$$\varepsilon_f = \varepsilon_0 \exp\left(\frac{1}{2} - \frac{3}{2} \frac{\sigma_m}{\sigma_{\text{eq}}}\right), \quad (4.2)$$

where ε_0 is the critical strain in uniaxial tension, σ_m is the mean stress⁽²⁾ and σ_{eq} is the equivalent (here: von Mises) stress. The quotient $\sigma_m/\sigma_{\text{eq}}$ is referred to as *stress triaxiality*. Figure 4.1 shows a plot of $\varepsilon_f/\varepsilon_0$ as described by Equation (4.2). In the case of uniaxial tension $\sigma_m/\sigma_{\text{eq}} = 1/3$ and thus $\varepsilon_f = \varepsilon_0$.

Using the reference failure strain ε_f , the increment of a damage indicator can be defined:

$$dD = \frac{d\varepsilon_{\text{eqp}}}{\varepsilon_f}, \quad (4.3)$$

and the following damage indicator D is obtained:

$$D = \frac{1}{\varepsilon_0} \int_0^{\varepsilon_{\text{eqp},f}} \exp\left(\frac{3}{2} \frac{\sigma_m}{\sigma_{\text{eq}}} - \frac{1}{2}\right) d\varepsilon_{\text{eqp}}. \quad (4.4)$$

Failure occurs, when D reaches the critical value $D = 1$.

⁽²⁾ $\sigma_m = \text{tr}(\sigma_{ij})/3$

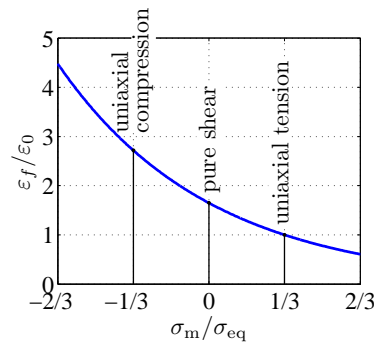


Figure 4.1: Reference failure strain ε_f as described by Equation (4.2).

Only one material parameter, the critical strain in uniaxial tension ε_0 , is needed for the calibration of Equation (4.4). Fischer et al. [1995] have explained in detail how ε_0 can be determined from the load-displacement curve and the neck diameter measured during a tensile test.

The finite element program ABAQUS⁽³⁾ has been used to carry out the simulations presented in this work. In order to evaluate Equation (4.4), a python program⁽⁴⁾ has been written that reads the simulation results from an ABAQUS output database, computes the damage indicator D at every integration point and writes D back to the database as a new “field output object” (see Dassault Systèmes [2008b]). After the execution of the program, D is available for postprocessing and fringe plots of D can be used to determine to location of the onset of fracture and the corresponding load. For examples of such fringe plots see Figure 7.13 and 7.14 on pages 115 and 116.

4.3 Discussion

It must be noted that the theoretical foundation of Equation (4.2) (the enlargement of spherical voids in a rigid-ideal plastic material investigated by Rice and Tracey [1969]) holds only for sufficiently high positive stress triaxialities. Thus, for low stress triaxialities Equation (4.2) must be seen as an empirical relation (see also [Gänser et al., 2001]).

Mohr and Henn [2007] used an interesting hybrid experimental-numerical method to investigate the onset of fracture in the same aluminum casting alloy used in present work (Al-7Si-Mg). The dependence of the failure strain on the stress triaxiality reported by the authors (see Mohr and Henn [2007, Fig. 17]) is very similar to the dependence described by Equation (4.2) and shown in Figure 4.1.

⁽³⁾<http://www.simulia.com>

⁽⁴⁾<http://www.python.org>

Chapter 5

Stress Singularities in Multi-Material Structures

5.1 Introduction

Local stress concentrations can occur due to the abrupt change in material properties at the interface of a multi-material structure. Under the assumptions of linear elasticity theory, these stress concentrations can manifest themselves as *stress singularities*. If such a stress singularity occurs, the computed stresses tend towards infinity when the singular point is approached.

In reality, of course, infinite stresses can not occur and the appearance of a stress singularity violates assumptions of linear elasticity theory. Even though the stresses predicted in these cases can not be interpreted directly, stress singularities correspond to strong stress concentrations in reality. Thus, the singular points will often be the origin of failure in the real structure.

The order of the stress singularity, which can be seen as a measure of the “severeness of the high stresses”, and the question whether a stress singularity occurs at all depend on a number of parameters. In this work, these parameter dependencies are considered in a systematical way and *design charts* are developed by which the order of the stress singularity can be directly registered. As the order of the stress singularity does not depend on the type of loading applied, these design charts are very general in application and some general statements about the proper geometrical design of steel-aluminum interfaces can be made.

Stress singularities are a fairly well-explored area in linear elasticity. Many different configurations are known to give rise to stress singularities. An extensive review of the literature can for instance be found in [Sinclair, 2004a,b].

In this work, attention is focused on the three two-dimensional configurations shown in Figure 5.1 as they are likely to appear in parts produced by compound casting. The analysis is restricted to the combination of two homogeneous, isotropic materials, which is in general a well-justified assumption for the material combination steel-aluminum.

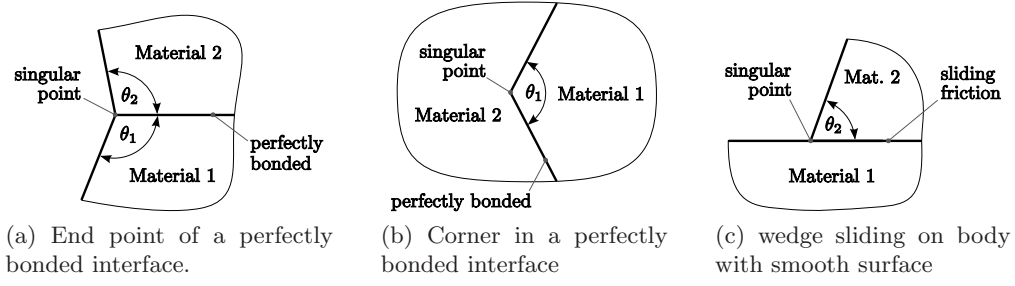


Figure 5.1: Configurations with possible stress singularities.

The first configuration considered is the end point of a perfectly bonded bimaterial interface. This is the point where the interface intersects the outer surface of the body as shown in Figure 5.1(a). The second configuration is a corner in a perfectly bonded bimaterial interface – see Figure 5.1(b). The third configuration is the case of a body with a sharp edge (a wedge) frictionally sliding on a body with a smooth surface as shown in Figure 5.1(c).

5.2 Mathematical Description

Using asymptotic analysis, an analytic expression can be derived that describes the singular stress field in the vicinity of the singular point. That means that the difference between the complete description of the stress field and the asymptotic expression vanishes when the singular point is approached.

Several methods have been proposed for performing the asymptotic analysis: The use of potentials together with separation of variables, introduction of complex variables or the use of the Mellin transform [Sinclair, 2004a,b]. All these methods are mathematically demanding and the details of the mathematical analyses are not shown here.

The stress field in the vicinity of the singular point can often be described in the following form:

$$\sigma_{ij}(r, \theta) = \sum_{k=1}^N \frac{K_k}{(r/L)^{\omega_k}} F_{ijk}(\theta) \quad 0 < \omega_k < 1 \quad (5.1)$$

where r and θ are the radial and the angular coordinate of a polar coordinate system whose origin is located at the singular point (see Figure 5.4). L is a characteristic length of the structure. Each ω_k is referred to as order of the singularity or *singularity exponent*. K_k is denoted as stress intensity factor⁽¹⁾. The function $F_{ijk}(\theta)$ only depends on θ and may be discontinuous at the interface.

⁽¹⁾This definition of the stress intensity factor K_k is different from the one used in fracture mechanics. K_k has the unit of stress.

It is assumed that the ω_k values are in descending order ($\text{Re}(\omega_1) > \text{Re}(\omega_2) > \dots > \text{Re}(\omega_N)$). Then, the sum on the right hand side of Equation (5.1) is dominated by the first term when r approaches zero. Often all but the first term are neglected and Equation (5.1) reads:

$$\sigma_{ij}(r, \theta) = \frac{K_1}{(r/L)^{\omega_1}} F_{ij1}(\theta) \quad 0 < \omega_1 < 1. \quad (5.2)$$

While this simplification is often justified, it should not be applied in certain special cases as will be demonstrated in Section 5.6.

According to the above definitions the stress field is singular for ω_1 positive and the larger ω_1 “the more singular it is”. As will be explained in Section 5.8.1, stress singularities with $\omega_1 \geq 1.0$ are not physically significant.

The asymptotic analysis, based on stress equilibrium equations, compatibility equations, Hooke’s law, interface conditions, and boundary conditions, usually leads to a homogeneous system of linear equations which has nontrivial solutions only if the determinant of the matrix of coefficients \mathcal{D} vanishes. This leads to the eigenvalue equation:

$$\mathcal{D}(p) = 0, \quad (5.3)$$

where p is – for the sake of generality – a complex variable. If the equation has no root in $0 < \text{Re}(p) < 1$, the stress field is regular. If it has one or more roots p_k in $0 < \text{Re}(p) < 1$, the stress field is singular and the N singularity exponents are $\omega_k = 1 - p_k$. Obviously, (5.3) could also be written in terms of $\omega = 1 - p$. However, (5.3) is the usual notation found in the literature.

For the case of an end point of a perfectly bonded interface Equation (5.3) takes the form:

$$\mathcal{D}(\theta_1, \theta_2, \alpha, \beta, p) = 0, \quad (5.3a)$$

where θ_1 and θ_2 are the angles describing the local geometry (see Figure 5.1(a)) and α and β are the so-called *Dundurs parameters* characterizing the material combination. The four elastic constants of the two materials enter Equation (5.3a) only through the two Dundurs parameters α and β – as will be explained in detail in Section 5.3.

For the case of a corner in a perfectly bonded interface (Figure 5.1(b)) Equation (5.3) takes the simpler form:

$$\mathcal{D}(\theta_1, \alpha, \beta, p) = 0, \quad (5.3b)$$

as $\theta_2 = 360^\circ - \theta_1$ in this case.

For the case of a wedge frictionally sliding on a body with smooth surface (Figure 5.1(c)) Equation (5.3) takes the form:

$$\mathcal{D}(\theta_2, \mu, \alpha, \beta, p) = 0, \quad (5.3c)$$

where μ is the coefficient of friction.

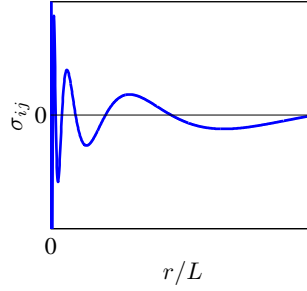


Figure 5.2: Oscillating stress singularity; schematic representation of Eqn. (5.4a) for constant θ . See, however, remarks in Section 5.5.4.

Complex eigenvalues

Equation (5.3) can have real as well as complex roots p_k . The mathematical description of the singular stress field outlined above basically stays valid when ω_k is complex. The real and the imaginary part of Equations (5.1) or (5.2) are then both possible descriptions of the singular stress field.

Assuming that the complex root $\omega_1 = \zeta_1 + i\eta_1$ is the root with the biggest real part, Eqn. (5.2) yields:

$$\sigma_{ij}(r, \theta) = \frac{K_1}{(r/L)^{\zeta_1}} \sin(\eta_1 \ln(r/L)) F_{ij1}(\theta) \quad \text{or} \quad (5.4a)$$

$$\sigma_{ij}(r, \theta) = \frac{K_1}{(r/L)^{\zeta_1}} \cos(\eta_1 \ln(r/L)) F_{ij1}(\theta) . \quad (5.4b)$$

This is the *oscillating stress singularity* known to occur at interface cracks. The oscillation is caused by the trigonometric function in (5.4a) and (5.4b) and becomes faster and faster as r approaches zero, because the argument of the trigonometric function goes to infinity. Figure 5.2 shows a schematic representation of Eqn. (5.4a) for constant θ . See, however, remarks in Section 5.5.4.

5.3 Dundurs Parameters

The material behavior of the two linear elastic isotropic materials considered here is described by four elastic constants. Dundurs [1969] has shown that for problems like the ones investigated here, the stress field shows a reduced dependence on the elastic constants. The solution only depends on the four elastic constants through the two

dimensionless Dundurs parameters:

$$\alpha = \frac{(G_2/G_1)(\kappa_1 + 1) - (\kappa_2 + 1)}{(G_2/G_1)(\kappa_1 + 1) + (\kappa_2 + 1)} \quad (5.5)$$

$$\beta = \frac{(G_2/G_1)(\kappa_1 - 1) - (\kappa_2 - 1)}{(G_2/G_1)(\kappa_1 + 1) + (\kappa_2 + 1)} \quad (5.6)$$

where

$$\kappa_i = 3 - 4\nu_i \quad \text{for plane strain,} \quad (5.7)$$

$$\kappa_i = \frac{3 - \nu_i}{1 + \nu_i} \quad \text{for generalized plane stress.} \quad (5.8)$$

G_1 and G_2 denote the shear moduli and ν_1 and ν_2 denote Poisson's ratio of the two materials.

At least for the cases with a perfectly bonded interface the physical significance of the generalized plane stress assumption (Equation (5.8)) is questionable [Durelli and Parks, 1972]. Even if the body under consideration is very thin, the mismatch of the mechanical properties will lead to significant out-of-plane stresses in the vicinity of the interface. Therefore, in this work, only the plane strain assumption (Equation (5.7)) is used.

Due to the physical limits $G_2/G_1 > 0$ and $0 < \nu_i < 0.5$, the possible values of α and β are restricted to a parallelogram in the α - β -plane as shown (for the assumption of plane strain) in Figure 5.3. The point $(\alpha, \beta) = (0, 0)$ corresponds to two identical materials. Also $\alpha \rightarrow 1$ for $G_2/G_1 \rightarrow \infty$ and $\alpha \rightarrow -1$ for $G_2/G_1 \rightarrow 0$. ν_1 nonlinearly varies along the right vertical line and ν_2 nonlinearly varies along the left vertical line as indicated in Figure 5.3. A choice of ν_1 and ν_2 defines a straight line across the parallelogram along which G_2/G_1 varies from 0 to ∞ . An example of such a line (for $\nu_1 = 0.2$ and $\nu_2 = 0.3$) is shown in the Figure.

This study focuses mainly on the material combination steel-aluminum. The corresponding material properties and the Dundurs parameters are given in Table 5.1. Exchanging the materials (material 1 becomes material 2 and vice versa) changes the Dundurs parameter α to $-\alpha$ and β to $-\beta$.

5.4 Design Charts

For the cases investigated here, the order of the singularity ω_1 depends on the Dundurs parameters (α, β) , the local geometry (θ_1, θ_2) and possibly on the coefficient of friction (μ) . Many authors choose a local geometry and possibly a coefficient of friction, search for the roots of Equation (5.3) and plot the singularity exponents as a function of α and β (see Bogy [1971]; Chen and Nisitani [1993]; Churchman et al. [2003]). The

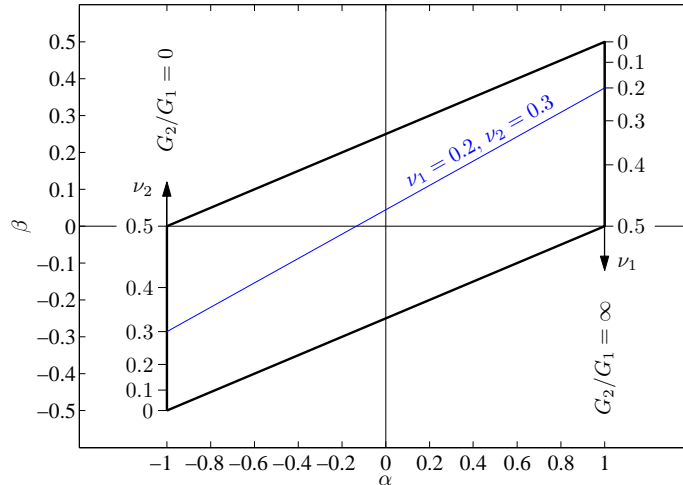


Figure 5.3: Admissible values of the Dundurs parameters α and β for plane strain.

Aluminum (Mat. 1)	Steel (Mat. 2)
$E_1 = 70$ GPa	$E_2 = 210$ GPa
$\nu_1 = 0.33$	$\nu_2 = 0.29$
$G_1 = 26.316$ GPa	$G_2 = 81.395$ GPa
$\alpha = 0.4896, \beta = 0.1135$	

Table 5.1: Material combination steel-aluminum: Material properties and Dundurs Parameters for plane strain.

resulting diagrams illustrate how the order of the singularity depends on the material combination.

However, for the practical engineer the number of different materials (materials exhibiting different elastic properties) to choose from is usually very limited, whereas the local geometry can often easily be modified.

Therefore, the author believes that a diagram that exhibits the singularity exponent as a function of θ_1 and θ_2 (or θ_2 and μ) for a given material combination is a valuable tool. As these diagrams are meant to support the practical engineer when designing a compound casting or other multi-material structures, they are here denoted as *design charts*.

To set up these design charts a program was written in Mathematica⁽²⁾. Basically, the program iterates through all possible combinations of the angles θ_1 and θ_2 (or θ_2

⁽²⁾<http://www.wolfram.com>

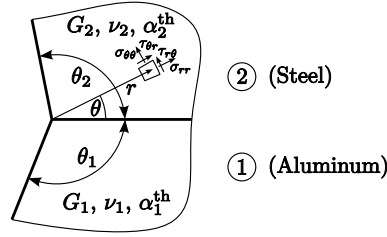


Figure 5.4: End point of a perfectly bonded interface.

and μ) and searches for the possibly complex roots of Equation (5.3) using Newton's method. A grid of values in the relevant part of the complex plane is used as starting values for Newton's method. This is necessary because Newton's method requires that the starting value is sufficiently close to the unknown root, and because (5.3) can have several roots in the relevant part of the complex plane. Generally, only ω_1 (the root with the largest real part) is reported in this work as it dominates the singular stress field (compare Equation (5.1)).

Additionally, the above mentioned program employs a special algorithm to compute the lines of transition from regular to singular behavior and the lines of transition from monotonic to oscillating singularities. The latter corresponds to the transition from real to complex roots of Equation (5.3).

In the following sections design charts are developed for the three configurations shown in Figure 5.1. At the end of each section examples are presented that demonstrate how these design charts can be used to identify configurations that give rise to singular stress fields and to modify the local geometry in order to avoid the singularity.

5.5 End Point of a Perfectly Bonded Interface

5.5.1 Introduction

The case of an end point of a perfectly bonded interface has been treated by Bogy [1968, 1970, 1971, 1975]. The configuration is shown in Figure 5.4.

The eigenvalue equation, taken from [Bogy, 1971], reads:

$$\mathcal{D}(\theta_1, \theta_2, \alpha, \beta, p) = A(\theta_1, \theta_2, p) \beta^2 + 2B(\theta_1, \theta_2, p) \alpha\beta + C(\theta_1, \theta_2, p) \alpha^2 - 2D(\theta_1, \theta_2, p) \beta - 2E(\theta_1, \theta_2, p) \alpha + F(\theta_1, \theta_2, p) = 0, \quad (5.9)$$

where

$$\begin{aligned}
 A(\theta_1, \theta_2, p) &= 4K(p, \theta_1) K(p, \theta_2) \\
 B(\theta_1, \theta_2, p) &= 2p^2 \sin^2(\theta_2)K(p, \theta_1) + 2p^2 \sin^2(\theta_1)K(p, \theta_2) \\
 C(\theta_1, \theta_2, p) &= 4p^2(p^2 - 1) \sin^2(\theta_1) \sin^2(\theta_2) + K(p, \theta_2 - \theta_1) \\
 D(\theta_1, \theta_2, p) &= 2p^2 (\sin^2(\theta_2) \sin^2(p\theta_1) - \sin^2(\theta_1) \sin^2(p\theta_2)) \\
 E(\theta_1, \theta_2, p) &= -D(\theta_1, \theta_2, p) + K(p, \theta_1) - K(p, \theta_2) \\
 F(\theta_1, \theta_2, p) &= K(p, \theta_1 + \theta_2) ,
 \end{aligned}$$

and the auxiliary function $K(p, x)$ is defined by

$$K(p, x) = \sin^2(px) - p^2 \sin^2(x).$$

For the special case of two identical materials ($\alpha = \beta = 0$), Equation (5.9) reduces to:

$$\sin^2(p\gamma) - p^2 \sin^2(\gamma) = 0 \quad \text{with} \quad \gamma = \theta_1 + \theta_2, \quad (5.10)$$

which is the eigenvalue equation for the well-known case of a reentrant corner in a homogeneous material as given by Williams [1952]. As the interface has “disappeared”, the equation only depends on $\gamma = \theta_1 + \theta_2$. Note also that (5.10) does not depend on the elastic properties of the material (α or β).

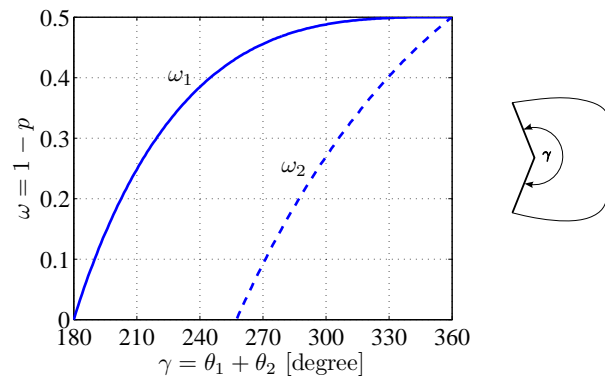
For the case of a reentrant corner in a homogeneous material Figure 5.5(a) shows the singularity exponents ω_1 and ω_2 as a function of $\gamma = \theta_1 + \theta_2$. Figure 5.5(b) shows only ω_1 as function of θ_1 and θ_2 . Figure 5.5(b) contains the same information as the ω_1 -curve in Figure 5.5(a). It is only provided for comparison with the following design charts.

As can be seen from Figure 5.5, the stress field is regular for $\gamma < 180^\circ$. As γ increases from 180° to 360° , the singularity exponent ω_1 increases from 0 to 0.5. For $\gamma = 360^\circ$ the classical crack-tip singularity is obtained.

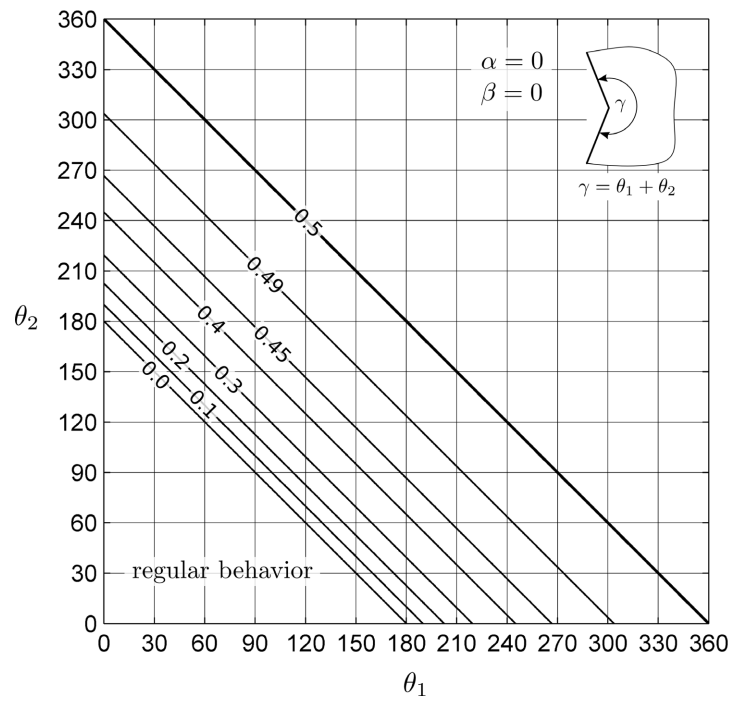
5.5.2 Design Chart

Figure 5.6 shows the design chart for the material combination steel-aluminum (material 1: aluminum, material 2: steel). While Figure 5.6(a) shows the real part of the singularity exponent ω_1 , Figure 5.6(b) shows the imaginary part. Values of the singularity exponent for selected combinations of θ_1 and θ_2 are also reported in Table 5.2.

The curve of transition from regular to singular behavior is denoted by “0.0” in Figure 5.6(a). The curve of transition from real to complex ω_1 (transition from monotonic to oscillating singularity) is an envelope of the curves for real ω_1 . The region of oscillating singularity is shaded gray.

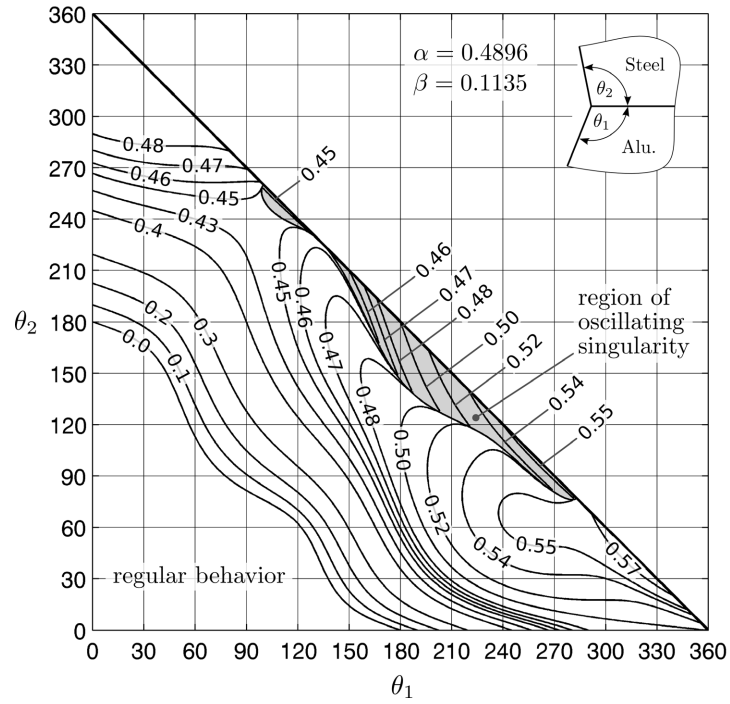


(a) Singularity exponents ω_1 and ω_2 as a function of $\gamma = \theta_1 + \theta_2$.

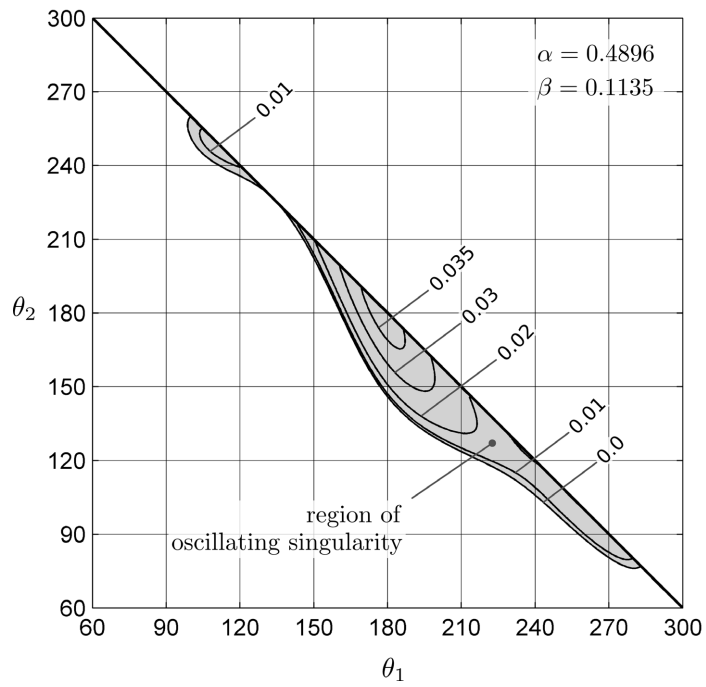


(b) Singularity exponent ω_1 as a function of θ_1 and θ_2 . Same information as ω_1 -curve in Figure 5.5(a).

Figure 5.5: Singularity exponents for a reentrant corner in a homogeneous material.



(a) Real part of the singularity exponent $\text{Re}(\omega_1)$.



(b) Imaginary part of the singularity exponent $\text{Im}(\omega_1)$.

Figure 5.6: Design chart for the end point of a perfectly bonded bimaterial interface; material combination: steel-aluminum.

θ_1	θ_2	$\omega_1 = 1 - p_1$
90°	90°	0.09156
45°	180°	0.20231
180°	45°	0.42874
90°	180°	0.40005
180°	90°	0.49378
135°	135°	0.44941
180°	180°	$0.5 + 0.036287i$

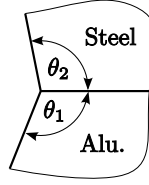


Table 5.2: Singularity exponent ω_1 for the end point of a perfectly bonded bimaterial interface; material combination: steel-aluminum ($\alpha = 0.4896$, $\beta = 0.1135$).

All configurations corresponding to a crack terminating at the interface lie on the straight line from $(0^\circ; 360^\circ)$ to $(360^\circ; 0^\circ)$. Complex singularity exponents are only found in the vicinity of that line. Thus, only configurations resembling cracks give rise to oscillating singularities for this material combination.

In Figure 5.6(b) it can be observed that the complex part of the singularity exponent rises from $\text{Im}(\omega_1) = 0.0$ at the line of transition from real to complex ω_1 to the maximum value $\text{Im}(\omega_1) = 0.036287$ at $\theta_1 = \theta_2 = 180^\circ$.

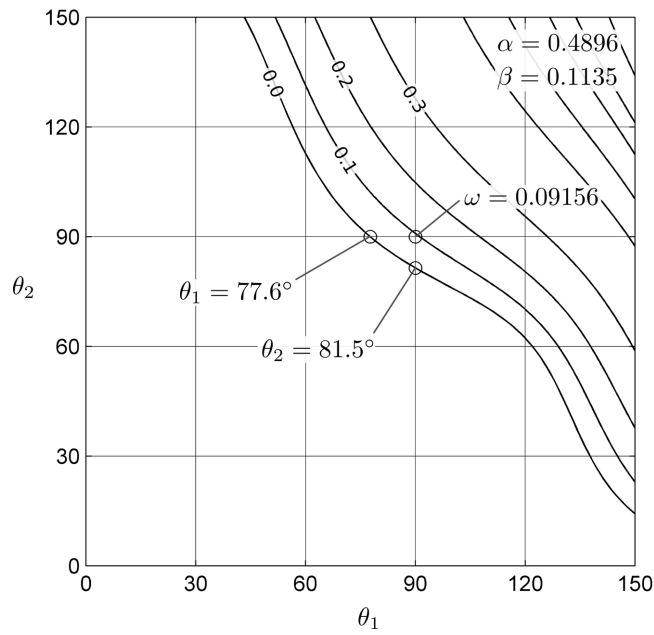
A conclusion that can be drawn from the design chart in Figure 5.6(a) is that if one of the angles, θ_1 or θ_2 , is kept at 180° the singularity can only be removed by decreasing the other angle to 0° , which is difficult to implement in practice.

Figure 5.7 shows details of the design chart in Figure 5.6(a) illustrating how to avoid singular behavior. For instance, the configuration $\theta_1 = \theta_2 = 90^\circ$ often found in practice yields singular behavior with singularity exponent $\omega_1 = 0.09156$. Starting from that configuration, either θ_1 can be decreased below 77.6° or θ_2 can be decreased below 81.5° to achieve regular behavior as shown in Figure 5.7(a). This leads to a sharp edge at the outer surface of the component which is sometimes undesirable.

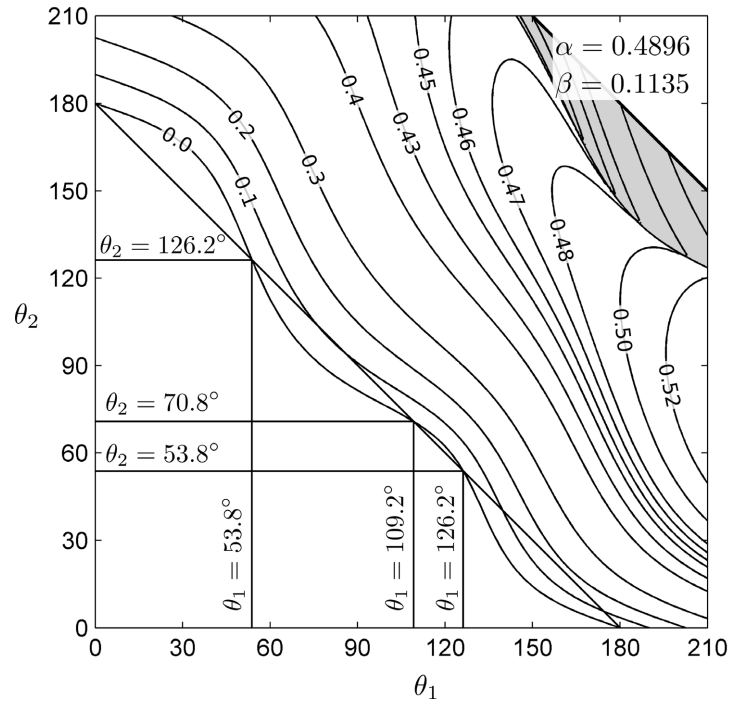
A smooth outer surface requires $\theta_1 + \theta_2 = 180^\circ$. All configurations fulfilling that requirement lie on the straight line from $(0^\circ; 180^\circ)$ to $(180^\circ; 0^\circ)$ shown in Figure 5.7(b). It can be observed that two angle windows allow for regular behavior. The first is $0^\circ < \theta_1 < 53.8^\circ$, the second is $109.2^\circ < \theta_1 < 126.2^\circ$.

Several examples demonstrating the beneficial effect of the above described geometrical modifications are presented in the following section.

A further design chart like the one in Figure 5.6 for a hypothetical material combination with $E_2/E_1 = 10$ is presented in Appendix C.



(a) Decreasing θ_1 or θ_2 .



(b) Regular behavior and smooth outer surface ($\theta_1 + \theta_2 = 180^\circ$)

Figure 5.7: Details of the design chart in Figure 5.6(a) illustrating how to avoid singular behavior.

Aluminum (Mat. 1)	Steel (Mat. 2)
$E_1 = 70 \text{ GPa}$	$E_2 = 210 \text{ GPa}$
$\nu_1 = 0.33$	$\nu_2 = 0.29$
$\alpha_1^{\text{th}} = 20.66 \cdot 10^{-6} \text{ K}^{-1}$	$\alpha_2^{\text{th}} = 11.7 \cdot 10^{-6} \text{ K}^{-1}$

Table 5.3: Material properties used for finite element analyses of the generic structures in Section 5.5.3.

5.5.3 Examples

In this section, a number of axisymmetric generic structures are investigated that demonstrate how the design charts (Figure 5.6) can be used to modify the local geometry of a structure in order to completely avoid the singularity. The analytical solutions represented by the design charts have been derived assuming plane strain conditions, not axisymmetry. However, with respect to the asymptotic singular character of the stress field, the analytical solutions obtained for plane strain conditions can also be assumed to be valid for the axisymmetric situation.

The generic axisymmetric structures are studied using standard linear finite element analysis. The material properties used are given in Table 5.3. All examples presented in this section have also been analyzed assuming plane strain instead of axisymmetry⁽³⁾. The results have been very similar to those presented in this section.

For problems involving stress singularities displacement-based finite element models (using non-singular elements) are capable of giving accurate results everywhere except in the region of a few elements surrounding the singular point [Whitcomb et al., 1982]. Therefore, this region was made extremely small compared to the size of the region of influence of the singularity using local mesh refinement as shown in Figure 5.8. The results coming from 6x6 elements in each quadrant surrounding the singular point have been ignored as also shown in Figure 5.8.

Two Structures Giving Rise to Singular Stress Fields (Examples A and B)

Figure 5.9 shows two axisymmetric generic structures giving rise to singular stress fields. Both structures represent cylindrical steel inserts perfectly bonded to an aluminum disc. The insert in example A (Figure 5.9(a) and (b)) is flush with the outer surface of the aluminum disc. The insert in example B (Figure 5.9(c) and (d)) protrudes above the outer surface of the aluminum disc. Two load cases are considered: in-plane tensile loading (referred to as load case 1) and a homogeneous temperature change of +100 K (referred to as load case 2).

⁽³⁾The axis of rotational symmetry is then the axis of mirror symmetry.

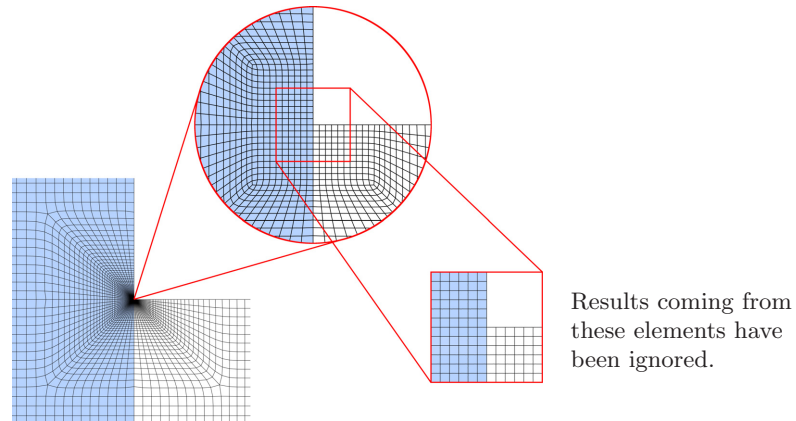


Figure 5.8: Local mesh refinement near the (upper right) singular point of the generic structure shown in Figure 5.9(c).

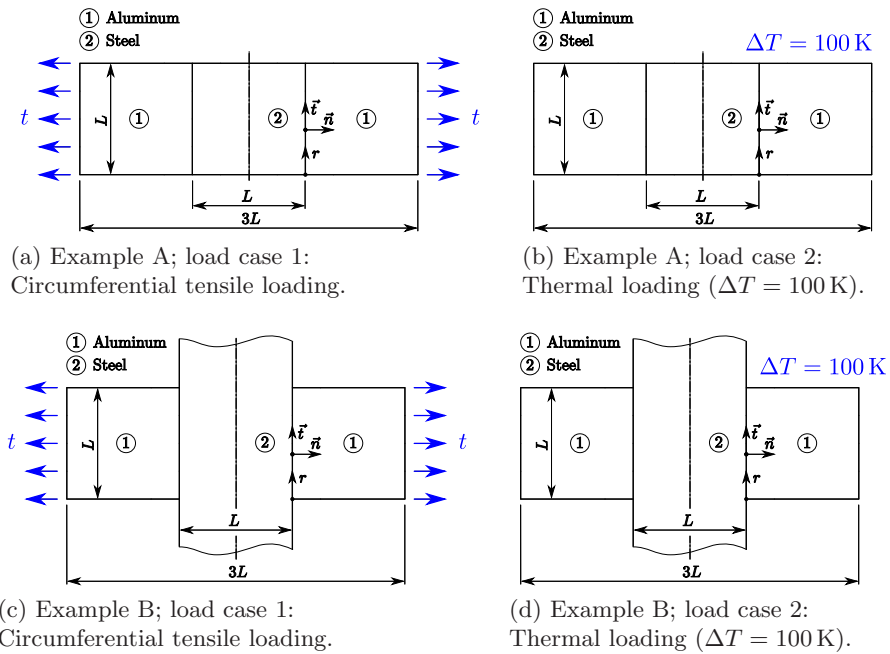


Figure 5.9: Two axisymmetric examples giving rise to singular stress fields; geometry and load cases.

From the design chart (Fig. 5.6) the singularity exponents are obtained as $\omega_1 = 0.09156$ for example A ($\theta_1 = 90^\circ$, $\theta_2 = 90^\circ$) and $\omega_1 = 0.40005$ for example B ($\theta_1 = 90^\circ$, $\theta_2 = 180^\circ$). Hence, the singularity in example B is more severe than the singularity in example A.

In Figure 5.10 plots of the normal and shear stresses along the interface are shown. For load case 1 (mechanical loading) the stresses are given in normalized form, that is the stress values are divided by the value of the applied surface load density t . Each plot of the stresses over the normalized distance along the interface is accompanied by a corresponding double logarithmic plot. Taking the logarithm of Equation (5.2) yields:

$$\log(\sigma_{ij}(r, \theta)) = \underbrace{\log(K_1 F_{ij1}(\theta))}_{\text{independent of } r} - \omega_1 \log(r/L). \quad (5.11)$$

Thus, for any constant angle θ ($\theta = 0$ along the interface) the plot of $\log(\sigma_{ij})$ versus $\log(r/L)$ should approach a straight line with slope $-\omega_1$ for $r/L \rightarrow 0$. This stays true when $\log(\sigma_{ij}/t)$ is plotted instead of $\log(\sigma_{ij})$. The double logarithmic plots in Figure 5.10 contain triangles representing the respective slopes. In all cases the slope of the curves is in good agreement with the predicted values for ω_1 .

It can also be observed how the larger singularity exponent of example B corresponds to a larger region of influence of the singularity – compare Figure 5.10(c) to Figure 5.10(d).

It is noteworthy that in the case of pure thermal loading (load case 2) the normal stress σ_{nn} close to the singular point is of opposite sign to the overall normal stress (see Figure 5.10(g) and (h)).

In the following six possibilities to completely avoid the stress singularity using local geometry modifications are studied for example A.

Example A1 and A2

Starting from the initial configuration $\theta_1 = \theta_2 = 90^\circ$ of example A either θ_1 can be decreased below 77.6° or θ_2 can be decreased below 81.5° in order to avoid the singularity (see Figure 5.7(a)).

By way of example, θ_1 is chosen as 57° (designated as example A1) or θ_2 is chosen as 57° (designated as example A2). Figure 5.11 shows the locally modified geometries as well as plots of the normal and shear stresses along the interface. The plots in Figure 5.11 should be compared to Figure 5.10(c) and (g).

In the case of mechanical loading (load case 1) both modifications (A1 and A2) reduce the normal and shear stress in the region of the previously singular point to a very low level! In the case of thermal loading (load case 2) the normal and shear stress at the previously singular point are reduced to a larger extent by modification A2. Thus,

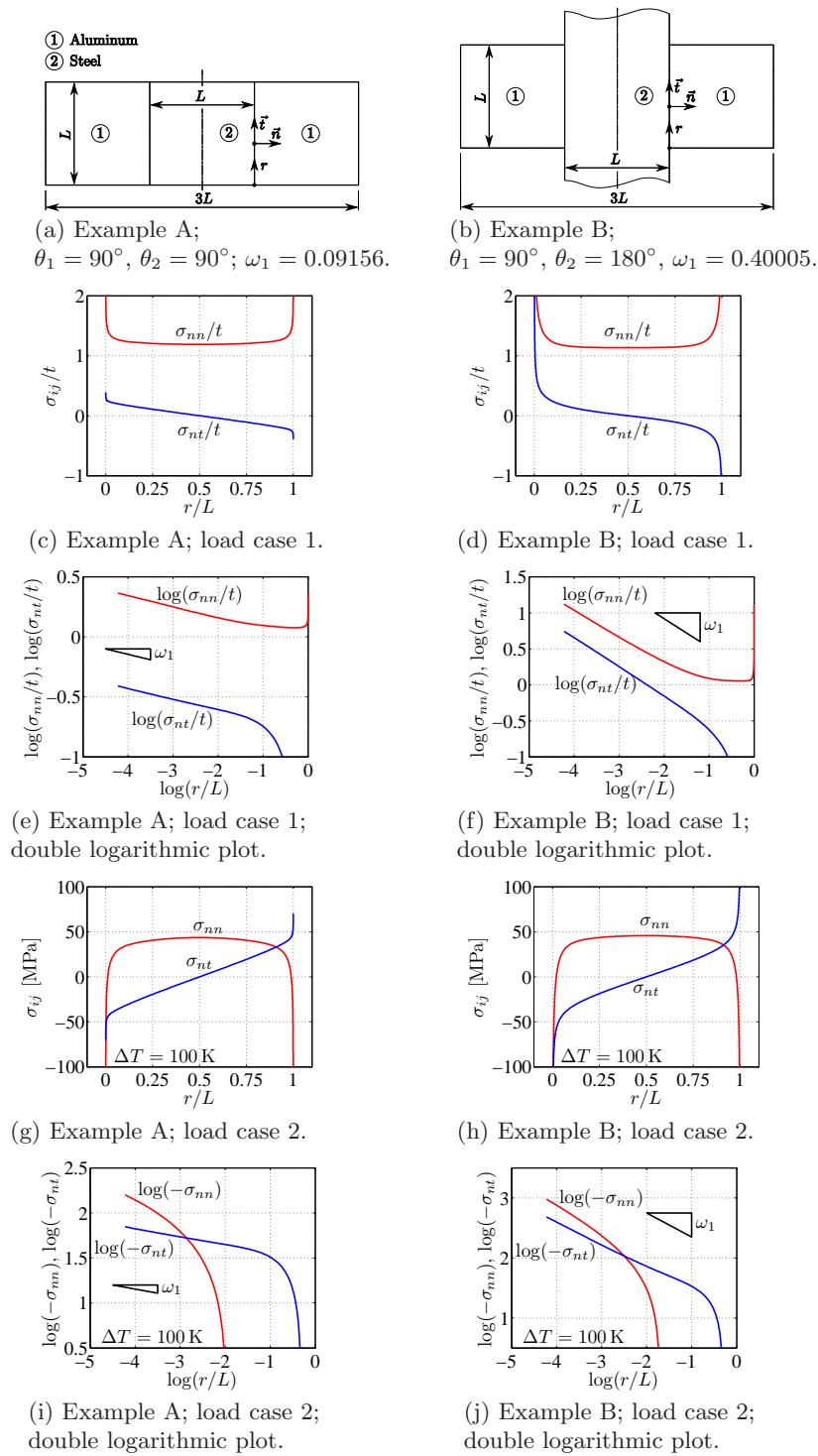


Figure 5.10: Two axisymmetric examples giving rise to singular stress fields; diagrams show normal stress σ_{nn} and shear stress σ_{nt} at the interface.

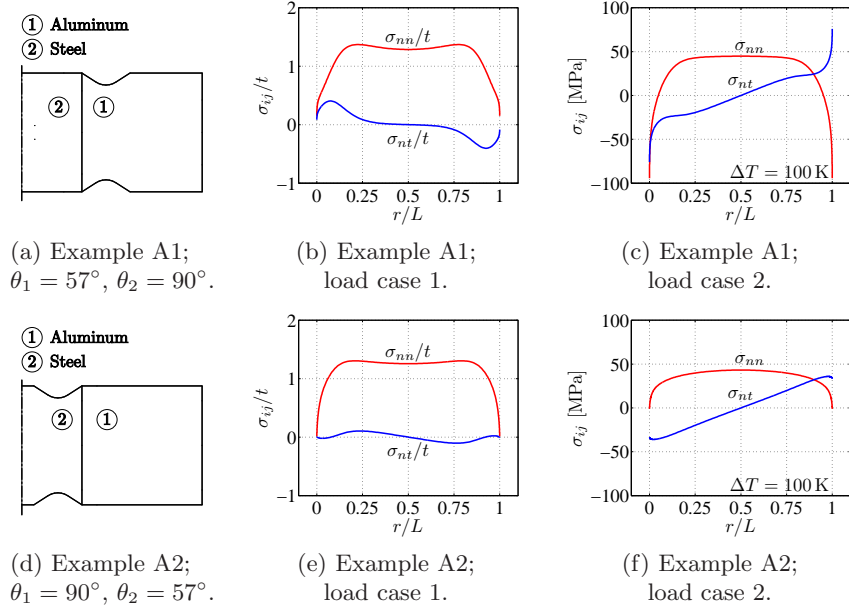


Figure 5.11: Removing the singularity from example A by either decreasing θ_1 or decreasing θ_2 ; only half of the meridian section is shown.

in the case of thermal loading, decreasing the angle of the stiffer of the two materials (material 2 is steel) seems to be the better choice.

Example A3 and A4

A smooth outer surface requires $\theta_1 + \theta_2 = 180^\circ$. As explained in the previous section, two angle windows fulfilling that requirement allow for regular behavior: $0^\circ < \theta_1 < 53.8^\circ$ or $109.2^\circ < \theta_1 < 126.2^\circ$ – see Figure 5.7(b).

By way of example, θ_1 is chosen as 45° (designated as example A3) or θ_1 is chosen as 111° (designated as example A4). Figure 5.12 shows the locally modified geometries as well as plots of the normal and shear stresses along the interface. As the interface is not flat, “ n ” refers to the local normal direction and “ t ” refers to the local tangential direction in Figure 5.12. Again these plots should be compared to Figure 5.10(c) and (g).

In the case of mechanical loading (load case 1) both modifications (A3 or A4) markedly reduce the normal and shear stress in the region of the previously singular point. In the case of thermal loading (load case 2) the reduction of the normal and shear stress in the region of the previously singular point is more favorable for modification A4. Again, in the case of thermal loading, decreasing the angle of the stiffer of the two materials (material 2 is steel) seems to be the slightly better choice.

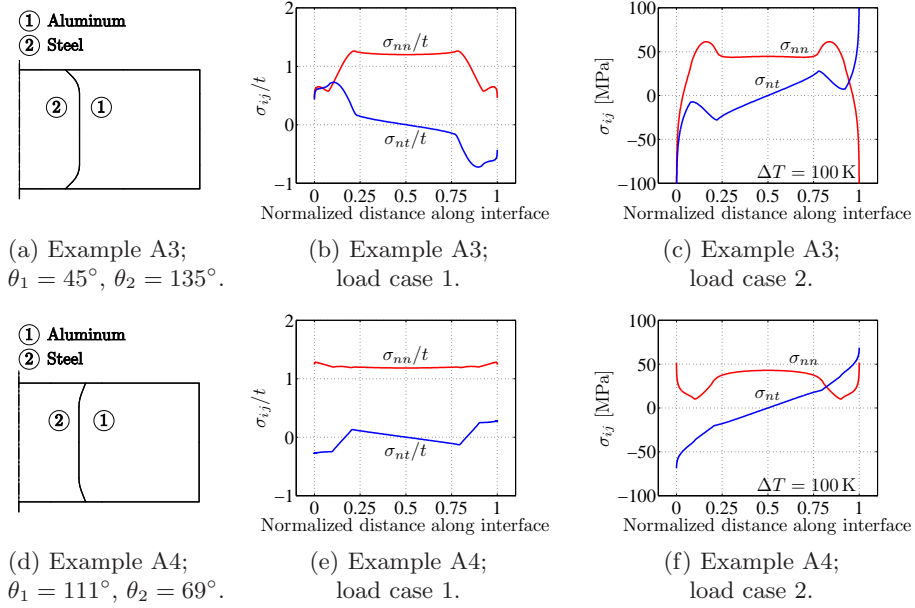


Figure 5.12: Removing the singularity from example A fulfilling $\theta_1 + \theta_2 = 180^\circ$; only half of the meridian section is shown.

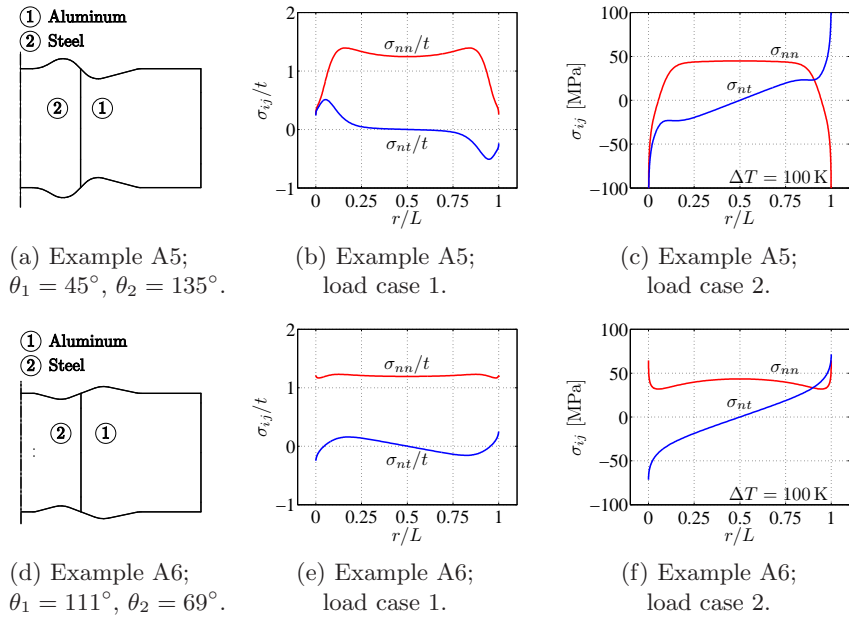


Figure 5.13: Alternative method for removing the singularity from example A fulfilling $\theta_1 + \theta_2 = 180^\circ$; only half of the meridian section is shown.

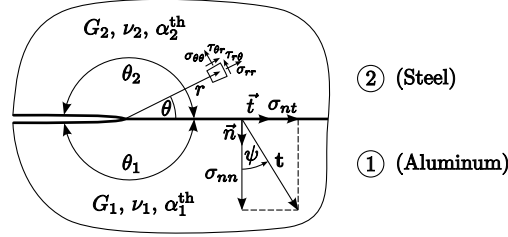


Figure 5.14: Crack lying in a bimaterial interface.

Example A5 and A6

In example A3 and A4 the singularity has been removed by locally inclining the interface in the meridian section, keeping the outer surface smooth ($\theta_1 + \theta_2 = 180^\circ$), see Figure 5.12. A similar modification (in terms of the angles θ_1 and θ_2) can also be achieved while keeping the interface flat, as shown in Figure 5.13. The plots of the normal and shear stress along the interface are similar to those of example A5 and A6 (compare Figure 5.12 to Figure 5.13).

While overall the geometry of examples A5 and A6 is more complicated than that of examples A3 and A4, keeping the interface flat might be beneficial in certain situations.

5.5.4 Some Remarks on Interface Cracks

In this section some remarks on interface cracks (cracks lying in the bimaterial interface) are made, and the stress state at the crack tip of a steel-aluminum interface crack is discussed by way of an example. This section is by no means meant as a full treatment of the subject of interface cracks. For an introduction to the wide topic the reader is referred to [O'Dowd, 2008] and [Rice, 1988].

By setting $\theta_1 = \theta_2 = 180^\circ$ (see Figure 5.14) Equation (5.9) reduces to the eigenvalue equation for the interface crack problem:

$$4 \sin^4(p\pi) \beta^2 + \sin^2(p2\pi) = 0, \quad (5.12)$$

which has the solution:

$$p_1 = \xi_1 + i\eta_1 = \frac{1}{2} + i \frac{1}{2\pi} \ln \left(\frac{1 + \beta}{1 - \beta} \right). \quad (5.13)$$

The singularity exponent $\omega_1 = 1 - p_1$ then is:

$$\omega_1 = \zeta_1 + i\eta_1 = \frac{1}{2} + i \frac{1}{2\pi} \ln \left(\frac{1 + \beta}{1 - \beta} \right). \quad (5.14)$$

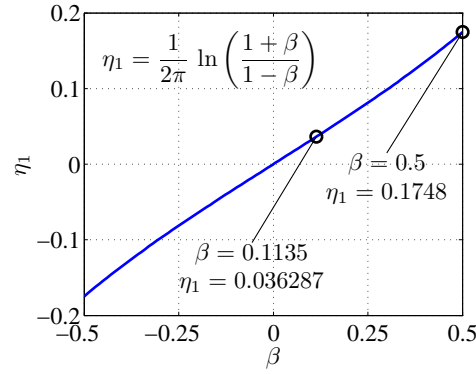


Figure 5.15: Bimaterial constant η_1 as a function of Dundurs parameter β , plotted over the admissible range $-0.5 \leq \beta \leq 0.5$.

Regarding interface cracks, the imaginary part of the singularity exponent $\eta_1 = \text{Im}(\omega_1)$ is often referred to as the *bimaterial constant*:

$$\eta_1 = \frac{1}{2\pi} \ln \left(\frac{1+\beta}{1-\beta} \right). \quad (5.15)$$

The bimaterial constant η_1 only depends on the second Dundurs Parameter β . Figure 5.15 shows η_1 as a function of β , plotted over the admissible range $-0.5 \leq \beta \leq 0.5$. As indicated in Table 5.2 on page 67, $\eta_1 = 0.036287$ for the material combination steel-aluminum. For the limiting case $\beta = 0.5$ (an extremely stiff material bonded to an extremely compliant material, see also Figure 5.3), η_1 assumes its maximum value $\eta_1 = 0.1748$.

Using a complex stress intensity factor

$$\hat{\mathbf{K}} = \hat{K}_1 + i\hat{K}_2 = |\hat{\mathbf{K}}| e^{i\varphi}, \quad (5.16)$$

the normal and shear stress directly ahead of the crack tip may be written:

$$(\sigma_{nn} + i\sigma_{nt})|_{\theta=0} = \frac{\hat{\mathbf{K}} r^{i\eta_1}}{\sqrt{2\pi r}} = \frac{|\hat{\mathbf{K}}| e^{i(\varphi + \eta_1 \ln r)}}{\sqrt{2\pi r}}, \quad (5.17)$$

or, using Euler's formula⁽⁴⁾,

$$\sigma_{nn}|_{\theta=0} = \frac{|\hat{\mathbf{K}}|}{\sqrt{2\pi r}} \cos(\underbrace{\varphi + \eta_1 \ln r}_{\psi}), \quad (5.18a)$$

$$\sigma_{nt}|_{\theta=0} = \frac{|\hat{\mathbf{K}}|}{\sqrt{2\pi r}} \sin(\underbrace{\varphi + \eta_1 \ln r}_{\psi}). \quad (5.18b)$$

⁽⁴⁾Euler's formula: $e^{i\varphi} = \cos(\varphi) + i \sin(\varphi)$

$$r_2/r_1 = \exp(\Delta\psi/\eta_1)$$

$\Delta\psi = \psi_2 - \psi_1$	steel-aluminum ⁽¹⁾	limiting case $\eta_1 = 0.1748$
10°	$1.23 \cdot 10^2$	2.71
45°	$2.51 \cdot 10^9$	$8.93 \cdot 10^1$
90°	$6.31 \cdot 10^{18}$	$7.97 \cdot 10^3$
180°	$3.98 \cdot 10^{37}$	$6.36 \cdot 10^7$

⁽¹⁾ $\eta_1 = 0.036287$

Table 5.4: Ratio r_2/r_1 for the material combination steel-aluminum and the limiting case $\eta_1 = 0.1748$.

From Equation (5.18a) and (5.18b) it can be seen that for *any* complex stress intensity factor $\hat{\mathbf{K}} = \hat{K}_1 + i\hat{K}_2 = |\hat{\mathbf{K}}| e^{i\varphi}$ normal *and* shear stresses occur at the interface. That is due to the oscillating singularity the stress fields are inherently mixed mode. Mode I and Mode II stress intensity factors equivalent to those for a crack in a homogeneous material cannot be defined. Thus, at least in the strict sense, \hat{K}_1 is not a Mode I stress intensity factor and \hat{K}_2 is not a Mode II stress intensity factor. For a further discussion see [Rice, 1988].

From Equation (5.17), (5.18a) and (5.18b) it can be seen that the angle ψ , defining the ratio of shear to normal traction at the interface (see Figure 5.14), is:

$$\psi = \varphi + \eta_1 \ln r . \quad (5.19)$$

ψ varies with distance from the crack tip and goes to infinity (“rotates faster and faster”) as $r \rightarrow 0$. As ψ is not defined at $r = 0$, the value of ψ at a fixed distance \hat{L} (independent of specimen size or crack length) is commonly used as a measure of the “mode mix” [O’Dowd, 2008].

From Equation (5.19) it is obvious that when r changes from r_1 to r_2 , the corresponding change in ψ is:

$$\Delta\psi = \psi_2 - \psi_1 = \eta_1 \ln(r_2/r_1) . \quad (5.20)$$

For example, for the material combination steel-aluminum $\Delta\psi = 4.79^\circ$ for $r_2/r_1 = 10$. For the limiting case $\eta_1 = 0.1748$, $\Delta\psi = 23.07^\circ$ for $r_2/r_1 = 10$.

Inversely, the ratio of two r values corresponding to a given change in ψ is:

$$r_2/r_1 = \exp(\Delta\psi/\eta_1) . \quad (5.21)$$

Table 5.4 lists the ratio r_2/r_1 for some values of $\Delta\psi$ for the material combination steel-aluminum and for the limiting case $\eta_1 = 0.1748$.

It must be noted that the range of physically significant values of r is limited. The largest physically significant value r_{\max} is given by the region of influence of the singularity. For typical engineering structures $r_{\max} \approx 10^{-2}$ m. The smallest physically significant value r_{\min} is in the order of a micron $r_{\min} \approx 10^{-6}$ m. That is, $r_{\max}/r_{\min} \approx 10^4$. Evaluating Equation (5.20) at $r_2/r_1 = 10^4$ yields $\Delta\psi_{\max} \approx 19^\circ$ for the material combination steel-aluminum and $\Delta\psi_{\max} \approx 92^\circ$ for the limiting case $\eta_1 = 0.1748$. It must be concluded that a change in ψ larger than 92° is impossible within a physically significant range of r values.

Obviously, the schematic representation of the oscillating stress singularity in Figure 5.2 (page 60) is somewhat misleading. Between two adjacent zeros r_1 and r_2 of the function depicted in Figure 5.2 the angle ψ changes by 180° – see Equations (5.18a) and (5.18b). From Equation (5.21) follows that then $r_2/r_1 = 3.98 \cdot 10^{37}$ for the material combination steel-aluminum and $r_2/r_1 = 6.36 \cdot 10^7$ for the limiting case $\eta_1 = 0.1748$. The illustration in Figure 5.2 implies $r_2/r_1 \approx 2$. It follows that (even for a combination of two very different materials) it is impossible to have two zeros of the stress components within a physically significant range of values of r .

For example, the stress state at the interface of an axisymmetric generic structure, designated as example B, is investigated using linear finite element analysis. The example is derived from example A (see Figure 5.10, page 72) by introducing a crack in the middle of the bimaterial interface as shown in Figure 5.16(a). Only one load case, namely in-plane tensile loading, is considered.

In Figure 5.16(b) a plot of the normal and shear stresses along the interface is shown. The stresses are given in normalized form. That is, the stress values are divided by the value of the applied surface load density t . Four singular points can be observed: Two points where the interface intersects the outer surface of the body ($\hat{r}/L = 0$ and $\hat{r}/L = 1$) and two crack tips ($\hat{r}/L = 0.45$ and $\hat{r}/L = 0.55$).

From Figure 5.16(c) it can be seen that the angle ψ assumes a finite value where the interface intersects the outer surface of the body (monotonic singularities). In contrast, as expected from Equation (5.19), ψ goes to plus or minus infinity when one of the crack tips is approached.

Figure 5.16(d) show a plot of ψ versus $\log(r/L)$ for the upper crack tip. As can be seen from Equation (5.19) the plot should approach a straight line with slope $\eta_1/\log(e)$ ⁽⁵⁾ for $r \rightarrow 0$. The plot in Figure 5.16(d) contain a triangle representing this slope. The slope of the curves is in good agreement with the predicted value for $\log(r/L) < -2$.

⁽⁵⁾Substitute $\ln(r) = \log(r)/\log(e)$ in Equation (5.19)

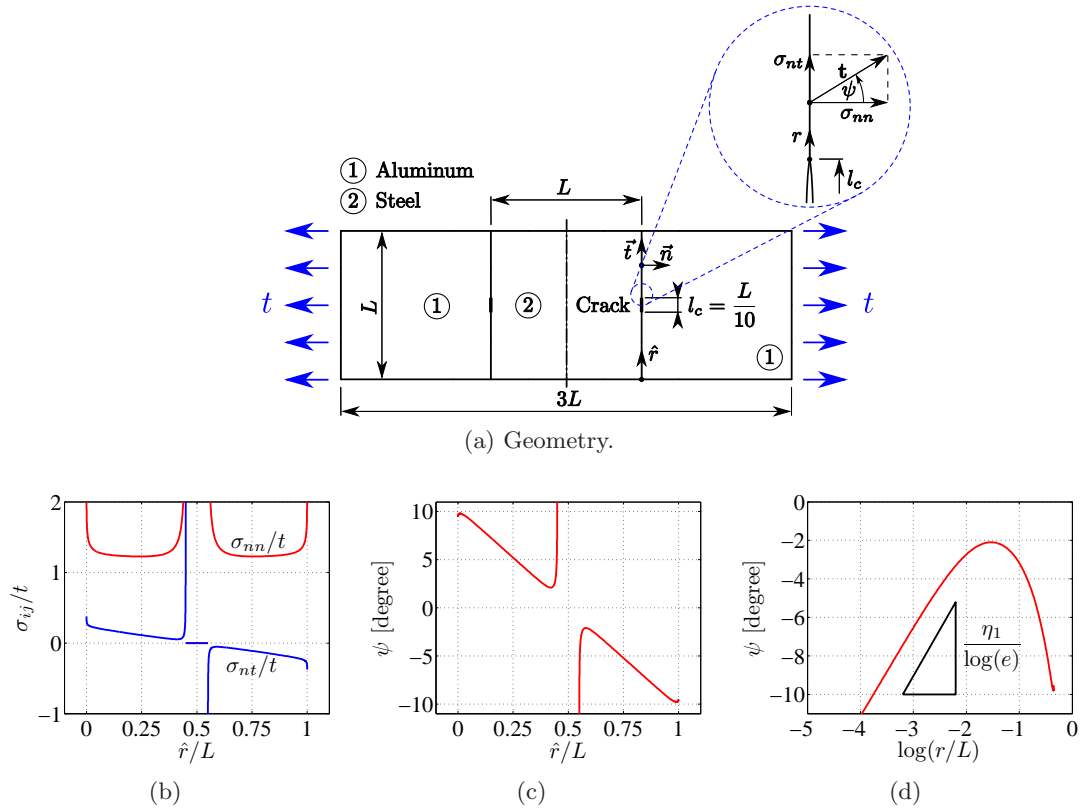


Figure 5.16: Example B: Axisymmetric generic structure with axisymmetric crack lying in the bimaterial interface.

5.6 Corner in a Perfectly Bonded Interface

5.6.1 Introduction

The case of two isotropic dissimilar wedge regions which are connected along both of their common faces (see Fig. 5.17, left) – the case of an interface corner – has been treated by Bogy and Wang [1971] and later been reinvestigated by Chen and Nisitani [1993]. Both investigations arrive at the same eigen equation for the determination of the order of the singularity. Chen and Nisitani, however, were able to split the eigen

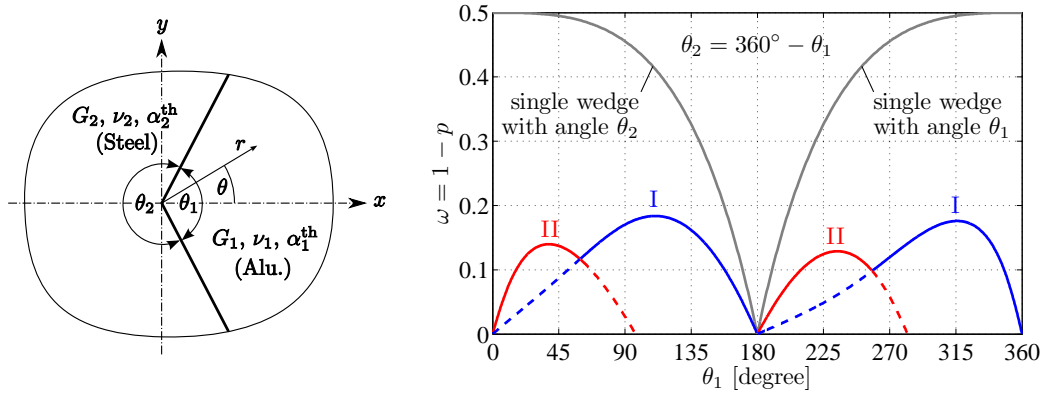


Figure 5.17: Design chart for a corner in a perfectly bonded interface; material combination: steel-aluminum ($\alpha = 0.4896$, $\beta = 0.1135$).

equation into two parts:

$$\mathcal{D}(\theta_1, \alpha, \beta, p) = \mathcal{D}_1(\theta_1, \alpha, \beta, p)\mathcal{D}_2(\theta_1, \alpha, \beta, p) = 0, \quad (5.22)$$

$$\begin{aligned} \mathcal{D}_1(\theta_1, \alpha, \beta, p) = & (\alpha - \beta)^2 p^2 (1 - \cos(2\theta_1)) + \\ & -2p(\alpha - \beta) \sin(\theta_1) [\sin(p\theta_1) + \sin(p(2\pi - \theta_1))] + \\ & -2p(\alpha - \beta)\beta \sin(\theta_1) [\sin(p(2\pi - \theta_1)) - \sin(p\theta_1)] + \\ & +(1 - \alpha^2) - (1 - \beta^2) \cos(2p\pi) + \\ & +(\alpha^2 - \beta^2) \cos(2p(\theta_1 - \pi)), \end{aligned} \quad (5.23)$$

$$\begin{aligned} \mathcal{D}_2(\theta_1, \alpha, \beta, p) = & (\alpha - \beta)^2 p^2 (1 - \cos(2\theta_1)) + \\ & +2p(\alpha - \beta) \sin(\theta_1) [\sin(p\theta_1) + \sin(p(2\pi - \theta_1))] + \\ & +2p(\alpha - \beta)\beta \sin(\theta_1) [\sin(p(2\pi - \theta_1)) - \sin(p\theta_1)] + \\ & +(1 - \alpha^2) - (1 - \beta^2) \cos(2p\pi) + \\ & +(\alpha^2 - \beta^2) \cos(2p(\theta_1 - \pi)), \end{aligned} \quad (5.24)$$

and showed that the first part \mathcal{D}_1 corresponds to the singularity appearing for a pure mode I deformation and the second part \mathcal{D}_2 corresponds to the singularity appearing for a pure mode II deformation. Mode I here refers to a deformation that is symmetric about $\theta = 0$ and Mode II refers to a deformation that is antisymmetric about $\theta = 0$. In the case of symmetry u_r is an even function of θ about $\theta = 0$, u_θ an odd, in the case of antisymmetry, vice versa.

5.6.2 Design Chart

Figure 5.17 (right) shows the design chart for the material combination steel-aluminum. The situation here is considerably simpler than in the previous section as the local

geometry is described by one angle (θ_1) only.

Curves corresponding to the roots of Equation (5.23) (Mode I deformation) and curves corresponding to the roots of Equation (5.24) (Mode II deformation) are labeled “I” and “II”, respectively. As we require that the singularity exponents ω_k (see Equation (5.1), page 58) are in descending order ($\omega_1 > \omega_2 > \dots > \omega_N$), the solid parts of the curves correspond to ω_1 and the dashed parts of the curves correspond to ω_2 .

Complex roots of Equation (5.22) exist but do not occur for the material combination steel-aluminum for any angle θ_1 .

For comparison the singularity exponents for a reentrant corner in a homogeneous material (“a single wedge”) with angles θ_1 or θ_2 are also shown in Figure 5.17 – compare Figure 5.5(a) on page 65. It can be concluded that (for a general loading situation) the singularity appearing at the corner of a steel-aluminum interface is always considerably weaker than that of a corresponding reentrant corner in a homogeneous material.

For a general loading situation regular behavior is only obtained for the two limiting cases $\theta_1 = 0^\circ$ and $\theta_1 = 360^\circ$ and for a straight (or smooth) interface ($\theta_1 = 180^\circ$). In the case of pure Mode II loading two angle windows allow for regular behavior: $97^\circ < \theta_1 < 180^\circ$ and $282^\circ < \theta_1 < 360^\circ$.

In many situations an obvious possibility to eliminate the stress singularity is to replace the sharp corner in the bimaterial interface with a smooth curve.

5.6.3 Example

For example, the stress state at the interface of an generic structure, designated as example C, is studied using linear finite element analysis. The geometry of the example, a rhombic steel insert perfectly bonded to a square aluminum block, is shown in Figure 5.18(a). Plane strain conditions and in plane tensile loading are assumed.

Attention is focused on the singular point at the right corner of the rhombic insert, where $\theta_1 = 225^\circ$. As can be seen from the design chart in Figure 5.18(b), the corresponding singularity exponents are: $\omega_1 = 0.1244$ and $\omega_2 = 0.04862$.

Figure 5.18(c) shows a plot of the normal stress along the interface and Figure 5.18(d) shows the corresponding double logarithmic plot. For $r/l_{\text{int}} \rightarrow 0$ the double logarithmic plot approaches a straight line with slope $-\omega_2$, not $-\omega_1$. That is, the smaller singularity exponent ω_2 , not ω_1 , determines the stress state in the vicinity of the singular point as the loading is purely mode I.

In other words, Equation (5.1) still properly describes the stress field in the vicinity of the singular point. However, due to the pure Mode I loading, $K_1 = 0$ and the

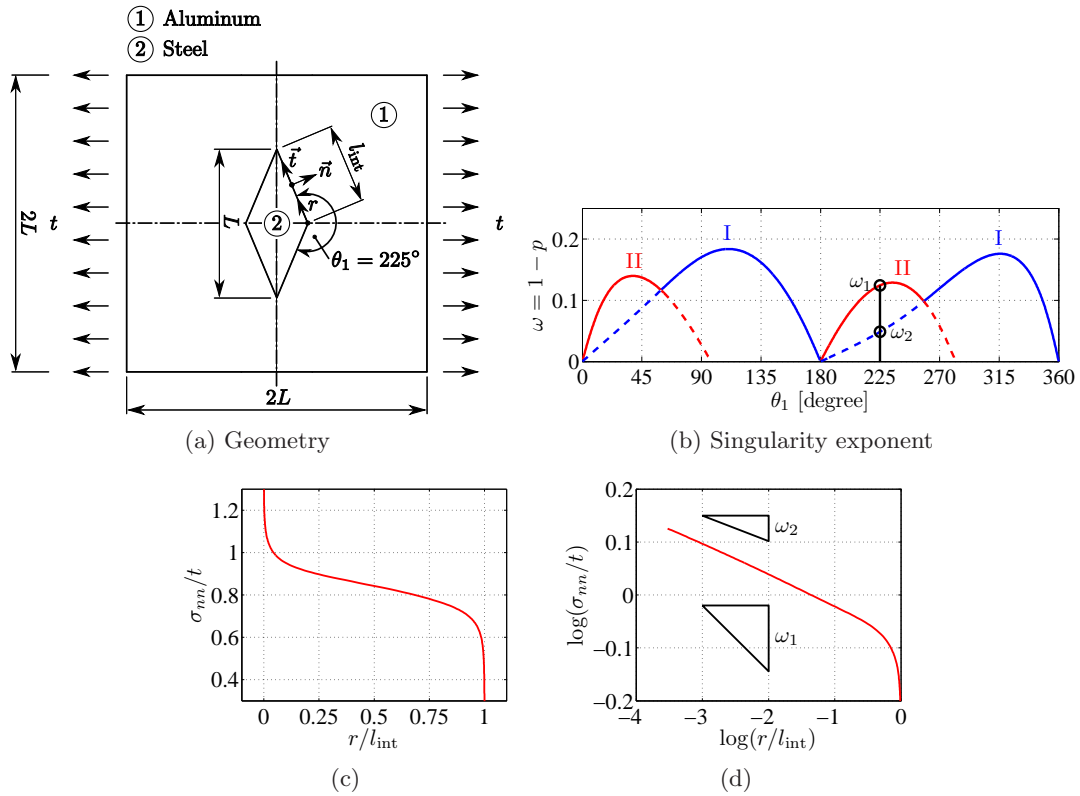


Figure 5.18: Example C: Corner in a perfectly bonded bimaterial interface.

asymptotic stress field is given by:

$$\sigma_{ij}(r, \theta) = \frac{K_2}{(r/L)^{\omega_2}} F_{ij2}(\theta) . \quad (5.25)$$

5.7 Wedge Frictionally Sliding on a Body with Smooth Surface

5.7.1 Introduction

The case of a wedge in frictionless contact with a body with smooth surface has been treated by Dundurs and Lee [1972]. The case of a wedge frictionally sliding on a body with smooth surface, as shown in Figure 5.19, has been treated by Comninou [1976] and Churchman et al. [2003] assuming Coulomb's law of sliding friction at the interface. The potentially singular point is located at $r = 0$.

This situation arises whenever two bodies in contact are in relative motion with respect to one another and one of the bodies has a sharp edge at the boundary of the contact

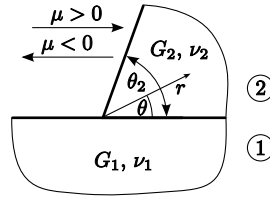


Figure 5.19: Wedge frictionally sliding on a body with smooth surface.

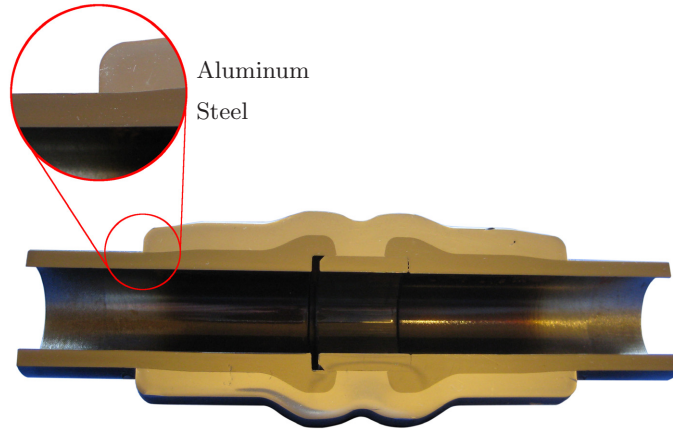


Figure 5.20: Compound casting with sharp edge at the boundary of the contact surface.

surface. It is important to note that local sliding motions can occur without global body motions. This may happen when a structure consisting of frictionally connected parts is loaded or unloaded. As an example for such a structure, Figure 5.20 shows a cut through an aluminum-steel compound casting without material-locking connection. The aluminum part has a sharp edge at the boundary of the contact surface.

Sliding friction in the region of interest, i.e., for small values of r , is a prerequisite for the applicability of the design charts developed in this section. If the interface sticks (static friction), the case of a perfectly bonded interface applies (see section 5.5).

For the case treated here, the order of the singularity depends on the Dundurs parameters α and β , the wedge angle θ_2 , the coefficient of friction μ , and, surprisingly, on the direction of relative motion. Both directions of relative motion can be treated at the same time by allocating a sign to the coefficient of friction μ . If the wedge in Figure 5.19 slides to the right (away from the potentially singular point), the coefficient of friction is said to have a positive sign and vice versa. The appropriate boundary condition at the interface is then:

$$\sigma_{r\theta} = -\mu \sigma_{\theta\theta}, \quad \sigma_{\theta\theta} < 0 \quad (5.26)$$

with $\mu < 0$ or $\mu > 0$, depending on the direction of motion.

The eigenvalue equation, taken from [Comninou, 1976], reads:

$$\begin{aligned} \mathcal{D}(\theta_2, \mu, \alpha, \beta, p) = & (1 + \alpha) \cos(p\pi) (\sin^2(p\theta_2) - p^2 \sin^2(\theta_2)) + \\ & + \frac{1}{2} (1 - \alpha) \sin(p\pi) (\sin(2p\theta_2) + p \sin(2\theta_2)) + \\ & + \mu \sin(p\pi) [(1 - \alpha)p(1 + p) \sin^2(\theta_2) + \\ & - 2\beta (\sin^2(p\theta_2) - p^2 \sin^2(\theta_2))] \end{aligned} \quad (5.27)$$

5.7.2 Design Charts

Two design charts are needed here to fully describe one material combination: One for a wedge made of material 1 sliding on a body made from material 2 and vice versa⁽⁶⁾. As will be shown, the two design charts are not only quantitatively but also qualitatively different.

Figure 5.21 shows the design chart for the case of an aluminum wedge (the more compliant material) sliding on a body made from steel (the stiffer material). While Figure 5.21(a) shows the real part of the singularity exponent ω_1 , Figure 5.21(b) shows the imaginary part. Additionally, Figure 5.23(a) show $\text{Re}(\omega_1)$ for selected coefficients of friction.

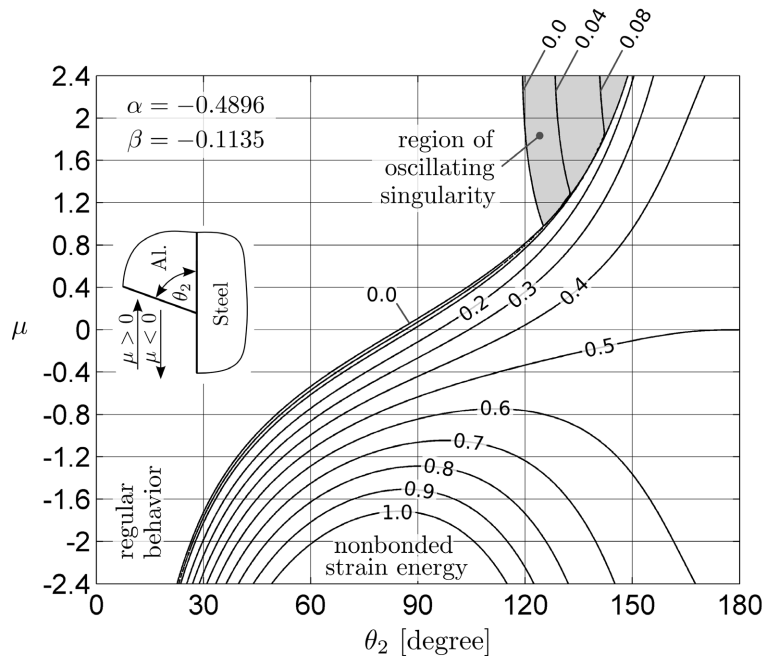
The curve of transition from regular to singular behavior is denoted by “0.0” in Figure 5.21(a). For very large, positive coefficients of friction (wedge sliding to the right) a region of oscillating singularity (shaded gray) is found.

An important observation coming from the design chart in Figure 5.21(a) is that for any wedge angle the order of the singularity increases with a decrease in the (signed) coefficient of friction. That is, the singularity is always more severe when the wedge slides to the left ($\mu < 0$) than when the wedge slides to the right ($\mu > 0$). As in the paper by Churchman et al. [2003] this behavior is here referred to as “Type A”.

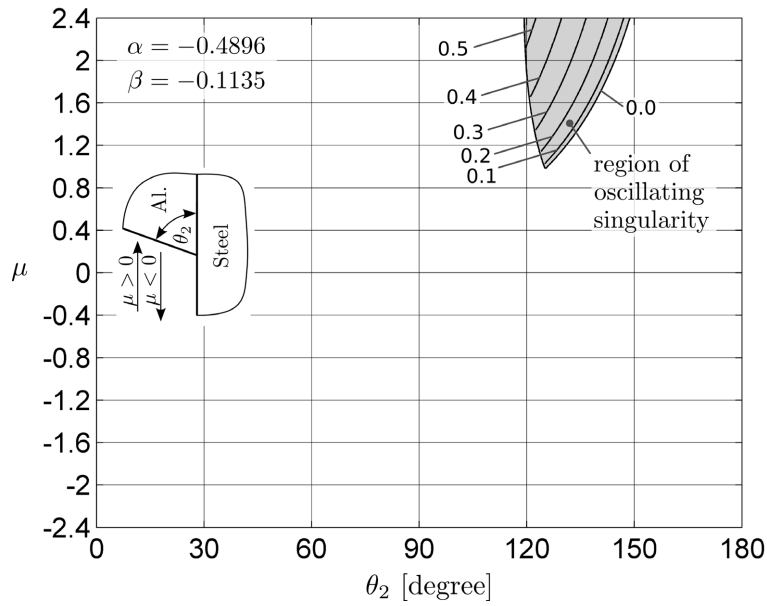
It is a startling observation illustrated by the design charts that an increase of the coefficient of friction may, depending on the direction of relative motion, decrease the order of the singularity or even change the stress field from singular to regular. For example, an aluminum wedge width $\theta_2 = 90^\circ$ in frictionless contact ($\mu = 0$) with a body made from steel yields a stress singularity with $\omega_1 = 0.1102$, see Figure 5.21(a). If the wedge slides to the right and the coefficient of friction increases to, say, $\mu = 0.2$, a regular stress field is obtained.

For absolutely very large, negative coefficients of friction the singularity exponent ω_1 reaches 1.0 in Figure 5.21(a). As will be explained in Section 5.8.1, stress singularities with $\omega_1 \geq 1.0$ are not physically significant as such singularities would correspond to an infinite amount of strain energy. It is therefore very likely that sliding is not attainable in the region labeled “nonbonded strain energy” in Figure 5.21(a).

⁽⁶⁾Exchanging the materials (material 1 becomes material 2 and vice versa) changes the Dundurs parameter α to $-\alpha$ and β to $-\beta$.

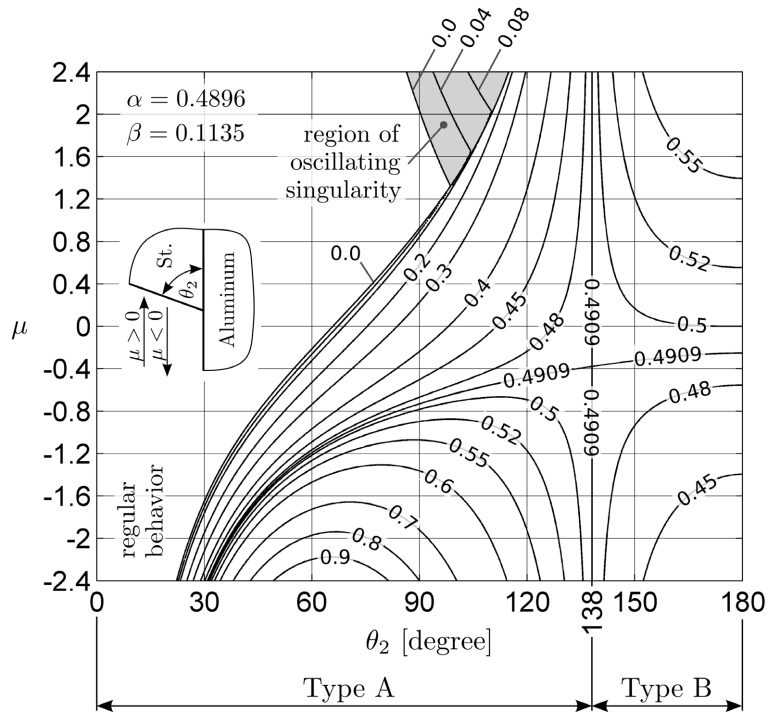


(a) Real part of the singularity exponent $\text{Re}(\omega_1)$.

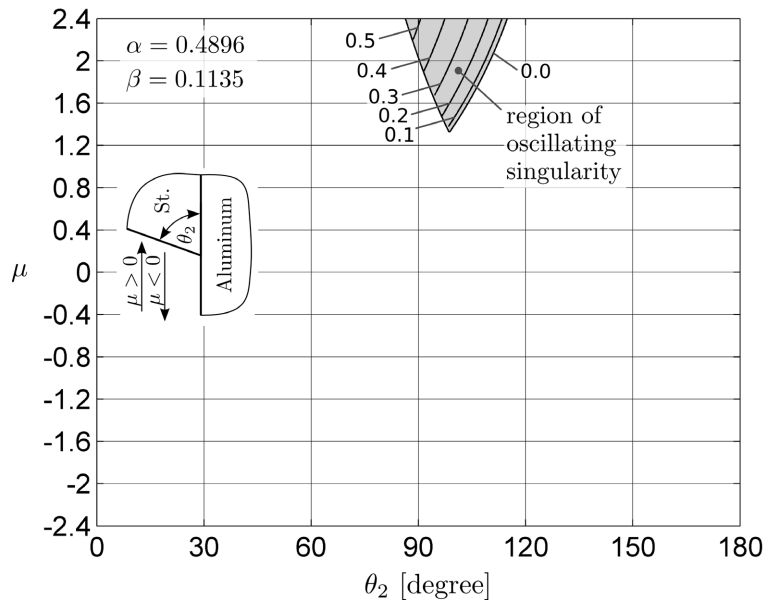


(b) Imaginary part of the singularity exponent $\text{Im}(\omega_1)$.

Figure 5.21: Design chart for an aluminum wedge frictionally sliding on a body made from steel. If the wedge is sliding to the right the coefficient of friction μ has a positive sign and vice versa.



(a) Real part of the singularity exponent $\text{Re}(\omega_1)$.



(b) Imaginary part of the singularity exponent $\text{Im}(\omega_1)$.

Figure 5.22: Design chart for a steel wedge frictionally sliding on a body made from aluminum. If the wedge is sliding to the right the coefficient of friction μ has a positive sign and vice versa.

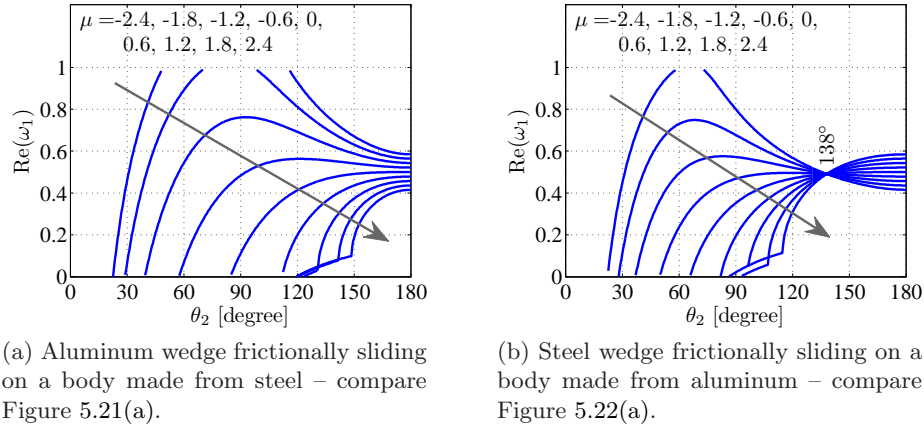

 Figure 5.23: $\text{Re}(\omega_1)$ for different coefficients of friction.

Figure 5.22 shows the design chart for the case of a steel wedge (the stiffer material) sliding on a body made from aluminum (the more compliant material). While Figure 5.22(a) shows the real part of the singularity exponent ω_1 , Figure 5.22(b) shows the imaginary part. Additionally, Figure 5.23(b) show $\text{Re}(\omega_1)$ for selected coefficients of friction.

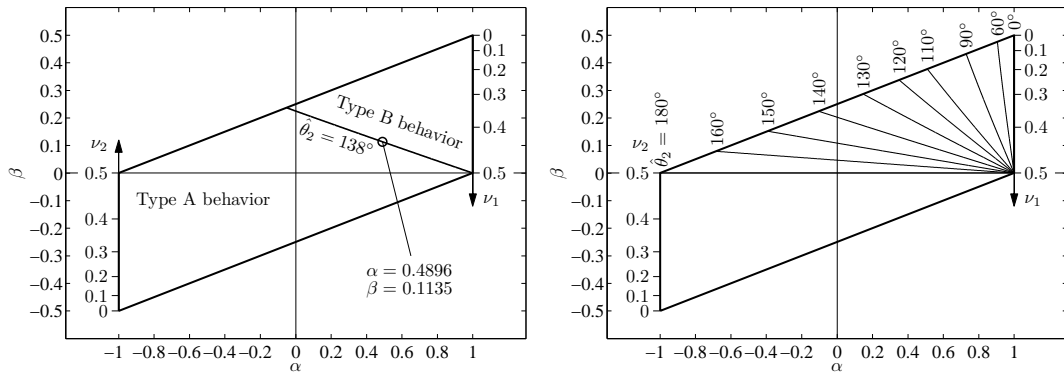
Obviously, the design chart in Figure 5.22 is qualitatively different from the one in Figure 5.21. The design chart in Figure 5.22(a) shows “Type A” behavior (the order of the singularity increases with a decrease in the coefficient of friction) for $\theta_2 < 138^\circ$, only. For $\theta_2 > 138^\circ$ the order of the singularity decreases with a decrease in the (signed) coefficient of friction. This behavior is here referred to as “Type B”.

As can be seen from Figure 5.22(a), the boundary between Type A and Type B behavior is independent of the coefficient of friction. In their paper, Churchman et al. [2003] show that this is always the case and derive a set of equations that determines the boundary delimiting the two kinds of behavior. These equations are used but not reproduced here.

As the boundary between Type A and Type B behavior is independent of the coefficient of friction, for each wedge angle $\hat{\theta}_2$ there exists a curve in the α - β -plane delimiting the two responses. Figure 5.24(a) shows this curve for $\hat{\theta}_2 = 138^\circ$. The curve passes through $(\alpha, \beta) = (0.4896, 0.1135)$, which are the Dundurs parameters for a steel wedge sliding on a body made from aluminum.

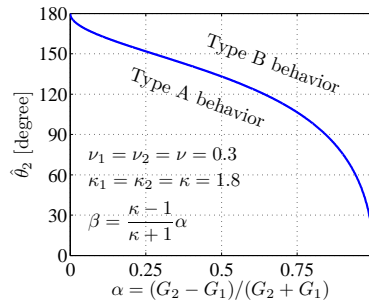
Figure 5.24(b) shows curves delimiting the two responses for selected wedge angles $\hat{\theta}_2$ ranging from 0° to 180° . All the curves pass through $(\alpha, \beta) = (1, 0)$. It can also be seen from Figure 5.24(b) that only type A behavior is found for $\beta < 0$, for instance for the case of a aluminum wedge sliding on a body made from steel.

Finally, Figure 5.24(c) shows the delimiting angle $\hat{\theta}_2$ for Poisson’s ratio $\nu_1 = \nu_2 = 0.3$ as a function of α , for α ranging from 0 ($G_2 = G_1$) to 1 ($G_2/G_1 \rightarrow \infty$). It can be



(a) Curve for $\hat{\theta}_2 = 138^\circ$.

(b) Curves for selected wedge angles $\hat{\theta}_2$



(c) Delimiting angle $\hat{\theta}_2$ for Poisson's ratio $\nu_1 = \nu_2 = 0.3$ as a function of α .

Figure 5.24: Curves delimiting type A and B responses.

seen that the more different the shear moduli are, the smaller is the wedge angle $\hat{\theta}_2$ delimiting type A and B responses.

The design charts presented in this section can be used to identify possible stress singularities and to modify the local geometry in order to minimize the singularity exponent. Ideally, the singularity should be completely removed. In the case of cycling loading both directions of relative motion may occur alternately. In these cases, it is recommended to choose an angle θ_2 , which for both directions of relative motion leads to a regular stress field.

5.7.3 Examples

In this section, two generic structures designated as example D and E are studied using linear finite element analysis. The two examples demonstrate how the design charts can be used to modify the local geometry in order to completely remove the singularity for the case of a wedge frictionally sliding on a body with smooth surface.

The structures have been analyzed assuming plane strain. The material properties used are given in Table 5.1. The coefficient of friction is assumed to be $\mu = 0.2$.

Figures 5.25(a) and (b) show the geometries of Examples D and E, respectively. An aluminum block is sliding on a steel body. The potentially singular point investigated here is located at $r = 0$.

As shown in Figure 5.26, the analysis consists of three steps:

- Step 1: The aluminum block is loaded by a distributed load $t = 100$ MPa, while the displacement u at the lower edge of the aluminum block is kept equal to zero.
- Step 2: A positive displacement $u = \hat{u}$ is prescribed at the lower edge of the aluminum block. The displacement \hat{u} is chosen sufficiently large so that a further increase of u would not change the stress state (viewed from a coordinate system moving with the singular point at $r = 0$).
- Step 3: A negative displacement $u = -\hat{u}$ is prescribed at the lower edge of the aluminum block.

For example D the wedge angle θ_2 equals 90° . As can be seen from the design chart in Figure 5.21(a), the stress state is singular with $\omega_1 = 0.2584$ when the aluminum block is moving upward (step 1 and 2) and regular when it is moving downward (step 3). The design charts also shows that decreasing the wedge angle to $\theta_2 = 70^\circ$, as in example D, yields a regular stress state for both directions of relative motion.

Figures 5.25(c) and (d) show plots of the normal stress at the interface at the end of each step for examples D and E, respectively. Figures 5.25(e) and (f) show the corresponding double logarithmic plots.

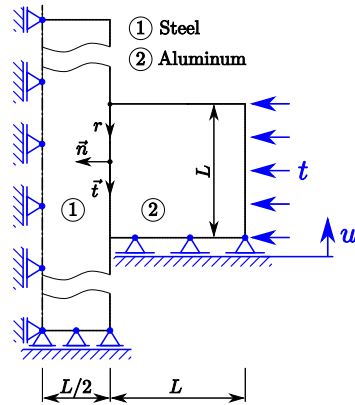
In the case of example D the stress state is singular for step 1 (the aluminum block is locally sliding upward when the distributed load t is applied) and step 2. The stress state is regular for step 3, as expected from the design chart. The slope of the curves for step 1 and 2 in the double logarithmic plot is in good agreement with the predicted value of the singularity exponent ω_1 .

In the case of example E the stress state is regular for all three steps, as can be seen in Figure 5.25(d). Step 3 leads to a local loss of contact indicated by a small region where $\sigma_{nn} = 0$ in Figure 5.25(d).

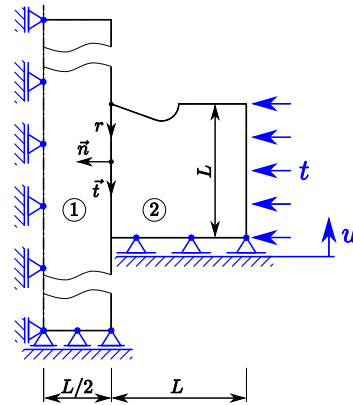
5.7.4 Some Remarks on Fretting Fatigue

There is a close connection between the singular stress state at the boundary of a contact surface discussed in this section and the phenomenon known as “fretting fatigue”.

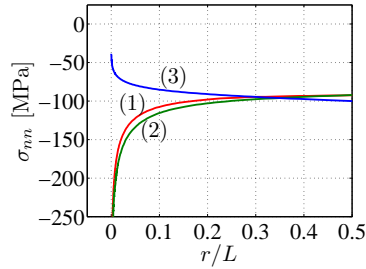
The term “fretting” refers to a type of surface damage found at contact interfaces exhibiting small, oscillatory sliding motions. These sliding motions can be caused by



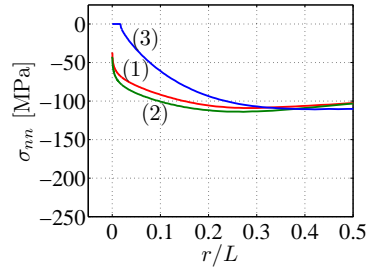
(a) Example D; $\theta_2 = 90^\circ$, $\mu = 0.2$, $\omega_1 = 0.2584$ or regular stress field.



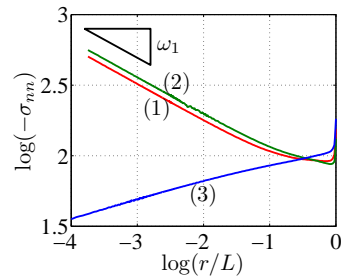
(b) Example E; $\theta_2 = 70^\circ$, $\mu = 0.2$, regular stress field



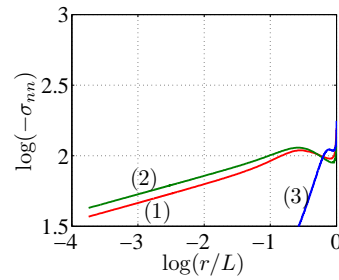
(c) Example D; normal stress at the interface at the end of each step.



(d) Example E; normal stress at the interface at the end of each step.



(e) Example D; double logarithmic plot.



(f) Example E; double logarithmic plot.

Figure 5.25: Examples D and E: Removing stress singularities from sliding interfaces.

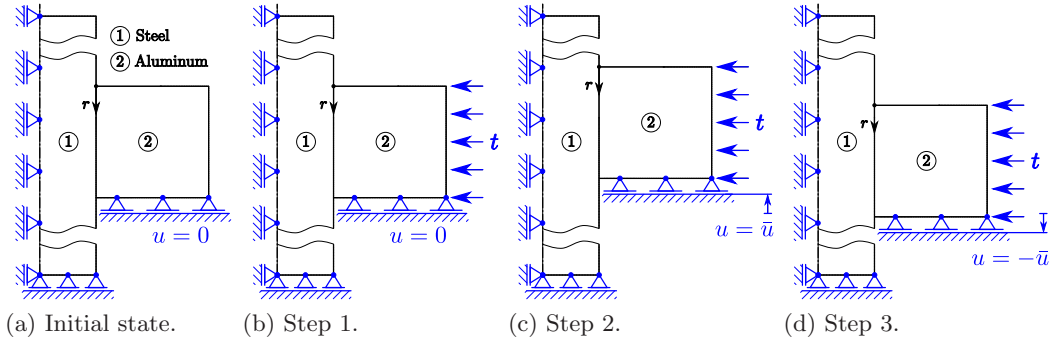


Figure 5.26: Analysis steps for Examples D and E.

cyclic loading of the structure. In the fretting zone cracks can be initiated that severely reduce fatigue life as compared to a configuration without contact. This reduction of the fatigue life is referred to as “fretting fatigue”.

Methods have been developed to predict surface crack initiation under fretting fatigue conditions based on the similarity of the singular stress field at the boundary of a contact surface (as discussed in this section) and the singular stress field at a crack tip – see [Giannakopoulos et al., 1998], [Nowell et al., 2006].

The design charts presented in this section can be used to modify local geometries in order to minimize the singularity exponent or, ideally, completely remove the singularity. It is reasonable to assume that these modifications help to prevent fretting fatigue crack initiation and thereby increase fatigue life of the structure.

5.8 Closing Remarks

5.8.1 Upper Limit for the Singularity Exponent

As mentioned before, a singularity exponent ω_1 larger than or equal to 1.0 is not physically significant. To show this, the total strain energy stored in a region close to the singular point ($0 \leq r \leq a$) is computed here for the case of a reentrant corner in a linear elastic, purely mechanically loaded (i.e. without any eigenstrains resulting from thermal loading or other sources) body, see Figure 5.27.

Using Einstein’s summation convention the elastic strain energy density U' can be written as

$$U' = \frac{1}{2} \sigma_{ij} \varepsilon_{ij} = \frac{1}{2} \sigma_{ij} C_{ijkl} \sigma_{kl} , \quad (5.28)$$

where σ_{ij} and ε_{ij} are the stress and strain tensor, respectively, and C_{ijkl} is the fourth rank compliance tensor.

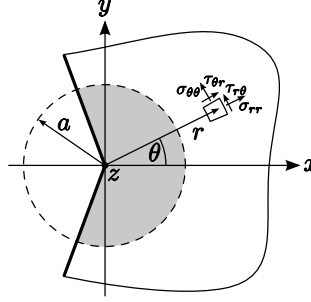


Figure 5.27: Region for which the strain energy is considered.

The total strain energy stored in the region $0 \leq r \leq a$, see Figure 5.27, is:

$$U = h \int_0^a \int_{-\theta_1}^{\theta_2} \frac{1}{2} \sigma_{ij} C_{ijkl} \sigma_{kl} r \, d\theta \, dr, \quad (5.29)$$

where h is the out-of-plane thickness.

Insertion of the singular stress field as described by Equation (5.2) into Equation (5.29) yields:

$$U = \frac{hK^2L^{2\omega}}{2} \int_0^a r^{1-2\omega} \underbrace{\int_{-\theta_1}^{\theta_2} F_{ij}(\theta) C_{ijkl} F_{kl}(\theta) \, d\theta}_{\chi} \, dr \quad (5.30)$$

The index “1” referring to the largest singularity exponent ω_1 in Equation (5.2) has been omitted here. The inner integral in Equation (5.30) yields a finite value χ , hence:

$$U = \frac{hK^2L^{2\omega}\chi}{2} \int_0^a r^{1-2\omega} \, dr = \begin{cases} \frac{hK^2L^{2\omega}\chi}{2} \frac{a^{2-2\omega}}{(2-2\omega)} & \text{for } \omega < 1 \\ \infty & \text{for } \omega \geq 1. \end{cases} \quad (5.31)$$

The integral in Equation (5.31) only yields a finite value if the magnitude of the singularity exponent ω is smaller than 1. Thus, if ω was larger than or equal to 1.0 the strain energy stored in an arbitrarily small region around the singular point would be infinite, which is of course impossible. It can be concluded that singularity exponents ω_1 larger than or equal to 1.0 are not physically significant.

5.8.2 Wedge Solver

Lee and Barber [2006] have presented a program called *Wedge Solver* (see Figure 5.28) that can determine the asymptotic elastic stress fields at singular points for a variety of cases. After entering the local geometry, the material properties, the boundary conditions and the interface conditions, the program computes the singularity exponents

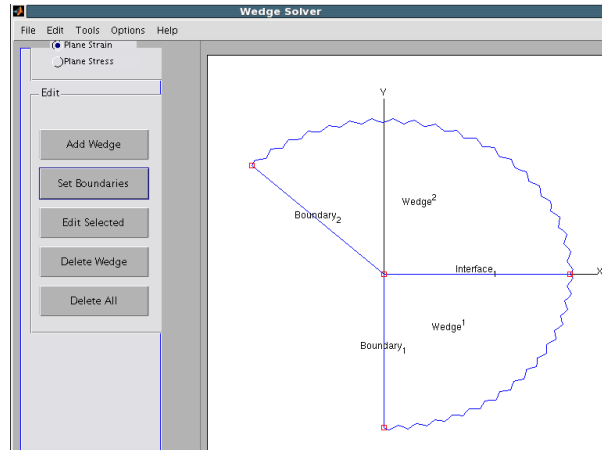


Figure 5.28: Screenshot of the Wedge Solver Program [Lee and Barber, 2006].

ω_k and outputs explicit expressions for the singular stress field. The program can be downloaded free of charge⁽⁷⁾.

For a small subset of parameter combinations, the results given in Sections 5.5.2, 5.6.2 and 5.7.2 have been cross-checked using the Wedge Solver program (version 1.0). As for the results in Sections 5.5.2 and 5.7.2 the singularity exponents computed by the Wedge Solver program are in perfect agreement with the results presented here. As for the results in Section 5.6.2 (the case of a corner in a perfectly bonded interface), the singularity exponents computed by the Wedge Solver program are different from the results presented here. Because the singularity exponents computed by the Wedge Solver program are also not in agreement with results presented in the literature (Bogy [1971], Chen and Nisitani [1993]), the author believes that there is a bug in the program affecting the case of a corner in a perfectly bonded interface.

5.9 Summary

This chapter has examined stress singularities which occur at bimaterial interfaces under a variety of circumstances.

Design charts, which exhibit the singularity exponent as function of the local geometry (or the local geometry and the coefficient of friction) for a given material combination, have been developed for three configurations of practical importance

The singularity exponent can be seen as a measure of the “severeness of the high stresses”. As the order of the stress singularity does not depend on the type of loading

⁽⁷⁾<http://www-personal.umich.edu/~jbarber/asymptotics/intro.html>

applied, the design charts are universal in application.

Using the design charts, stress singularities in a given structure can be identified and geometry modifications can be determined that minimize the order of the singularity or, ideally, completely remove the stress singularity. As a result, the durability of the structure will be enhanced.

As confirmed by a number of examples presented in this chapter, great improvements can often be achieved through comparatively small and local modifications of the geometry (see for example Figure 5.11 or 5.25).

Chapter 6

Step-Bars with Axisymmetric Inserts

6.1 Introduction

In the framework of the project *Austrian Light Weight Structures*, aluminum step-bars with various axisymmetric steel inserts were produced by Leichtmetallkompetenzzentrum Ranshofen (LKR)⁽¹⁾ using low pressure die casting. The inserts are made from steel S355, the step bar is made from aluminum alloy A356.0. Information on both materials can be found in Section 2.3.

The design of the inserts incorporates two possibilities of compound casting technology: the form-locking and the frictional connection. The third possibility, metallurgical bonding, has been consciously omitted.

A step-bar with 12 inserts located in the inner four steps is shown in Figure 6.1(a). The inner four steps are 10 mm, 15 mm, 20 mm and 25 mm high. For the 20 mm high step, the geometry and designation of the different inserts is shown in Figure 6.2.

⁽¹⁾<http://www.lkr.at>

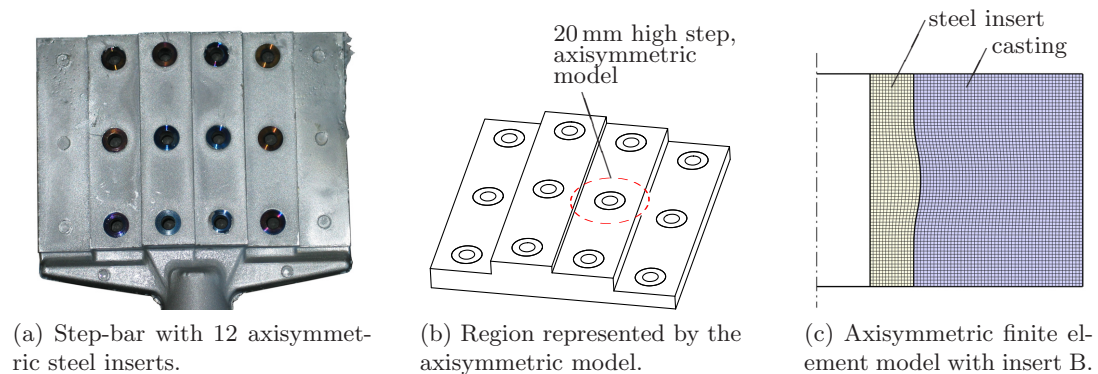


Figure 6.1: Step-bar with steel inserts and axisymmetric model. Picture (a) courtesy of Leichtmetallkompetenzzentrum Ranshofen

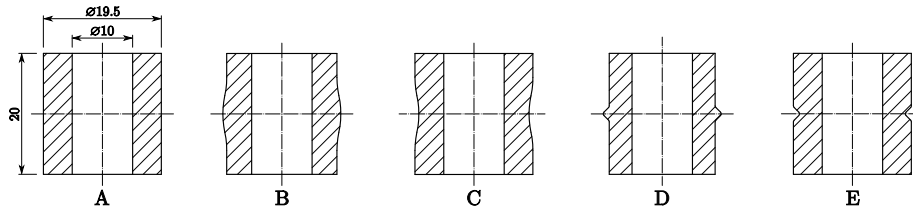


Figure 6.2: Geometry and designation of the steel inserts for the 20 mm high step.

All inserts are machined from a round rod with a diameter of 20 mm. Insert A results in a purely frictional connection, whereas inserts B to E result in a force- and form-locking connections. In order to be able to push the inserts out during mechanical testing⁽²⁾, only “moderate” form-locking connections have been used.

During the casting process the inserts were held in place by extended ejector pins which are normally used to eject the solidified step-bar from the mold.

After the casting process, the step-bar was removed from the mold as early as possible, transported to the quench tank and immediately quenched in water. No further heat treatment was performed, so that the residual stresses that develop during the quenching process persist and determine the frictional connection of the structure. As the aluminum’s coefficient of thermal expansion is about twice that of the steel, the aluminum basically shrinks on to the steel inserts during the quenching process.

6.2 Finite Element Simulation of Quenching and Mechanical Testing

Fundamental considerations regarding the simulation of the quenching process of a compound casting have been given in Chapter 2 and 3. The basic assumptions made for the simulations presented in this section are therefore stated only briefly. The general purpose finite element program ABAQUS Standard⁽³⁾ [Dassault Systèmes, 2008a] has been used to carry out the simulations.

Axisymmetric finite element models have been used for the simulation of the quenching process and the subsequent push-out tests. These models approximately represent the region in the vicinity of the middle steel insert in the 20 mm high step as shown in Figure 6.1(b) and (c). To account for the effects of neighbouring inserts, the nodes on the outer radius of the axisymmetric model are constrained to have the same radial displacement.

⁽²⁾A testing machine with a maximum force of 100 kN was available.

⁽³⁾<http://www.simulia.com>

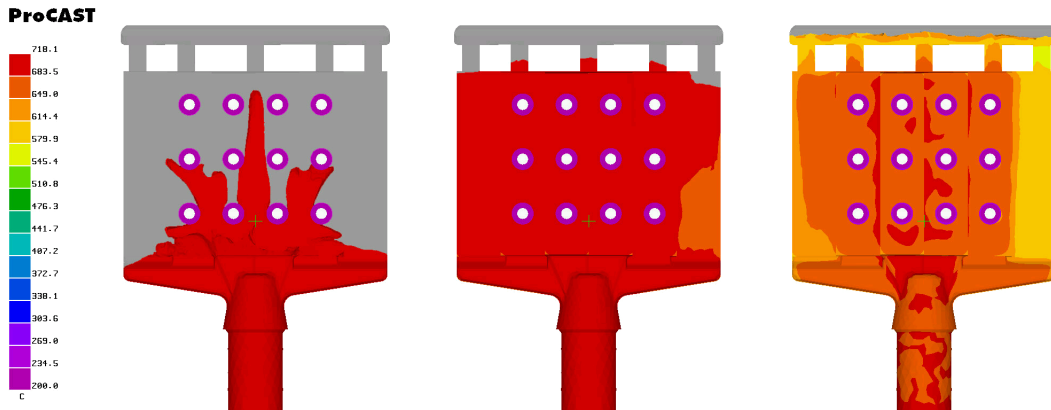


Figure 6.3: Three dimensional casting simulation (thermal problem only); colors indicate temperature in Celsius. Image courtesy of Leichtmetallkompetenzzentrum Ranshofen.

A three-dimensional casting simulation (thermal problem only) carried out by Leichtmetallkompetenzzentrum Ranshofen showed that the temperature distribution in the step-bar is very inhomogeneous at the time of immersion into the quenching water, see Figure 6.3. In the region represented by the axisymmetric finite element model, however, an approximately homogeneous temperature of about 400°C is found in the aluminum and the steel insert. Therefore, it is assumed that at the beginning of the quenching simulation the insert and the surrounding aluminum exhibit a homogeneous temperature of 400°C . Moreover, it is assumed that the model is still stress free at that time (see remarks in Section 2.5).

The complete sequence of simulation steps using the axisymmetric model is as follows:

- Simulation of the quenching process.
- Expansion of the yield surface to account for the effects of natural ageing (see Figure 2.7 on page 26).
- Simulation of push-out tests.

For the quenching simulation, the heat transfer coefficient is taken to be a function of the surface temperature as shown in Figure 6.4. Lower values are assumed at the inner surface of the steel insert to account for the effects of “entrapped vapor” (see also Section 2.2).

Thermal contact conductance at the steel aluminum interface is taken as a function of contact pressure and macroscopic gap width as described in Section 3.5.

Von Mises rate-independent plasticity with isotropic hardening is assumed for aluminum and steel (see Section 2.5). Stress-strain curves for the relevant temperature range are given in Figure 2.7 on page 26 for A356.0 and in Figure 2.8(a) on page 27 for

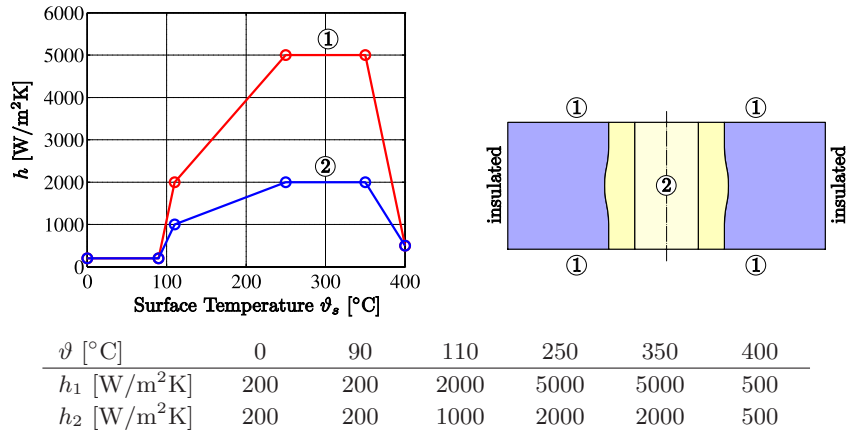


Figure 6.4: Dependence of heat transfer coefficient h on surface temperature ϑ ; initial temperature: 400 °C; $T_\infty = 20$ °C.

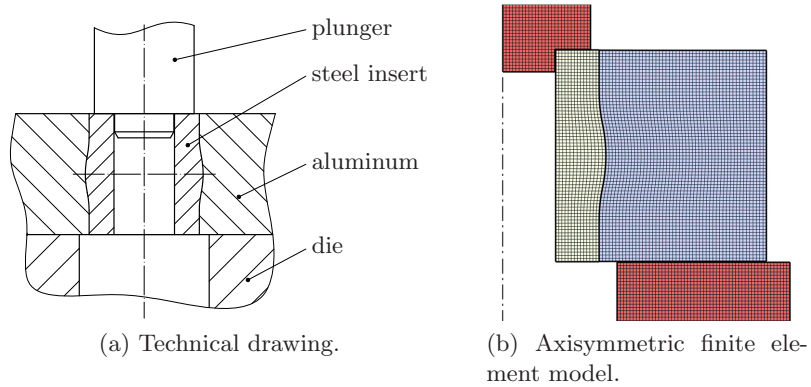


Figure 6.5: Push-out test.

S355. Further required thermophysical and mechanical material properties are given in Section 2.8.

Coulomb's law of friction is assumed at the steel-aluminum interface. The coefficient of friction is assumed to be $\mu = 0.4$. The static and the kinetic coefficient of friction are assumed to be identical.

The geometry has been meshed with quadrilateral elements of type CAX4RT (4-node, linear, coupled temperature-displacement element with reduced integration and hour-glass control). For example, Figure 6.1(c) shows the mesh used for insert B. Second order elements could not be used as spurious (nonphysical) oscillations appeared in the solution during quenching simulation, see [Dassault Systèmes, 2008a].

To accurately model the push-out test, a deformable plunger and die have been included in the axisymmetric finite element model, see Figure 6.5.

The damage indicator described in chapter 4 is used to predict the onset of fracture in the aluminum alloy A356.0 during the push-out test. The critical strain in uniaxial tension ε_0 needed for the calibration of Equation (4.4) is chosen as $\varepsilon_0 = 0.05$.

6.3 Simulation Results and Comparison to Experimental Data

Figure 6.6 illustrates the evolution of the temperature field (left column), the radial stresses (middle column) and the contact pressure at the steel-aluminum interface (right column) during the quenching process for insert A. Note that each plot has a different color legend and that the radial deformations are scaled by a factor of 40.

It can be observed that immediately after immersion of the casting into the quenching water a gap opens up at the steel-aluminum interface and closes again after several seconds. The maximum width of the gap is about $17\ \mu\text{m}$. As apparent from the plots of the contact pressure (Figure 6.6, right column), only about half of the insert's outer surface continuously remains in contact with the surrounding aluminum during the quenching process!

As the thermal contact conductance at the steel-aluminum interface decreases with increasing gap width (see Figure 3.9 on page 48), heat is forced to flow mainly parallel to the open gap and a temperature drop ΔT can be observed at the interface while the gap is open.

After complete cooling, a high level of contact pressure (about 80 MPa) and hence a strong frictional connection is obtained, see Figure 6.6(o).

Figure 6.7 compares the residual stress states obtained after quenching for the different steel inserts shown in Figure 6.2. Radial stresses (left column) and the contact pressure at the steel-aluminum interface (right column) are shown. The contact pressure is plotted versus the normalized distance along the interface, i.e. the path length along the interface divided by the full length of the interface.

Compared to the straight insert A, the “convex” inserts B and D yield a local increase, the “concave” inserts C and E a local decrease of the contact pressure. Extremely large contact pressures are obtained in the region of the “steel tip” of insert D, whereas contact is completely lost in the region of the “aluminum tip” of insert E.

Figure 6.8 compares the measured force-displacement curves during the push-out tests (left column) to the ones obtained by simulation (middle column).

During the push out tests, only the force and the crosshead displacement of the testing machine were recorded. The crosshead displacement includes deformations of the testing machine not reproduced by the finite element models. Thus, in terms of displacement, the measured force-displacement curves (force versus crosshead displacement)

Chapter 6 Step-Bars with Axisymmetric Inserts

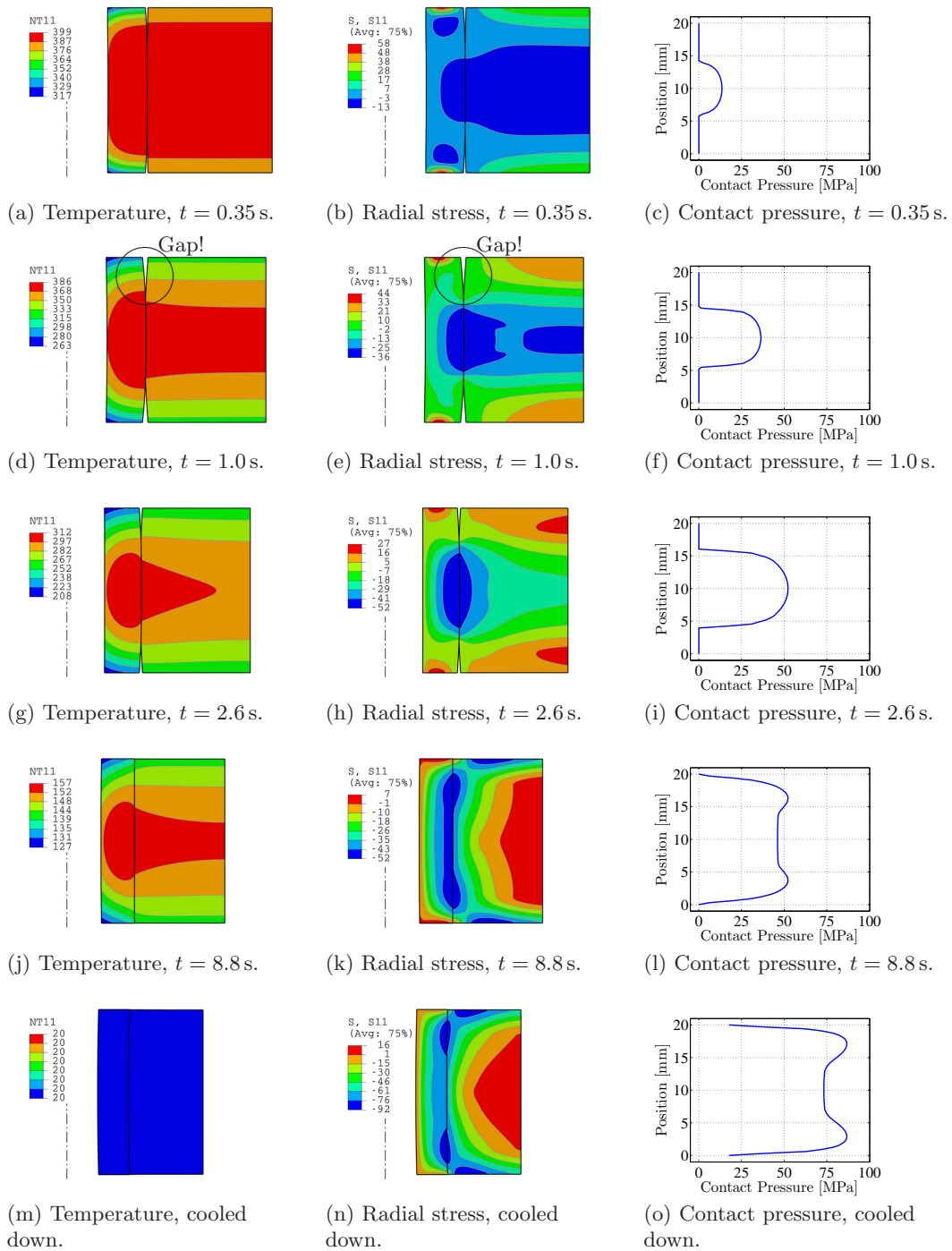
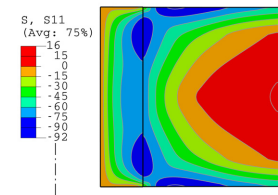
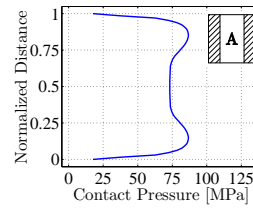


Figure 6.6: Insert A: Temperature (Celsius), radial stress (MPa) and contact pressure t seconds after immersion into the quenching water; radial deformation scaled by a factor of 40; note the different color legends.

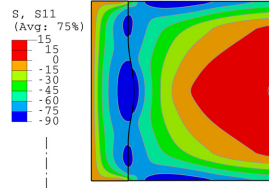
Chapter 6 Step-Bars with Axisymmetric Inserts



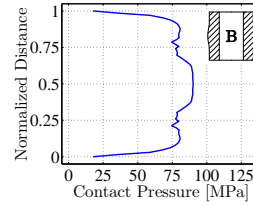
(a) Insert A; radial stress.



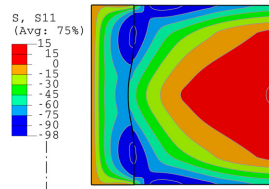
(b) Insert A; contact pressure.



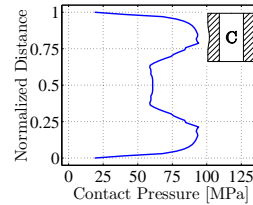
(c) Insert B; radial stress.



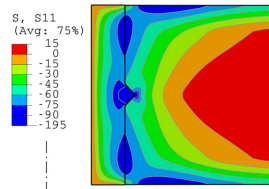
(d) Insert B; contact pressure.



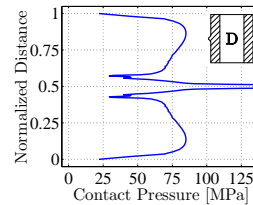
(e) Insert C; radial stress.



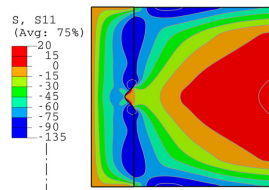
(f) Insert C; contact pressure.



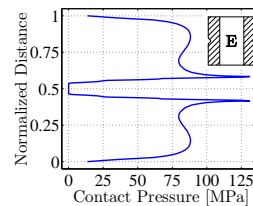
(g) Insert D; radial stress.



(h) Insert D; contact pressure.



(i) Insert E; radial stress.



(j) Insert E; contact pressure.

Figure 6.7: Radial stress (MPa) and contact pressure after quenching for all inserts.

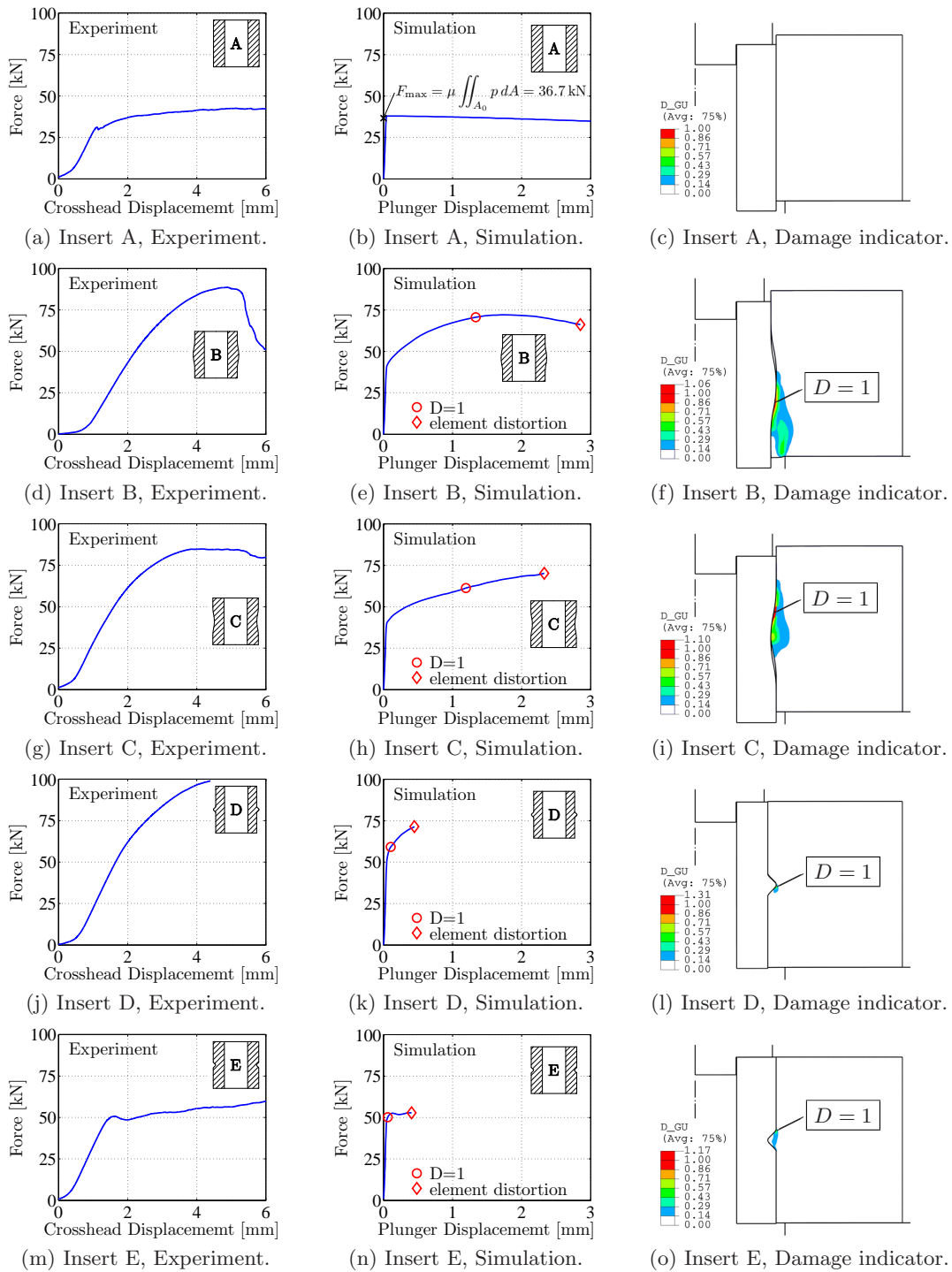


Figure 6.8: Push-out test: Comparison of measured force-displacement curves (left column) to the ones obtained by simulation (middle column); position where the critical value of the damage indicator is reached (right column).

can only be qualitatively compared to the curves obtained by simulation (force over plunger displacement).

With the exception of the model for insert A, all simulations had to be stopped when element distortions close to the steel-aluminum interface became unacceptably large. Especially in the case of insert D, see Figure 6.8(k), the simulated force would continue to increase if simulation was continued.

On the simulated force-displacement curves the point where the damage indicator reaches the critical value $D = 1$ is marked by a circle. The position where the critical value of the damage indicator is reached, is shown in the right column of Figure 6.8.

In the case of insert A (purely frictional connection), the force corresponding to the onset of sliding at the steel-aluminum interface, see Figure 6.8(b), is in good agreement with the integral of the initial contact pressure p over the contact surface A_0 multiplied by the coefficient of friction μ :

$$F_{\max} = \mu \iint_{A_0} p \, dA = 36.7 \text{ kN} . \quad (6.1)$$

6.4 Discussion

In this chapter aluminum step-bars with various axisymmetric steel inserts and a corresponding finite element models for the simulation of the quenching process and the subsequent push-out test have been presented.

The simulations show that a gap opens up at the steel-aluminum interface at the beginning of the quenching process and closes again after several seconds (see Figure 6.6). The opening of the gap severely reduces the thermal contact conductance at the interface and forces heat to flow mainly parallel to the open gap.

The force-displacement curves recorded during push-out tests are generally in good agreement with the ones obtained by simulation.

For all inserts investigated a strong frictional connection is obtained. The axial force corresponding to the onset of sliding at the steel-aluminum interface is only slightly increased by the “moderate” form-locking geometries investigated here. However, all form-locking connections result in a marked increase of the ultimate axial load.

Insert D exhibits the highest ultimate load. However, cracks are initiated ($D = 1$) long before the ultimate load is reached as shown by the simulation.

In the case of insert A (purely frictional connection), the simulation predicts a continuous decrease of the push-out force after the onset of sliding at the steel-aluminum interface, see Figure 6.8(b). This is due to the continuous loss of contact area. Remarkably, the measured push-out force increases to a certain extent after the onset of sliding, see Figure 6.8(a). This could indicate that the coefficient of friction actually increases during the sliding motion.

Chapter 7

Demo Prototype of a Compound Casting

7.1 Introduction

In the framework of the project *Austrian Light Weight Structures*, the author has designed a demo prototype of a steel-aluminum compound casting. Around 60 pieces of the demo prototype were manufactured by Leichtmetallkompetenzzentrum Ranshofen (LKR)⁽¹⁾ using high pressure die casting.

The demo prototype is meant to demonstrate the possibilities of the compound casting technology. The design incorporates two possibilities of compound casting technology: the form-locking and the frictional connection. The third possibility, metallurgical bonding, has been consciously omitted.

The first part of this chapter will address the geometry and the manufacturing process of the demo prototype. Next, a finite element analysis of the quenching process, the machining and the mechanical testing is presented. Finally, the simulation results are compared to experimental data.

7.2 Geometry and Manufacturing Process

The task set by LKR was to join two identical, coaxially positioned inserts made from steel C45E by a cast aluminum node made from alloy A356.0. (Information on both materials can be found in Section 2.3.) Moreover, the demo prototype should be designed to carry primarily axial (compressive or tensile) and torsional loads.

Figure 7.1 shows an exploded view of the demo prototype. Only two-thirds of the casting are shown. Figure 7.2 shows a technical drawing.

As the steel inserts have a complicated shape, they have been produced by CNC milling. Large-scale production of similar components would require a more economical production process, e.g. hydroforming.

⁽¹⁾<http://www.lkr.at>

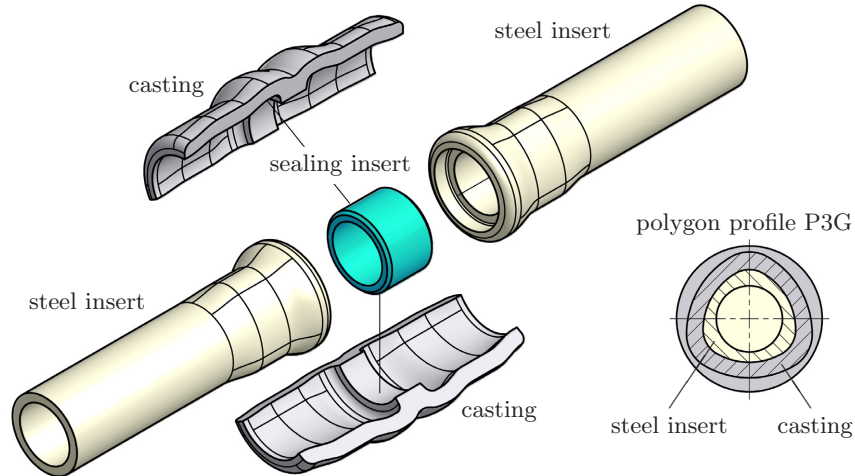


Figure 7.1: Exploded view of the demo prototype; only two-thirds of the casting are shown. The casting gate is not shown.

The cross section of each steel insert smoothly changes throughout its length. Outside of the aluminum node, the steel inserts are tubular in shape. Approaching the center of the node, the cross section changes from a circle to a polygon profile P3G (see Figure 7.1, bottom right). The polygon profile serves as a form-locking connection with respect to torsional loads. Approaching the center of the node further, the cross section changes back to a circle, while the diameter also increases. This increase in diameter serves as a form-locking connection with respect to axial tensile loads.

The polygon profile P3G is a standardized form of a shaft-to-collar connection described in [DIN 32711-1]⁽²⁾. This machined shaft-to-collar connection is not very common because tight geometrical tolerances have to be maintained during production. For the application presented here, obviously, no tight tolerances have to be observed.

Remarkably, the polygon profile P3G is a curve of constant width. That is, the curve's width, measured by the distance between two opposite parallel lines touching its boundary, is the same regardless of the direction of those two parallel lines. We denote this width as D .

The curve can be described by the parametric equation:

$$\begin{aligned} x(\alpha) &= [D/2 - e \cos(3\alpha)] \cos(\alpha) - 3e \sin(3\alpha) \sin(\alpha) , \\ y(\alpha) &= [D/2 - e \cos(3\alpha)] \sin(\alpha) + 3e \sin(3\alpha) \cos(\alpha) , \end{aligned} \quad (7.1)$$

where e is the eccentricity and $\alpha = 0 \dots 360^\circ$ is the parameter⁽³⁾. For the steel inserts

⁽²⁾The proposed technical standard [DIN 32711-1] from Jan. 2007 contains considerably more information than the standard from 1979.

⁽³⁾ α is a parameter, not the angular coordinate of a polar coordinate system.

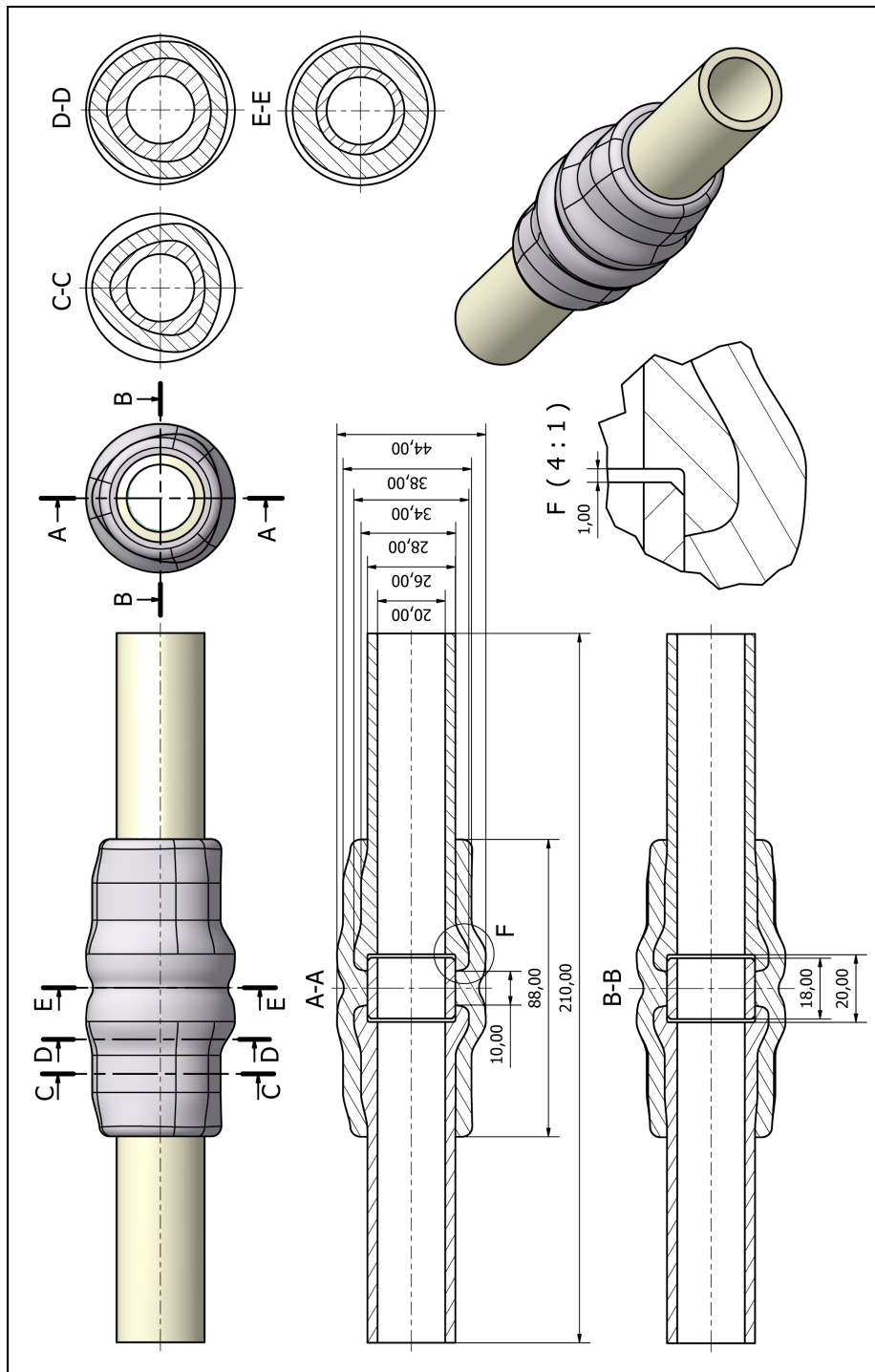
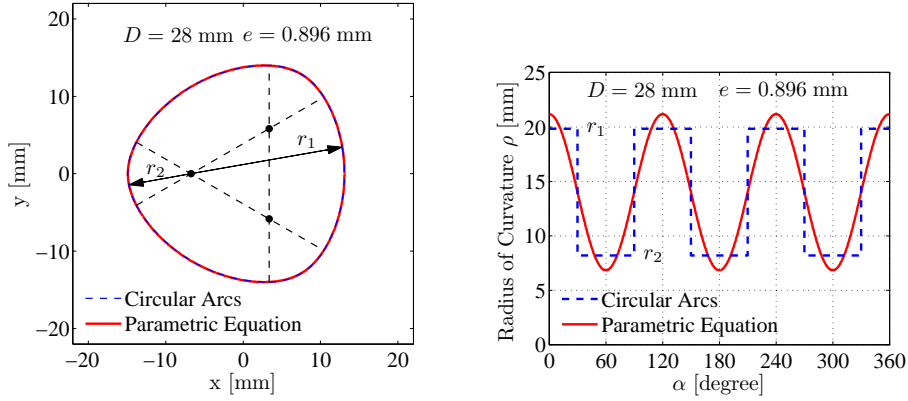


Figure 7.2: Technical drawing of the demo prototype; dimensions in mm.



(a) Plot of Equation (7.1) and approximation by six circular arcs.

(b) Radius of curvature.

Figure 7.3: Polygon profile P3G.

of the demo prototype $D = 28$ mm and $e = 0.896$ mm has been chosen. Figure 7.3(a) shows a corresponding plot of the parametric equation (solid curve).

The geometry of the polygon profile can be approximated by six circular arcs with radii:

$$r_1 = D/2 + 6.5e \quad \text{and} \quad r_2 = D/2 - 6.5e . \quad (7.2)$$

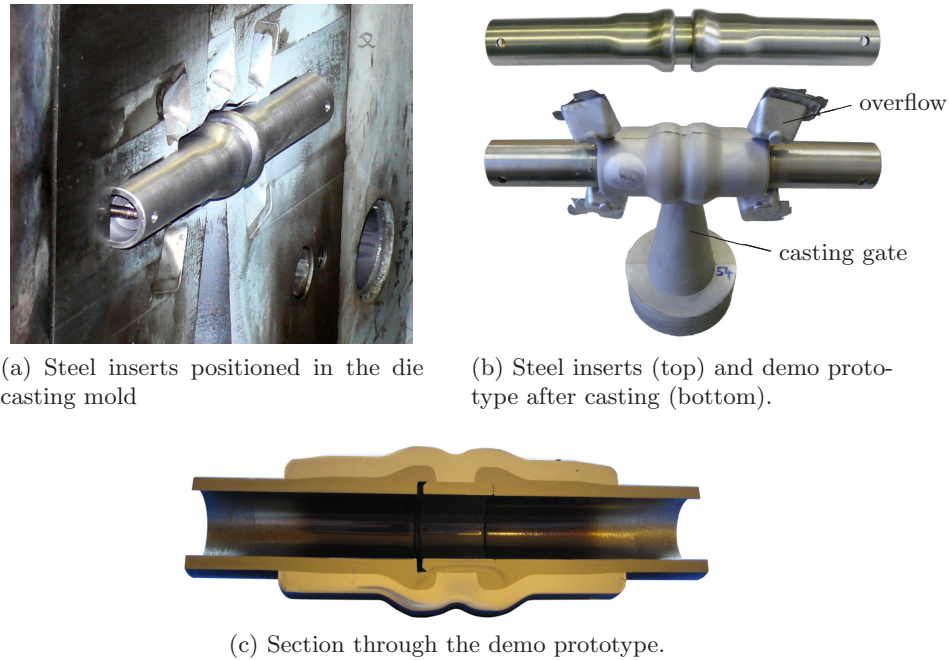
Figure 7.3(a) also shows these six circular arcs (dashed curves). The difference between the parametric equation and the circular arcs is hardly visible to the naked eye. As shown in Figure 7.3(b) the radius of curvature of the curve described by the parametric equation smoothly varies, whereas the radius of curvature of the curve composed of circular arcs jumps between r_1 and r_2 .

As the difference between the real polygon profile P3G and the curve composed of six circular arcs is small, the latter has been used to describe the geometry of the demo prototype. This simplifies the description of the geometry in standard 3D CAD programs and the generation of CNC code to drive the milling machine.

Further information on the polygon profile P3G can be found in [Frank and Pflanzl, 1998].

The “sealing insert” shown in Figures 7.1 and 7.2 is not meant for load transmission. It merely prevents the melt from flowing inside the steel inserts. A tubular part made from steel C45E has been used in the present case. However, a different material or even a removable salt core could be used.

As already mentioned, the demo prototype has been manufactured using high pressure die casting. Figure 7.4(a) shows the steel inserts positioned in the casting mold. Figure 7.4(b) show two steel inserts loosely connected by the sealing insert (top) and a finished casting including the casting gate and four overflows (bottom). The four



(a) Steel inserts positioned in the die casting mold

(b) Steel inserts (top) and demo prototype after casting (bottom).

(c) Section through the demo prototype.

Figure 7.4: Manufacturing of the demo prototype. Pictures courtesy of Leichtmetallkompetenzzentrum Ranshofen.

overflows are later broken off and the casting gate is machined off. Figure 7.4(c) shows a cross section of the demo prototype. The cutting plane is slightly off-center, as the release of the residual stresses cause the steel parts to separate from the aluminum node when the structure is cut in the middle.

The pressure used to force the molten aluminum into the mold during high pressure die casting can exceed 100 MPa. Inserts have to be able to withstand this pressure, which can be an important factor in the design of such inserts. For instance, Figure 7.5 shows the von Mises equivalent stress in the cross section of the steel inserts of the demo prototype loaded by a pressure of $p = 80$ MPa (linear elastic finite element analysis assuming plane stress conditions).

After casting, the demo prototype was removed from the mold as early as possible, transported to the quench tank and immediately quenched in water. No further heat treatment was performed, so that the residual stresses that develop during the quenching process persist and determine the frictional connection of the structure.

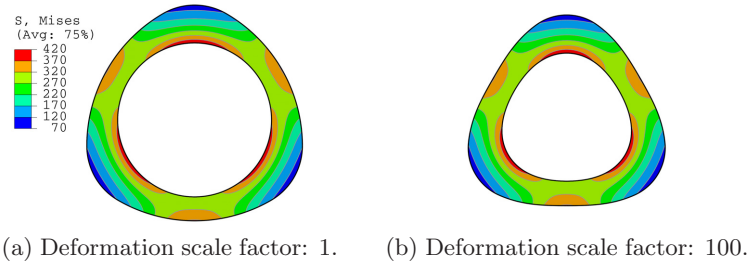


Figure 7.5: Von Mises equivalent stress in the cross section of the steel inserts of the demo prototype loaded by a pressure of $p = 80$ MPa.

7.3 Finite Element Simulation of Quenching, Machining and Mechanical Testing

Fundamental considerations regarding the simulation of the quenching process of a compound casting have been given in Chapter 2 and 3. The basic assumptions made for the simulations presented in this section are therefore stated only briefly. The general purpose finite element program ABAQUS Standard⁽⁴⁾ [Dassault Systèmes, 2008a] has been used to carry out the simulations.

The sequence of simulation steps is as follows:

- Simulation of the quenching process.
- Expansion of the yield surface to account for the effects of natural ageing (see Figure 2.7 on page 26).
- Simulation of the removal of the casting gate (stress redistribution).
- Simulation of mechanical tests (tensile and torsion test).

The simulation starts at the time of immersion of the demo prototype into the quenching water. At that time, it is assumed that all components (aluminum node, steel inserts and sealing insert) exhibit a homogeneous temperature of 400 °C and that the structure is still stress-free (see remarks in Section 2.5). The heat transfer coefficient is taken as a function of the surface temperature as shown in Figure 7.6. Lower values are assumed at the inner surfaces to account for the effects of “entrapped vapor” (see also Section 2.2).

Thermal contact conductance at the steel aluminum interface is taken as a function of contact pressure and macroscopic gap width as described in Section 3.5.

Von Mises rate-independent plasticity with isotropic hardening is assumed for aluminum and steel (see Section 2.5). Stress-strain curves for the relevant temperature range are given in Figure 2.7 on page 26 for A356.0 and in Figure 2.8(b) on page 27 for

⁽⁴⁾<http://www.simulia.com>

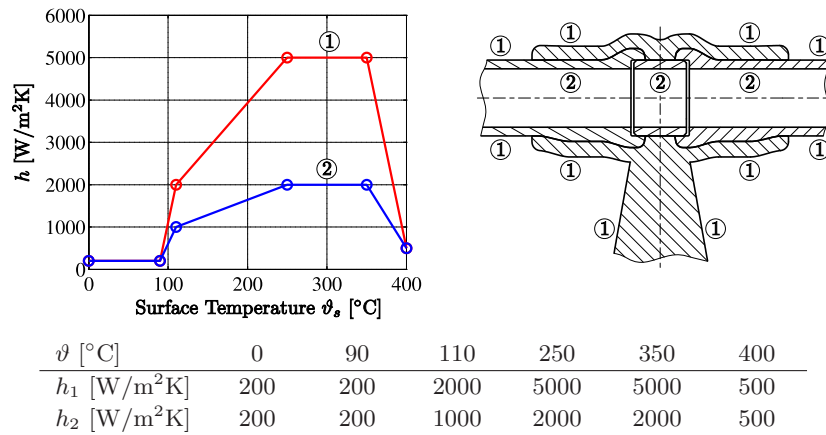


Figure 7.6: Dependence of heat transfer coefficient h on surface temperature ϑ ; initial temperature: 400 °C; $T_\infty = 20$ °C.

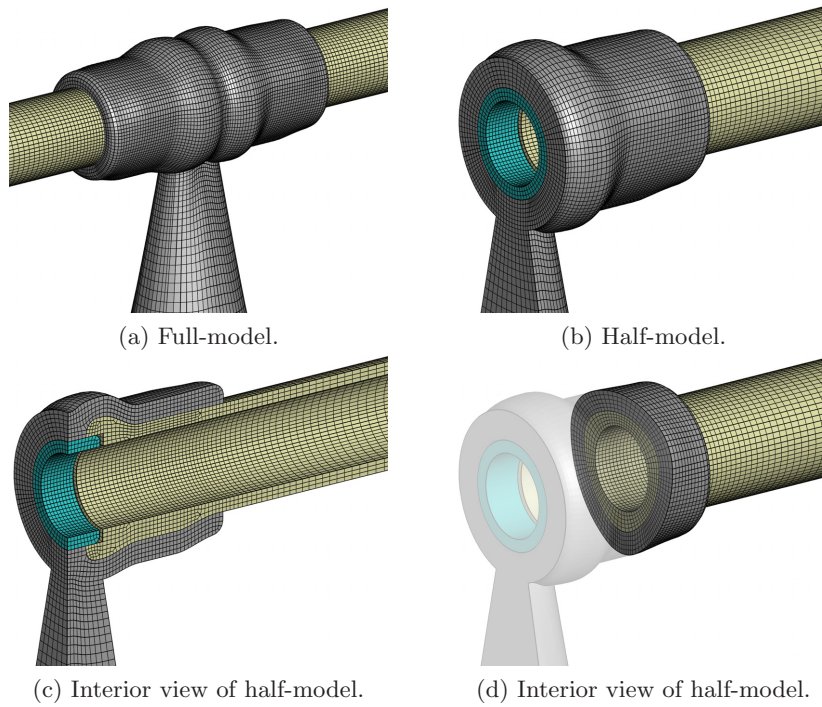


Figure 7.7: Finite element mesh.

C45E. Further required thermophysical and mechanical material properties are given in Section 2.8.

To account for the effect of the lay pattern generated during the milling of the inserts, an anisotropic extension of Coulomb's law of friction is assumed at the steel-aluminum interface. The coefficient of friction is assumed as $\mu_a = 0.6$ in axial direction and as $\mu_c = 0.4$ in circumferential direction. The static and the kinetic coefficient of friction are assumed to be identical.

The removal of the casting gate is simulated using a simple approach. The nodal forces that the elements representing the casting gate are exerting on the remaining part of the model are ramped down to zero during a nonlinear analysis step.

The damage indicator described in chapter 4 is used to predict the onset of fracture in the aluminum alloy A356.0 during the mechanical tests. The critical strain in uniaxial tension ε_0 needed for the calibration of Equation (4.4) is chosen as $\varepsilon_0 = 0.05$.

The demo prototype was meshed with hexahedral elements of type C3D8RT (8-node, linear, coupled temperature-displacement element with reduced integration and hour-glass control). Second order elements could not be used as spurious (nonphysical) oscillations appeared in the solution during quenching simulation [Dassault Systèmes, 2008a].

Figure 7.7 shows various views of the mesh. The four overflows, see Figure 7.4(b), have not been included as their presence neither affects the thermal nor the mechanical problem significantly.

Figure 7.7(a) shows a full-model of the demo prototype containing about 120000 nodes or 480000 degrees of freedom (three displacement degrees of freedom and one temperature degree of freedom per node). As the geometry of the demo prototype is mirror symmetric with respect to the central plane perpendicular to the axis of the structure, a half-model can be used – see Figure 7.7(b). If the loading is mirror symmetric, the boundary conditions for the nodes lying in the plane of symmetry are evident. In the case of torsional loading, however, the loading is not mirror symmetric with respect to said plane. Nevertheless, the half-model can be used to simulate this load case if appropriate boundary conditions are used, as explained in detail in Appendix D. Figures 7.7(c) and (d) show interior views of the half-model.

7.4 Simulation Results and Comparison to Experimental Data

Figure 7.8 illustrates the evolution of the temperature field during the quenching process. Note that each plot has a different color legend.

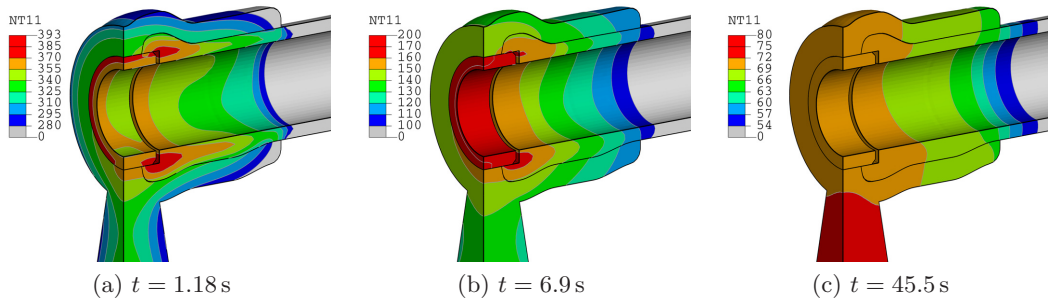


Figure 7.8: Quenching simulation: Temperature field t seconds after immersion into the quenching water. Note the different color legends.

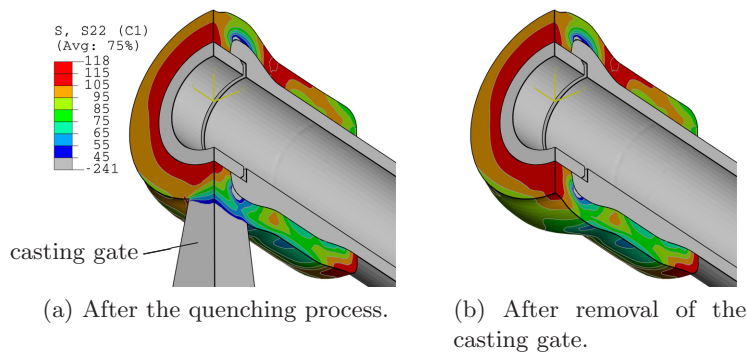


Figure 7.9: Circumferential residual stresses in the cast node.

Figure 7.9 shows circumferential residual stresses in the cast node. Figure 7.9(a) shows the state after the quenching process, and Figure 7.9(b) shows the state after natural ageing and removal of the casting gate. As a result of the removal of the casting gate, a certain degree of stress redistribution occurs. However, the effect is limited to a small region close to the removed part. The extension of the yield surface associated with natural ageing does not cause any stress redistributions.

Figure 7.10 shows the von Mises equivalent stresses after removal of the casting gate. The stress values are depicted on an exploded view of the model. The highest values of the von Mises stress, about 200 MPa, occur in the thin-walled region of the steel insert. This is, however, markedly below the yield stress of the steel (≈ 690 MPa). In the casting values from 60 MPa to 120 MPa are encountered.

Figure 7.11(a) shows the contact pressure on the inner surface of the casting after the removal of the casting gate. Some small areas of very low contact pressure can be observed. As the thermal contact conductance at the steel-aluminum interface decreases with decreasing contact pressure (see Figure 3.9 on page 48), the heat flux “avoids” these regions during the quenching process. This can be observed in Figure 7.11(b),

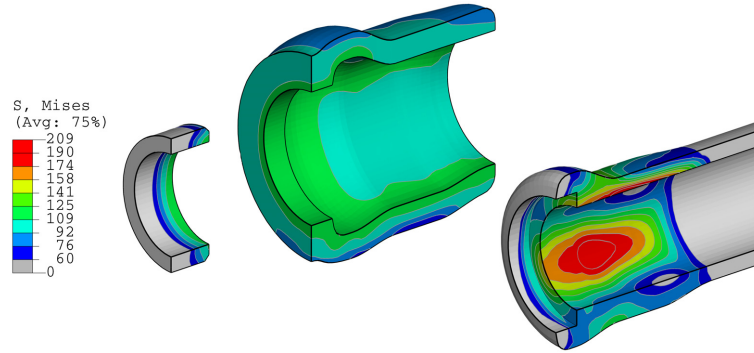


Figure 7.10: Von Mises equivalent stress after removal of the casting gate depicted on an exploded view of the model.

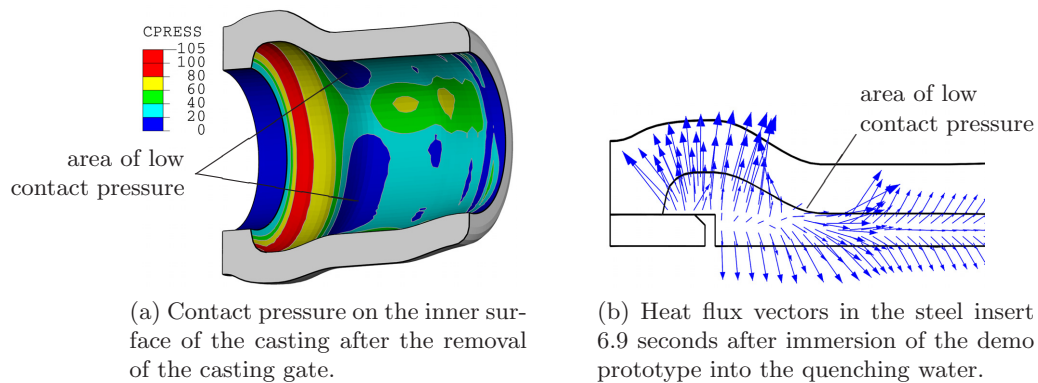


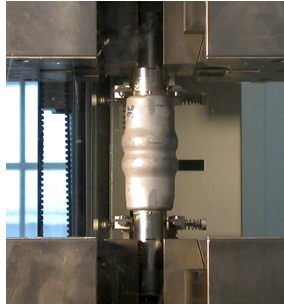
Figure 7.11: Contact pressure and heat flux.

where the heat flux vectors in the steel insert 6.9 seconds after immersion of the demo prototype into the quenching water are shown.

The demo prototype was designed to carry primarily axial and torsional loads. Accordingly, tensile and a torsion tests have been performed (see Figure 7.12). The tensile tests have been carried out by the Institute of Materials Science and Technology, Vienna University of Technology. The torsion tests have been carried out by the Institut für Stahlbau und Werkstoffmechanik, Fachgebiet Werkstoffmechanik, Technische Universität Darmstadt.

Tensile Tests

In Figure 7.13(a) five measured force-displacement curves are compared to the one obtained by simulation. Final fracture in the experiments is marked by crosses. The point where the damage indicator reaches the critical value $D = 1$ in the simulation is marked by a circle. Good agreement between the simulated curve and the measured



(a) Tensile test.



(b) Torsion test, picture courtesy of (*).

(*). Institut für Stahlbau und Werkstoffmechanik, Fachgebiet Werkstoffmechanik, Technische Universität Darmstadt.

Figure 7.12: Mechanical tests.

curves can be observed. Also, final fracture occurs in the experiments shortly after the damage indicator D has reached the critical value $D = 1$.

The position where the critical value of the damage indicator $D = 1$ is reached, is shown in Figures 7.13(c) and (d). The critical value is reached practically simultaneously at two different positions designated as “position 1” and “position 2” in Figures 7.13(c) and (d). All five specimens fractured in a similar manner, see Figure 7.13(b), and in all five cases the location of the crack matches “position 1” as predicted by the damage indicator.

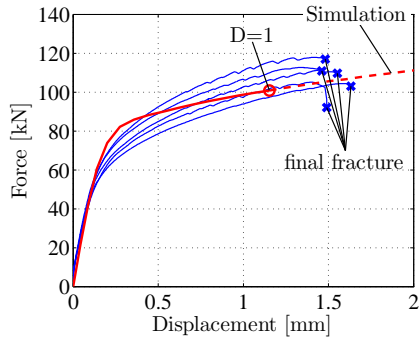
Torsion Tests

In Figure 7.14(a) four measured moment-angle curves are compared to the one obtained by simulation. Final fracture in the experiments is marked by crosses. One specimen did not fracture. The point where the damage indicator reaches the critical value $D = 1$ in the simulation is marked by circle. The agreement between the simulated and the measured curves is not as good as in the case of the tensile test. The torsional moment required to generate a relative motion between the steel inserts and the casting is overpredicted by the simulation.

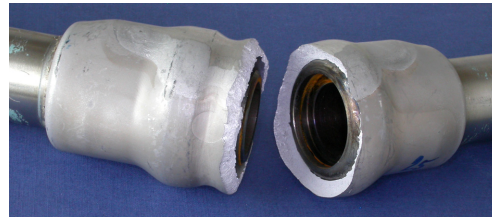
Figures 7.14(c), (d) and (e) indicate the position where the critical value of the damage indicator $D = 1$ is reached. All fractured specimens fractured in a similar manner, see Figure 7.14(b), and in all cases the location of the crack matches the position predicted by the damage indicator.

7.5 Discussion

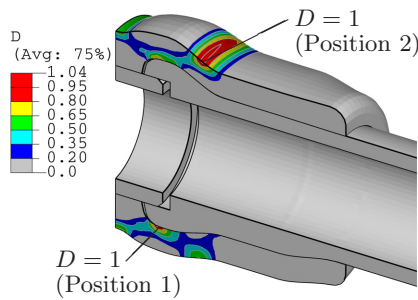
In this chapter a demo prototype of a compound casting manufactured by high pressure die casting and a corresponding finite element model have been presented.



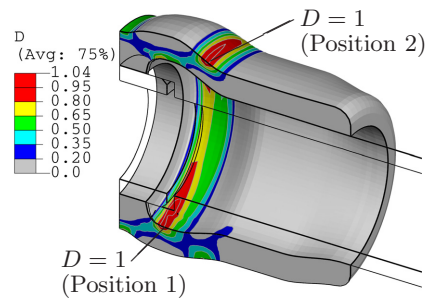
(a) Comparison of the measured force-displacement curves to the one obtained by simulation.



(b) Typical fractured specimen.



(c) Position where the critical value of the damage indicator $D = 1$ is reached.



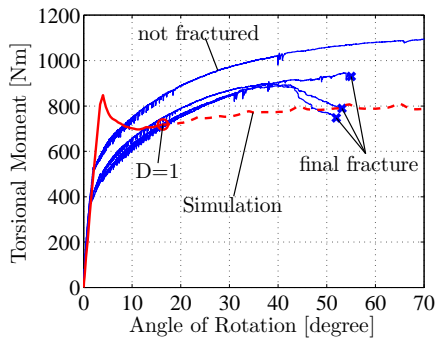
(d) Figure (c) with transparent steel parts.

Figure 7.13: Tensile test.

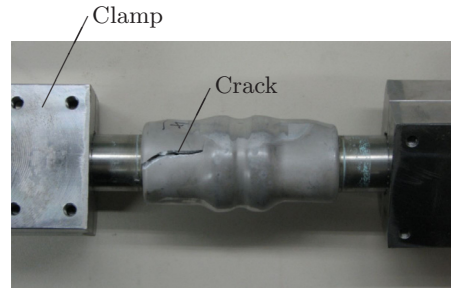
The demo prototype can resist high static loads. For example a tensile axial load of 70 kN, see Figure 7.13(a), corresponds to a uniaxial stress of approximately 320 MPa in the steel inserts, outside of the aluminum node. A torsional load of 600 Nm, see Figure 7.14(a), corresponds to a maximum shear stress of approximately 270 MPa in the steel inserts, outside of the aluminum node.

Generally, the outcome of the mechanical tests is well predicted by the finite element model. Only in the case of the torsion test, the torsional moment required to generate a relative motion between the steel inserts and the casting is clearly overpredicted by the simulation. A possible reason for this overprediction is that the tightening of the clamps, see Figure 7.14(b), might have altered the residual stress state and thus, weakened the frictional connection. The clamps are not taken into account in the finite element model, but the torsional moment is introduced using a suitable coupling constraint far away from the cast node.

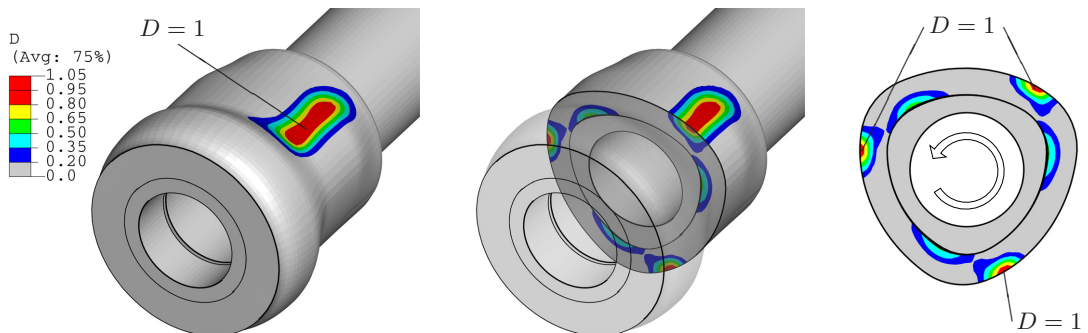
Finite element models like the one presented in this chapter can be a valuable tool in assisting in the design process of a compound casting. The intended gap between the left steel insert and the sealing insert apparent in Figure 7.4(c) is an example for a



(a) Comparison of the measured moment-angle curves to the one obtained by simulation.



(b) Typical fractured specimen; picture courtesy of (*).



(c) Position where the critical value of the damage indicator $D = 1$ is reached.

(d) Figure (c) with translucent front part.

(e) Front view of Figure (d).

(*): Institut für Stahlbau und Werkstoffmechanik, Fachgebiet Werkstoffmechanik, Technische Universität Darmstadt.

Figure 7.14: Torsion test.

design modification suggested by the results of the finite element analysis of a previous design. The gap allows the two steel inserts to axially move towards each other during the cooling of the compound casting. This is important because high axial residual stresses (tensile in the aluminum and compressive in the sealing insert) build up if this relative movement is prohibited, and the additional residual stresses diminish the structure's load carrying capacity.

Chapter 8

Conclusion and Outlook

The aim of this thesis was to develop computational methods for the analysis and design of compound castings and other multi-material structures. Both finite element methods and asymptotic analysis techniques have been presented.

It is difficult to achieve a perfect, continuous material-locking connection during a real, industrial compound casting process. However, excellent results can be achieved using form-locking and/or frictional connections. Practical examples of steel-aluminum compound castings with form-locking and/or frictional connection have been presented in Chapters 6 and 7. In general, the strength as well as the mode of failure of these connections could be well-predicted by the finite element models.

During the quenching (or cooling) of a compound casting, residual stresses develop due to the inhomogeneous transient temperature field and due to the dissimilar coefficients of thermal expansion of the materials involved. As these stresses determine the frictional connection and other important characteristics (e.g. the fatigue life) of the structure, the simulation of the quenching process is of central importance.

For the quenching simulations, stress-strain curves that appropriately describe the behavior of the cast alloy during the quenching operation are required. If the cast alloy responds to precipitation hardening, special care has to be taken as the results of a tensile or compressive test can be distorted by unintended precipitation processes.

Due to the large coefficient of thermal expansion mismatch between steel and aluminum, frictional connections of steel-aluminum compound castings are often so strong that it might be questioned whether an additional form-locking connection is necessary. However, relaxation of residual stresses may weaken the frictional connection over time. Therefore, additional form-locking connections can also be seen as a safeguard.

The thermal contact conductance at the interface of compound castings without metallurgical bonding increases with increasing contact pressure and decreases with increasing gap opening. It is a major finding of this thesis that, in general, the consideration of this dependence is crucial to the simulation of the quenching process of steel-aluminum compound castings. (The same is presumably true for other material combinations.) In many cases a completely different residual stress state will be predicted if the thermal contact conductance is assumed constant (see Section 3.7).

During the quenching process of a compound casting, gaps can open up at the interface, even if the structure is geometrically simple (see Chapter 6). The opening of the gap severely reduces the thermal contact conductance and forces heat to flow mainly parallel to the open gap.

Although this research focused on steel-aluminum compound castings, many concepts and findings are applicable to multi-material structures in general. This is especially true for the examination of stress singularities which may occur at bimaterial interfaces presented in Chapter 5. Design charts have been developed which exhibit the singularity exponent as function of the local geometry (or the local geometry and the coefficient of friction) for a given material combination. Using these charts, stress singularities in a given multi-material structure can be identified and geometry modifications can be determined that minimize the order of the singularity or, ideally, completely remove the stress singularity. As a result, the durability of the multi-material structure will be enhanced. Often, great improvements can be achieved through comparatively small and local modifications of the geometry.

How to Reduce the Level of Residual Stresses

Due to the large coefficient of thermal expansion mismatch between steel and aluminum, high levels of residual stresses are generally generated during the quenching or cooling of a steel-aluminum compound castings. These high stresses are a mixed blessing. On the one hand, they provide for a strong frictional connection. On the other hand, they can (among other things) reduce the fatigue life of a structure. Thus, the question arises how the residual stresses in a steel-aluminum compound casting can be reduced.

Obviously, a stress relief heat treatment is hardly an option as residual stresses build up again during the subsequent cooling process.

One realistic option is a reduction of the coefficient of thermal expansion mismatch. For instance, some high alloy chromium-nickel steels have coefficients of thermal expansion about 50% higher than those of low alloy steels. As shown in Figure 8.1, the mismatch between aluminum cast alloy A356.0 and high alloy chromium-nickel steel X5CrNi18-10 is considerably smaller than that between A356.0 and low alloy steel S355. The reduction of the coefficient of thermal expansion mismatch could not only reduce the residual stresses generated during the quenching (or cooling) of the compound casting, but also reduce the thermally induced stresses during operation.

A further possibility to limit the residual stresses to a suitable level is the use of an aluminum cast alloy that exhibits low yield stress during quenching and a pronounced response to natural ageing.

Still another possibility stems from the example presented in Section 3.7. This example has shown that (falsely) assuming low thermal contact conductance at the steel-aluminum interface can result in a substantially lower level of residual stresses, see

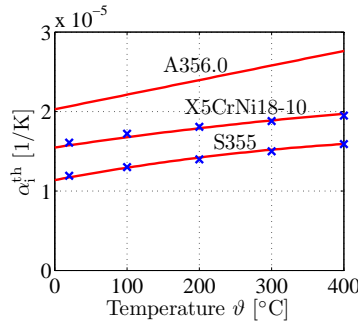


Figure 8.1: Instantaneous coefficient of thermal expansion α_i^{th} of steels S355 and X5CrNi18-10 [SEW 310, 1992] and aluminum cast alloy A356.0 [Kaufman and Rooy, 2005].

Figure 3.11(a). Thus, low residual stresses can be achieved by deliberately reducing thermal contact conductance. One way of doing this would be to introduce a low conductance interstitial material in the interface. This could be achieved by coating the steel inserts (See also the book by Madhusudana [1996]). Presumably, the residual stress level could even be controlled by modifications of the coating thickness.

Propositions for Future Research

If metallurgical bonding is achieved during a steel-aluminum compound casting process, a thin layer of brittle intermetallic phases is formed at the interface. The structural performance of such a compound casting depends on the fracture toughness of that interface. Thus, fracture mechanics parameters of these interfaces should be determined experimentally!

Chapter 3 discusses the thermal contact conductance at a steel-aluminum interface without metallurgical bonding. In order to establish the dependence of the thermal contact conductance on contact pressure and gap opening, it was assumed that the contact at the interface of the compound casting is similar to the common contact of two engineering surfaces. While this seems to be a reasonable assumption, the resulting dependence of the thermal contact conductance on contact pressure depicted in Figure 3.9 (page 48) should be experimentally verified.

Coulomb's law of friction has been assumed at the steel-aluminum interface in this work. The static and the kinetic coefficient of friction have been assumed to be identical and in the range of 0.4 to 0.6. While good agreement with experimental results was generally achieved, the static and kinetic coefficient of friction should be experimentally determined.

For the quenching simulations presented in this thesis von Mises rate-independent plasticity with isotropic hardening and associated flow rule has been assumed for the cast alloy. This is a reasonable assumption for the simulation of "fast" quenching

Chapter 8 Conclusion and Outlook

processes. However, for the simulation of a slow cooling process or the simulation of artificial ageing (ageing at elevated temperatures) an elastic-visco-plastic constitutive model would be required.

In the simulations presented in this work, the effects of natural ageing of the aluminum cast alloy have been accounted for in a simple manner. That is, subsequent to the quenching simulation the yield surface has been expanded according to a representative stress-strain curve measured in the naturally aged condition. In reality, the evolution of the yield stress depends on the degree of supersaturation and thus on the *local* thermal history. If a quantitative model capable of predicting the evolution of the yield stress based on a known thermal history was available, this dependence could be accounted for in the simulations.

Appendices

Appendix A

Cubic Splines Approximating Stress-Strain Curves

Splines are functions defined piecewise by polynomials (see Figure A.1). At the intersections of two polynomial pieces, continuity conditions (e.g. n -times continuously differentiable) are usually assigned in order to achieve a smooth curve. Splines can describe arbitrary functions even when using low degree polynomials and are therefore well suited for the approximation of measured data.

A spline $p(x)$ can be described in terms of its breaks $\xi_1, \xi_2, \dots, \xi_l$ and its polynomial coefficients c_{ji} :

$$p_j(x) = \sum_{i=1}^k (x - \xi_j)^{k-i} c_{ji} \quad j = 1, 2, \dots, l \quad , \quad (\text{A.1})$$

where l is the number of polynomial pieces and k is the number of coefficients in each polynomial ($k = 4$ for a cubic spline). The polynomial $p_j(x)$ describes the spline in the interval $\xi_j \leq x \leq \xi_{j+1}$.

In this work, cubic splines ($k = 4$) haven been used to approximate measured stress-strain curves. Figure A.1 shows an example. Here x refers to logarithmic plastic strain and $p(x)$ refers to true stress in Pascal. A spline with three polynomial pieces is used to describe the stress-strain curve. In the diagram on the left of Figure A.1 the polynomials are plotted over the entire interval, while in the diagram on the right the polynomials are plotted on their respective intervals only. The table on the bottom of Figure A.1 displays the breaks ξ_j and the polynomial coefficients c_{ji} . Note that the spline always passes through the points (ξ_j, c_{j4}) for $j = 1, 2, \dots, l$. The spline shown in Figure A.1 is twice continuously differentiable at the interior breaks ξ_2 and ξ_3 .

To obtain a spline approximation like to one shown in Figure A.1 the following procedure can be followed: First, the number of polynomial pieces l and appropriate breaks ξ_j are chosen. Next, continuity conditions are assigned at the interior breaks (e.g. two times continuously differentiable for a cubic spline). Finally, the polynomial coefficients c_{ji} are determined by least square approximation to the measured data. In MATLAB⁽¹⁾ this last step can be accomplished using the `spap2` function.

⁽¹⁾<http://www.mathworks.com>

Appendix A Cubic Splines Approximating Stress-Strain Curves

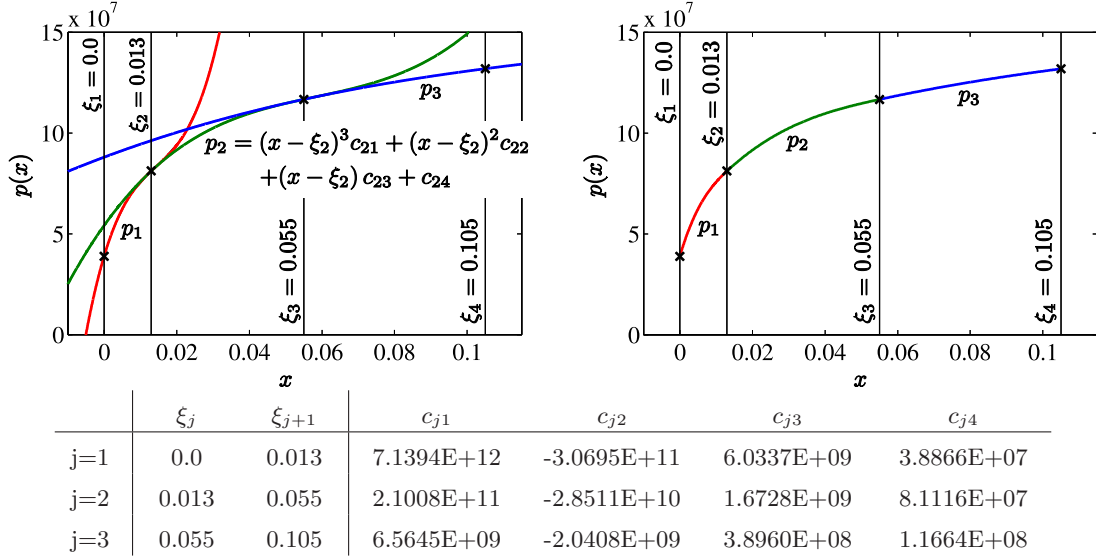


Figure A.1: Cubic spline approximating a measured stress-strain curve.

Tables A.1 to A.3 display the breaks and polynomial coefficients of the splines used for the approximation of stress-strain curves (true stress as a function of logarithmic plastic strain) in the present work. The spline approximating the room temperature stress-strain curve of S355 (Table A.3) is intentionally not continuously differentiable at $\xi_2 = 0.02$.

Appendix A Cubic Splines Approximating Stress-Strain Curves

		ξ_j	ξ_{j+1}	c_{j1}	c_{j2}	c_{j3}	c_{j4}
(5) $\vartheta = 20^\circ\text{C}$	j=1	0.0	1.0E-03	9.6966E+15	-3.2015E+13	4.9374E+10	6.1643E+07
	j=2	1.0E-03	4.0E-03	3.1129E+14	-2.9246E+12	1.4435E+10	8.8698E+07
	j=3	4.0E-03	3.0E-02	1.3713E+12	-1.2296E+11	5.2920E+09	1.1409E+08
	j=4	3.0E-02	1.1E-01	7.5216E+10	-1.5997E+10	1.6792E+09	1.9266E+08
(4) $\vartheta = 200^\circ\text{C}$	j=1	0.0	1.3E-02	7.1394E+12	-3.0695E+11	6.0337E+09	3.8866E+07
	j=2	1.3E-02	5.5E-02	2.1008E+11	-2.8511E+10	1.6728E+09	8.1116E+07
	j=3	5.5E-02	1.05E-01	6.5645E+09	-2.0408E+09	3.8960E+08	1.1664E+08
(3) $\vartheta = 300^\circ\text{C}$	j=1	0.0	1.0E-02	1.1565E+13	-3.7061E+11	4.8558E+09	3.4128E+07
	j=2	1.0E-02	4.0E-02	2.4598E+11	-2.3678E+10	9.1290E+08	5.7189e+07
	j=3	4.0E-02	1.05E-01	8.1749E+09	-1.5392E+09	1.5639E+08	6.9908E+07
(2) $\vartheta = 400^\circ\text{C}$	j=1	0.0	1.5889E-02	3.7802E+11	-4.8326E+10	1.2494E+09	2.3591E+07
	j=2	1.5889E-02	1.0E-01	0.0	0.0	0.0	3.2758E+07
(1) $\vartheta = 500^\circ\text{C}$	j=1	0.0	1.0131E-02	3.1974E+12	-9.7943E+10	1.0000E+09	7.6016E+06
	j=2	1.0131E-02	1.0E-01	0.0	0.0	0.0	1.1005E+07

Table A.1: Splines approximating stress-strain curves (true stress as a function of logarithmic plastic strain) for the quenching simulation of A356.0; numbers in brackets refer to curves in Figure 2.7 on page 26; stress in Pascal.

		ξ_j	ξ_{j+1}	c_{j1}	c_{j2}	c_{j3}	c_{j4}
(6) nat. aged $\vartheta = 20^\circ\text{C}$	j=1	0.0	1.0E-03	4.3320E+15	-1.6589E+13	3.7323E+10	7.8531E+07
	j=2	1.0E-03	4.0E-03	3.8323E+14	-3.5933E+12	1.7140E+10	1.0360E+08
	j=3	4.0E-03	3.0E-02	1.6169E+12	-1.4427E+11	5.9275E+09	1.3302E+08
	j=4	3.0E-02	8.2E-02	9.5583E+10	-1.8148E+10	1.7048E+09	2.1803E+08
(7) art. aged $\vartheta = 20^\circ\text{C}$	j=1	0.0	1.0E-03	2.1103E+16	-6.7745E+13	9.0861E+10	1.2851E+08
	j=2	1.0E-03	4.0E-03	4.7871E+14	-4.4367E+12	1.8679E+10	1.7273E+08
	j=3	4.0E-03	3.0E-02	1.4491E+12	-1.2831E+11	4.9843E+09	2.0176E+08
	j=4	3.0E-02	7.5E-02	4.8049E+10	-1.5273E+10	1.2513E+09	2.7009E+08

Table A.2: Splines approximating stress-strain curves (true stress as a function of logarithmic plastic strain) of A356.0 in the naturally and artificially aged condition; numbers in brackets refer to curves in Figure 2.7 on page 26; stress in Pascal.

	ξ_j	ξ_{j+1}	c_{j1}	c_{j2}	c_{j3}	c_{j4}
S355 ¹						
j=1	0.0	2.0E-02	0.0	0.0	7.0417E+08	3.8500E+08
j=2	2.0E-02	7.0E-02	1.7118E+11	-3.3828E+10	3.6109E+09	4.0503E+08
j=3	7.0E-02	1.8E-01	2.7269E+10	-8.1505E+09	1.5120E+09	5.2241E+08
C45E						
j=1	0.0	1.8E-01	0.0	0.0	4.4444E+08	6.9000E+08

¹ The spline is intentionally not continuously differentiable at $\xi_2 = 0.02$.

Table A.3: Splines approximating stress-strain curves for steels S355 and C45E at room temperature; compare Figure 2.8 on page 27; stress in Pascal.

Appendix B

Polynomials Approximating Temperature Dependence of Thermophysical and Mechanical Properties

The temperature dependence of mechanical and thermophysical material properties of aluminum alloy A356.0, steel S355 and steel C45E have been approximated by low order polynomials (see Section 2.8).

For instance, the temperature dependence of a material property p is described by:

$$p(\vartheta) = a_0 + a_1\vartheta + \cdots + a_n\vartheta^n, \quad (\text{B.1})$$

where ϑ is the Celsius temperature.

In some cases the polynomial coefficients ($a_0, a_1 \dots a_n$) could be taken directly from the literature. In the remaining cases suitable polynomials were fitted to the literature data by least square approximation.

The polynomial coefficients are reported in Table B.1 to B.4. Each row lists a material property, the polynomial coefficients, the limits of applicability ($\vartheta_{\min}, \vartheta_{\max}$), the source of data and the number of the figure showing the curve. SI units have been used for all properties given in this Appendix.

	a_0	a_1	a_2	a_3	ϑ_{\min}	ϑ_{\max}	Source	Figure
α_i^{th}	2.269E-05	3.902E-08	-1.185E-10	1.548E-13	-250	600	[Blanke, 1989]	2.12(a)
c_p	8.9138E+02	4.59E-01	-	-	25	655	[Blanke, 1989]	2.16(a)
λ	2.3762E+02	1.7013E-02	-9.6253E-05	-	0	527	[Blanke, 1989]	2.14
E	7.2720E+10	-3.9852E+07	-1.9166E+04	-	-273	620	[Mondolfo, 1979]	2.9

Table B.1: Polynomial coefficients describing temperature dependence of material properties of pure aluminum; all properties in SI units.

	a_0	a_1	a_2	a_3	ϑ_{\min}	ϑ_{\max}	Source	Figure
α_i^{th}	2.0294E-05	1.8369E-08	-	-	-20	315	[Kaufman and Rooy, 2005]	2.12(a)
c_p	7.7815E+02	7.5579E-01	-	-	20	535	[Blumm et al., 1998]	2.16(a)
λ	1.5297E+02	-	-	-	0	450	[Blumm et al., 1998]	2.14

Table B.2: Polynomial coefficients describing temperature dependence of material properties of A356.0; all properties in SI units.

	a_0	a_1	a_2	a_3	ϑ_{\min}	ϑ_{\max}	Source	Figure
α_i^{th}	1.1373E-05	1.6963E-08	-1.4043E-11	-	-100	600	[SEW 310, 1992]	2.12(b)
c_p	4.4855E+02	6.1100E-01	-1.3354E-03	2.0544E-06	-100	600	[SEW 310, 1992]	2.16(b)
λ	4.1600E+01	2.6752E-02	-1.1821E-04	8.8333E-08	-100	600	[SEW 310, 1992]	2.15(a)
E	2.1255E+11	-5.4421E+07	-4.3439E+04	-	-100	600	[SEW 310, 1992]	2.10

Table B.3: Polynomial coefficients describing temperature dependence of material properties of S355; all properties in SI units.

	a_0	a_1	a_2	a_3	ϑ_{\min}	ϑ_{\max}	Source	Figure
α_i^{th}	1.1373E-05	1.6963E-08	-1.4043E-11	-	-100	600	[SEW 310, 1992]	2.12(b)
c_p	4.4855E+02	6.1100E-01	-1.3354E-03	2.0544E-06	-100	600	[SEW 310, 1992]	2.16(b)
λ	4.1187E+01	3.3109E-02	-1.3713E-04	1.0418E-07	20	600	[SEW 310, 1992]	2.15(b)
E	2.1255E+11	-5.4421E+07	-4.3439E+04	-	-100	600	[SEW 310, 1992]	2.10

Table B.4: Polynomial coefficients describing temperature dependence of material properties of C45E; all properties in SI units.

Appendix C

Additional Design Charts

Section 5.5.2 presented a design chart for the case of an end point of a perfectly bonded bimaterial interface. The material combination considered was steel-aluminum, hence the ratio of Young's moduli was $E_2/E_1 = 3$.

To demonstrate the effect of a distinctly higher ratio of Young's moduli, a design chart for a hypothetical material combination with $E_2/E_1 = 10$ is presented in this appendix. The material properties and Dundurs parameters are given in Table C.1. The design chart is shown in Figure C.1 and C.2.

$E_2/E_1 = 10$
$\nu_1 = \nu_2 = 0.3$
$G_2/G_1 = 10$
$\alpha = 0.8182, \beta = 0.2338$

Table C.1: Hypothetical Material combination with $E_2/E_1 = 10$: Material properties and Dundurs parameters for plane strain.

Appendix C Additional Design Charts

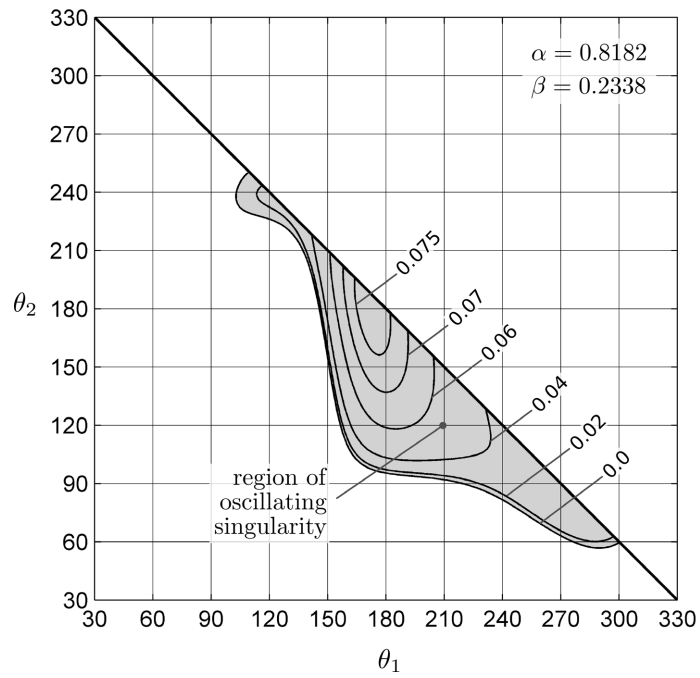
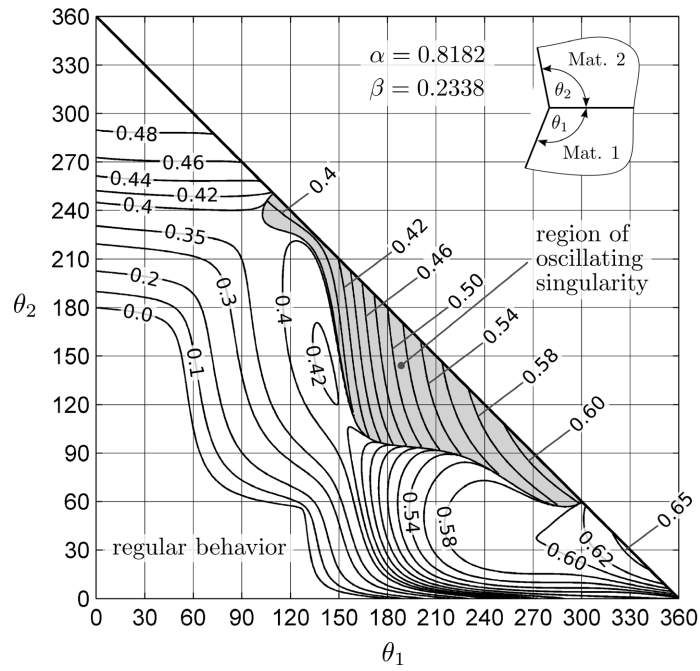


Figure C.1: Design chart for the end point of a perfectly bonded bimaterial interface; material combination: Table C.1.

Appendix C Additional Design Charts

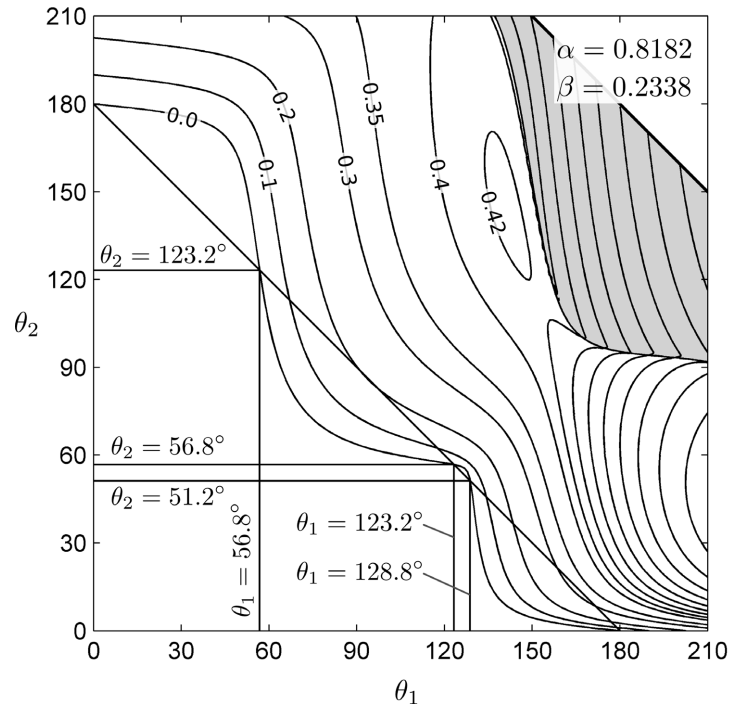


Figure C.2: Detail of the design chart in Figure C.1(a) illustrating how to avoid singular behavior while keeping a smooth outer surface ($\theta_1 + \theta_2 = 180^\circ$).

Appendix D

Boundary Conditions for Torsional Loading

The geometry of the demo prototype studied in Chapter 7 is mirror-symmetric with respect to the central plane perpendicular to the axis of the structure, see Figure 7.2 on page 106. Hence, a *half-model* was used for the finite element analysis, see Figure 7.7(a) on page 110.

If the loading is mirror-symmetric (quenching simulation, tensile test) the boundary conditions for the nodes lying in the plane of symmetry are evident. In the case of torsional loading, the loading is not mirror symmetric with respect to said plane. As will be explained in this appendix, it is still possible to employ the half-model if appropriate boundary conditions are used.

For the sake of simplicity, the approach is here explained by means of the simple, torsionally loaded structure shown in Figure D.1. The structure is similar to the demo prototype in the sense that it exhibits the same symmetries. Figure D.1(a) shows the complete structure, whereas Figure D.1(b) shows the half-model. Appropriate boundary conditions are needed for the nodes lying in the x-y-plane as indicated in Figure D.1(b).

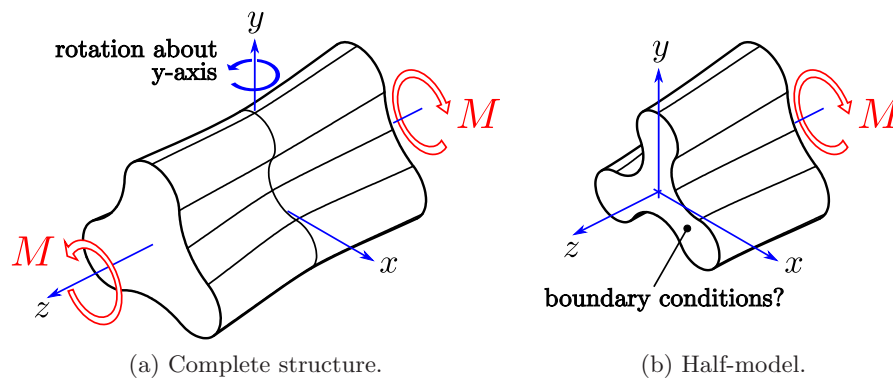


Figure D.1: Structure exhibiting the same symmetries as the demo prototype in Chapter 7.

Appendix D Boundary Conditions for Torsional Loading

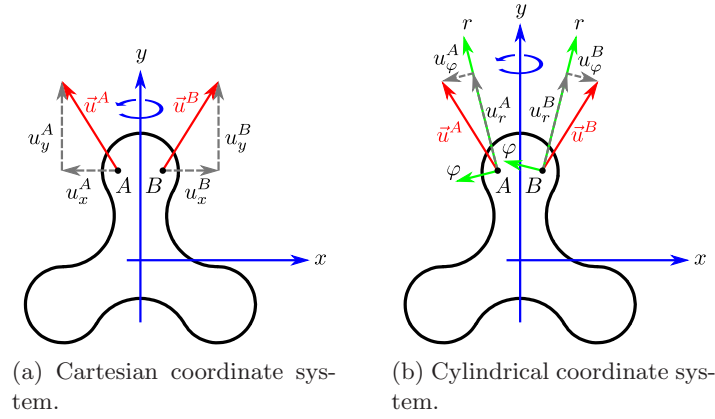


Figure D.2: Displacements of corresponding points in the x-y-plane.

While the problem is not mirror-symmetric with respect to the x-y-plane, it is symmetric with respect to a 180° rotation about the y-axis. That is, the displacements must also be symmetric with respect to this rotation.

In the x-y-plane, the rotation maps point A onto point B as shown in Figure D.2(a). For the displacements follows:

$$u_x^A = -u_x^B, \quad u_y^A = u_y^B, \quad u_z^A = -u_z^B. \quad (\text{D.1})$$

For the nodes lying on the y-axis this implies:

$$u_x = 0, \quad u_z = 0. \quad (\text{D.2})$$

If a cylindrical coordinate system is used, as shown in Figure D.2(b), the corresponding expressions are:

$$u_r^A = u_r^B, \quad u_\phi^A = -u_\phi^B, \quad u_z^A = -u_z^B, \quad (\text{D.3})$$

and for the nodes lying on the y-axis:

$$u_\phi = 0, \quad u_z = 0. \quad (\text{D.4})$$

In finite element programs Equations (D.1) or (D.3) can be accounted for using suitable constraint equations.

Figure D.3 shows deformed finite element models (deformation scale factor: 1) of the problem shown in Figure D.1. Colors correspond to displacements in axial direction. While Figure D.3(a) shows a full-model, Figure D.3(b) shows a half-model employing suitable constraint equations. The results from both models are identical.

Care has to be taken when the approach presented in this appendix is applied to the simulation of the demo prototype presented in Chapter 7 using ABAQUS⁽¹⁾. If linear multi-point constraints⁽²⁾ are used to define the appropriate boundary conditions, the

⁽¹⁾<http://www.simulia.com>

⁽²⁾Keyword: *EQUATION

Appendix D Boundary Conditions for Torsional Loading

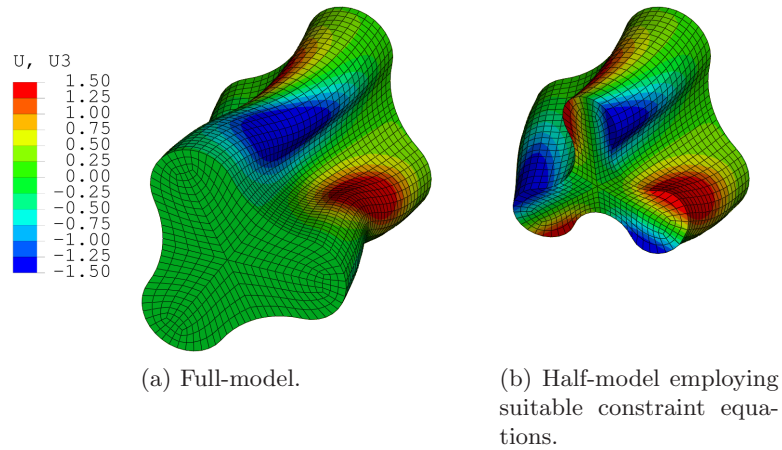


Figure D.3: Deformed finite element models (deformation scale factor: 1) of the problem shown in Figure D.1. Colors correspond to displacements in axial direction.

constraints are imposed by eliminating degrees of freedom. The “eliminated nodes” should not be involved in any contact definitions (see Figure 7.7(a) on page 110). In the case of the demo prototype the “eliminated nodes” had to be removed from the contact definitions in order to achieve convergence.

Bibliography

The entries are arranged alphabetically by the author's last name.

- Alonso Rasgado, M. T. and Davey, K., 2002. An experimental investigation on the effect of vibration on casting surface finish. *Journal of Manufacturing Science and Engineering*, 124(2):435–443. doi:10.1115/1.1459085.
- ASM, 1991. *ASM Handbook*, vol. 4, Heat Treating. ASM International.
- Bathe, K.-J., 2002. *Finite-Elemente-Methoden*. Berlin: Springer, second edn.
- Blanke, W., ed., 1989. *Thermophysikalische Stoffgrößen*. Springer.
- Blumm, J., Henderson, J. B., and Hagemann, L., 1998. Measurement of the thermophysical properties of an aluminium-silicon casting alloy in the solid and molten regions. *High Temperatures - High Pressures*, 30:153–157.
- Bogy, D. B., 1968. Edge-bonded dissimilar orthogonal elastic wedges under normal and shear loading. *Journal of Applied Mechanics*, 35(3):460–466.
- Bogy, D. B., 1970. On the problem of edge-bonded elastic quarter-planes loaded at the boundary. *International Journal of Solids and Structures*, 6:1287–1313.
- Bogy, D. B., 1971. Two edge-bonded elastic wedges of different materials and wedge angles under surface tractions. *Journal of Applied Mechanics*, 38(2):377–386.
- Bogy, D. B., 1975. The plane solution for joined dissimilar elastic semistrrips under tension. *Journal of Applied Mechanics*, 42:93–98.
- Bogy, D. B. and Wang, K. C., 1971. Stress singularities at interface corners in bonded dissimilar isotropic elastic materials. *International Journal of Solids and Structures*, 7(8):993–1005. doi:10.1016/0020-7683(71)90077-1.
- Borrisutthekul, R., Yachi, T., Miyashita, Y., and Mutoh, Y., Oct. 2007. Suppression of intermetallic reaction layer formation by controlling heat flow in dissimilar joining of steel and aluminum alloy. *Materials Science and Engineering: A*, 467:108–113. doi:10.1016/j.msea.2007.03.049.
- Chen, D.-h. and Nisitani, H., 1993. Singular stress field near the corner of jointed dissimilar materials. *Journal of Applied Mechanics*, 60(3):607–613. doi:10.1115/1.2900847.

Bibliography

- Churchman, C., Mugadu, A., and Hills, D. A., 2003. Asymptotic results for slipping complete frictional contacts. *European Journal of Mechanics - A/Solids*, 22(6):793–800.
- Comninou, M., 1976. Stress singularity at a sharp edge in contact problems with friction. *Journal of Applied Mathematics and Physics (ZAMP)*, 27:493–499.
- Dassault Systèmes, Apr. 2008a. *Abaqus Analysis User's Manual*. Version 6.8, <http://www.simulia.com>.
- Dassault Systèmes, Apr. 2008b. *Abaqus Scripting User's Manual*. Version 6.8, <http://www.simulia.com>.
- DIN 32711, Mar. 1979. Antriebs-elemente, Polygonprofil P3G. Technical Standard.
- DIN 32711-1, Jan. 2007. Welle-Nabe-Verbindung - Polygonprofil P3G. Proposed Technical Standard.
- DIN EN 10025-2, Apr. 2005. Warmgewalzte Erzeugnisse aus Baustählen - Teil 2: Technische Lieferbedingungen für unlegierte Baustähle. Technical Standard.
- DIN EN 10083-2, Oct. 2006. Vergütungsstähle - Teil 2: Technische Lieferbedingungen für unlegierte Stähle. Technical Standard.
- Dittmann, A., 1995. *Repetitorium der technischen Thermodynamik*. Vieweg+Teubner.
- Dundurs, J., 1969. Discussion of [Bogy, 1968]. *Journal of Applied Mechanics*, 36(3):650–652.
- Dundurs, J. and Lee, M. S., Jun. 1972. Stress concentration at a sharp edge in contact problems. *Journal of Elasticity*, 2(2):109–112.
- Durelli, A. J. and Parks, V. J., 1972. Discussion of [Bogy, 1971]. *Journal of Applied Mechanics*, 39(1):317.
- El Sebaie, O., Samuel, A. M., Samuel, F. H., and Doty, H. W., Jul. 2008. The effects of mischmetal, cooling rate and heat treatment on the hardness of A319.1, A356.2 and A413.1 Al-Si casting alloys. *Materials Science and Engineering: A*, 486(1-2):241–252. doi:10.1016/j.msea.2007.09.011.
- Estey, C. M., Cockcroft, S. L., Maijer, D. M., and Hermesmann, C., Oct. 2004. Constitutive behaviour of A356 during the quenching operation. *Materials Science and Engineering: A*, 383(2):245–251. doi:10.1016/j.msea.2004.06.004.
- Fischer, F. D., Kolednik, O., Shan, G. X., and Rammerstorfer, F. G., Dec. 1995. A note on calibration of ductile failure damage indicators. *International Journal of Fracture*, 73(4):345–357.

Bibliography

- Fragner, W., Papis, K., Uggowitzer, P., and Wosik, J., 2008. Herausforderungen und Lösungsmöglichkeiten bei der Herstellung von Verbundgussbauteilen. *Giesserei-Praxis*, 7-8:243–248.
- Fragner, W., Zberg, B., Sonnleitner, R., Uggowitzer, P. J., and Löffler, J. F., 2006. Interface reactions of Al and binary Al-alloys on mild steel substrates in controlled atmosphere. *Materials Science Forum*, 519–521:1157–1162.
- Frank, A. and Pflanzl, M., 1998. *VDI Berichte 1384, Welle-Nabe-Verbindungen*, chap. Die Norm-Polygonverbindungen P3G und P4C - Geometrische Grundlagen, Funktionsverhalten und Fertigung, pages 105–120. VDI.
- Giannakopoulos, A. E., Lindley, T. C., and Suresh, S., May 1998. Aspects of equivalence between contact mechanics and fracture mechanics: theoretical connections and a life-prediction methodology for fretting-fatigue. *Acta Materialia*, 46:2955–2968. doi:10.1016/S1359-6454(98)00011-1.
- Goede, M., Stehlin, M., Rafflenbeul, L., Kopp, G., and Beeh, E., Dec. 2008. Super light car – lightweight construction thanks to a multi-material design and function integration. *European Transport Research Review*. doi:10.1007/s12544-008-0001-2.
- Gross, D. and Seelig, T., 2007. *Bruchmechanik*. Springer, fourth edn.
- Gänsler, H.-P., Atkins, A. G., Kolednik, O., Fischer, F. D., and Richard, O., 2001. Upsetting of cylinders: A comparison of two different damage indicators. *Journal of Engineering Materials and Technology*, 123:94–99.
- Hancock, J. W. and Mackenzie, A. C., 1976. On the mechanisms of ductile failure in high-strength steels subjected to multi-axial stress-states. *Journal of the Mechanics and Physics of Solids*, 24:147–169.
- Kammer, C., 2002. *Aluminium Taschenbuch*. Aluminium-Verlag, 16th edn.
- Kaufman, J. G. and Rooy, E. L., 2005. *Aluminum Alloy Castings, Properties, Processes and Applications*. ASM International.
- Kliauga, A. M., Vieira, E. A., and Ferrante, M., 2008. The influence of impurity level and tin addition on the ageing heat treatment of the 356 class alloy. *Materials Science and Engineering: A*, 480(1-2):5–16. doi:10.1016/j.msea.2007.07.091.
- Klüting, M. and Landerl, C., 2004. Der neue Sechszylinder Ottomotor von BMW, Teil I: Konzept und konstruktiver Aufbau. *MTZ*, 11:868–880.
- Lee, D. and Barber, J. R., 2006. An automated procedure for determining asymptotic elastic stress fields at singular points. *The Journal of Strain Analysis for Engineering Design*, 41(4):287–295. doi:10.1243/03093247JSA164.
- Lemaitre, J. and Desmorat, R., 2005. *Engineering Damage Mechanics*. Springer.

Bibliography

- Loulou, T., Artyukhin, E. A., and Bardon, J. P., Jun. 1999a. Estimation of thermal contact resistance during the first stages of metal solidification process: I—experiment principle and modelisation. *International Journal of Heat and Mass Transfer*, 42(12):2119–2127. doi:10.1016/S0017-9310(98)00333-0.
- Loulou, T., Artyukhin, E. A., and Bardon, J. P., Jun. 1999b. Estimation of thermal contract resistance during the first stages of metal solidification process: II—experimental setup and results. *International Journal of Heat and Mass Transfer*, 42(12):2129–2142. doi:10.1016/S0017-9310(98)00338-X.
- Lumley, R. N., O'Donnell, R. G., Gunasegaram, D. R., and Givord, M., Oct. 2007. Heat treatment of high-pressure die castings. *Metallurgical and Materials Transactions A*, 38(10):2564–2574. doi:10.1007/s11661-007-9285-4.
- Madhusudana, C. V., 1996. *Thermal Contact Conductance*. Springer.
- Maniruzzaman, M. and Sisson, R. D., Jr., Dec. 2004. Heat transfer coefficients for quenching process simulation. *Journal de Physique IV (Proceedings)*, 120:521–528. doi:10.1051/jp4:2004120060.
- Mikic, B. B., 1974. Thermal contact conductance - theoretical considerations. *International Journal Of Heat And Mass Transfer*, 17(2):205–214.
- Mohr, D. and Henn, S., Dec. 2007. Calibration of stress-triaxiality dependent crack formation criteria: A new hybrid experimental-numerical method. *Experimental Mechanics*, 47(6):805–820.
- Mondolfo, L. F., 1979. *Aluminum Alloys, Structure and Properties*. Butterworths.
- Nikanorov, S., Volkov, M., Gurin, V., Burenkov, Y., Derkachenko, L., Kardashev, B., Regel, L., and Wilcox, W., Jan. 2005. Structural and mechanical properties of Al-Si alloys obtained by fast cooling of a levitated melt. *Materials Science and Engineering: A*, 390(1-2):63–69. doi:10.1016/j.msea.2004.07.037.
- Nowell, D., Dini, D., and Hills, D. A., 2006. Recent developments in the understanding of fretting fatigue. *Engineering Fracture Mechanics*, 73(2):207–222. doi:10.1016/j.engfracmech.2005.01.013.
- O'Dowd, N. P., 2008. *Concise Encyclopedia of the Properties of Materials Surfaces and Interfaces*, chap. Fracture at Interfaces, pages 154–160. Elsevier, first edn.
- Papis, K. J. M., Hallstedt, B., Löffler, J. F., and Uggowitzer, P. J., 2008. Interface formation in aluminium-aluminium compound casting. *Acta Materialia*, 56(13):3036–3043. doi:10.1016/j.actamat.2008.02.042.
- Polmear, I., 2006. *Light Alloys*. Elsevier, fourth edn.

Bibliography

- Potesser, M., Schoeberl, T., Antrekowitsch, H., and Bruckner, J., 2006. The characterization of the intermetallic Fe-Al layer of steel-aluminum weldings. In *EPD Congress 2006*. The Minerals, Metals & Materials Society.
- Reddy, B. V. and Deevi, S. C., Dec. 2000. Thermophysical properties of FeAl (Fe-40 at.% Al). *Intermetallics*, 8:1369–1376.
- Rice, J. R., 1988. Elastic fracture mechanics concepts for interfacial cracks. *Journal of Applied Mechanics*, 55:98–103.
- Rice, J. R. and Tracey, T. M., 1969. On the ductile enlargement of voids in triaxial stress fields. *Journal of the Mechanics and Physics of Solids*, 17:201–217.
- Richter, F., 1973. Stahleisen Sonderbericht: Die wichtigsten physikalischen Eigenschaften von 52 Eisenwerkstoffen. Tech. rep., Verlag Stahleisen.
- Richter, F., 1991. Die physikalischen Eigenschaften von metallischen Werkstoffen. *Metall*, 45(6):582.
- Rohloff, H. and Zastera, A., eds., 1996. *Physikalische Eigenschaften gebräuchlicher Stähle*. Stahleisen.
- Rometsch, P. A., Starink, M. J., and Gregson, P. J., Jan. 2003. Improvements in quench factor modelling. *Materials Science and Engineering: A*, 339(1-2):255–264. doi:10.1016/S0921-5093(02)00110-7.
- Santos, C. A., Quaresma, J. M. V., and Garcia, A., Apr. 2001. Determination of transient interfacial heat transfer coefficients in chill mold castings. *Journal of Alloys and Compounds*, 319(1-2):174–186. doi:10.1016/S0925-8388(01)00904-5.
- Schulze, G. E. R., 1967. *Metallphysik*. Akademie-Verlag.
- SEW 310, Aug. 1992. Physikalische Eigenschaften von Stählen. Taschenbuch der Stahl-Eisen-Werkstoffblätter, 10. Auflage, Stahleisen.
- Sinclair, G. B., 2004a. Stress singularities in classical elasticity–I: Removal, interpretation, and analysis. *Applied Mechanics Reviews*, 57(4):251–298. doi:10.1115/1.1762503.
- Sinclair, G. B., 2004b. Stress singularities in classical elasticity–II: Asymptotic identification. *Applied Mechanics Reviews*, 57(5):385–439. doi:10.1115/1.1767846.
- Sinha, A. K., 2003. *Physical Metallurgy Handbook*. McGraw-Hill.
- Sritharan, T., Murali, S., and Hing, P., Jul. 2000. Synthesis of aluminium-iron-silicon intermetallics by reaction of elemental powders. *Materials Science and Engineering: A*, 286(2):209–217. doi:10.1016/S0921-5093(00)00823-6.
- THERPRO. Thermo-physical Properties Database provided by the International Atomic Energy Agency. URL <http://therpro.hanyang.ac.kr>.

Bibliography

- VDI, 2002. *VDI-Wärmeatlas*. VDI-Gesellschaft Verfahrenstechnik und Chemieingenieurwesen, 9th edn.
- Wahid, S. M. S. and Madhusudana, C. V., Dec. 2000. Gap conductance in contact heat transfer. *International Journal of Heat and Mass Transfer*, 43(24):4483–4487. doi:10.1016/S0017-9310(00)00071-5.
- Whitcomb, J. D., Raju, I. S., and Goree, J. G., 1982. Reliability of the finite element method for calculating free edge stresses in composite laminates. *Computers & Structures*, 15(1):23–37. doi:10.1016/0045-7949(82)90030-X.
- Williams, M. L., 1952. Stress singularities resulting from various boundary conditions in angular corners of plates in extension. *Journal of Applied Mechanics*, 19:526–528.
- Zhang, B., Maijer, D. M., and Cockcroft, S. L., 2007a. Development of a 3-D thermal model of the low-pressure die-cast (LPDC) process of A356 aluminum alloy wheels. *Materials Science and Engineering: A*, 464(1-2):295 – 305. doi:10.1016/j.msea.2007.02.018.
- Zhang, L., Zhou, B., Zhan, Z., Jia, Y., Shan, S., Zhang, B., and Wang, W., Mar. 2007b. Mechanical properties of cast A356 alloy, solidified at cooling rates enhanced by phase transition of a cooling medium. *Materials Science and Engineering: A*, 448(1-2):361–365. doi:10.1016/j.msea.2006.10.025.